Sequence Stratigraphy and Seismic-Guided Estimation of Log Properties of the Second Sand Member of the Bone Spring Formation, Delaware Basin, New Mexico

by

Robin A. Pearson

Submitted in partial fulfillment of the requirements to
the degree of Masters of Science in Geology

New Mexico Institute of Mining and Technology

Socorro, New Mexico

May 1999

Abstract

Seismic attributes have the potential to significantly improve reservoir property predictions in interwell areas if care is taken to ensure that the results are geologically and geophysically reasonable as well as statistically significant. This study illustrates how an integrated, volume-based attribute analysis can be used to determine reservoir properties and evaluate infill drilling targets via a case study of an oil and gas field producing from the Second Sand Member of the Bone Spring Formation along the northern slope of the Delaware Basin, New Mexico. The Second Sand is a stratigraphically complex submarine fan deposit, and more traditional horizon- and interval-based attribute analysis techniques have been unable to predict porosity with the desired accuracy.

Based on an integrated analysis of well logs, cores, and 3-D seismic data, a combination of high frequency sea level changes, variations in sediment supply, and tectonic activity have resulted in a submarine fan deposit that is largely confined to a small intraslope basin and which can be subdivided into a basin-floor fan, a slope fan, and a modified lowstand wedge. The best reservoir quality is found in the slope fan. The porosity distribution was successfully predicted using a combination of five seismic attributes. Although the predicted porosity distribution is complex, it appears to be geologically reasonable with high porosities (>10%) tending to occur in what is believed to be a channel fairway, and zones of extreme low porosity being associated with faults. Three potential drilling targets were identified within the slope fan, and were assigned risk factors based on the geologic setting, production history, and statistical significance. These results have implications for the way in which other attribute studies are done and for Bone Spring exploration elsewhere.

Acknowledgments

Table of Contents

List of Tables

List of Figures

List of Abbreviations

ϕ	porosity
λ	wavelength
AI	acoustic impedance
CMP	common midpoint
DMO	dip moveout
f	frequency
NMO	normal moveout
RC	reflection coefficient
S/N	signal to noise ratio
v	velocity
VSP	vertical seismic profile

1. Introduction

1.1 Purpose of Study and Project Objectives

The purpose of this study is to investigate seismic attribute-based porosity predictions and to illustrate how a research project that integrates geology and geophysics can be used to validate attribute–based predictions of reservoir properties. This approach is demonstrated via a case study of the porosity distribution of the Second Sand Member of the Bone Spring Formation of southeast New Mexico.

The Bone Spring Formation was chosen for this study because it is a thick, stratigraphically complex unit composed of intercalated carbonates and siliciclastics that has been heavily explored along the slope of the northern margin of the Delaware Basin. There is a need to re-evaluate the slope reserves of the siliciclastic members, and a better understanding of their stratigraphy and the distribution of reservoir properties is necessary in order to fully exploit their reservoir potential. Thus, in addition to developing a methodology for an integrated attribute analysis, this study will also provide needed information about the Bone Spring siliciclastic reservoirs along the slope.

The specific objectives of this project are: (1) to illustrate an how geology can be integrated into a geostatistical analysis and how the validity of the statistical results can be tested within a geologic framework, (2) to provide detailed documentation of an integrated, volume-based seismic attribute analysis, (3) to develop a sequence stratigraphic model of the Second Bone Spring Sand that can be used as an analog in other areas along the slope, (4) to determine the factors that influence the distribution of porosity within the study area, and perhaps have similar relationships in other areas along the slope, and (5) to use this information to assess the remaining potential of an oil and gas field.

1.2 Study Area

The study area is an oil and gas field along the slope adjacent to the Northwest Shelf (Figure 1.1) that has been producing from the Second Sand and Second Carbonate Members for approximately 20 years. This field is an excellent candidate for an integrated seismic attribute analysis because: (1) the Second Sand Member is a heterogeneous assemblage of overlapping submarine fan deposits containing reservoir quality rocks in multiple facies, resulting in a complex porosity distribution that is difficult to adequately model using well data alone, (2) there is an excellent data set available consisting of good quality, modern well log suites, core data, production data, and a 3-D reflection seismic survey, and (3) this field can be used
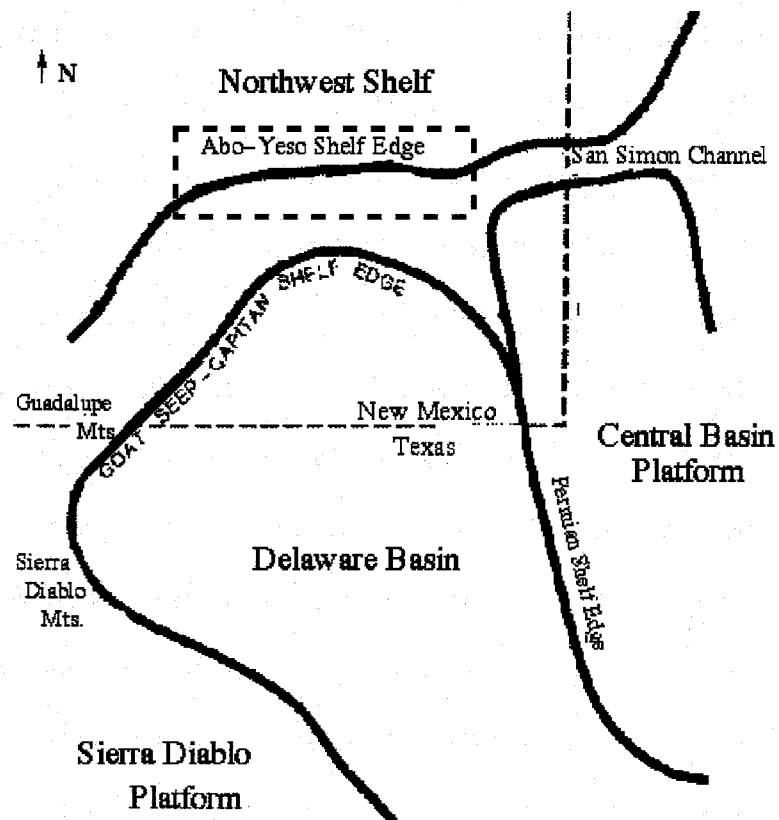
Figure 1.1: The Delaware Basin of southeast New Mexico and west Texas. The approximate location of the study area is indicated by the dashed box. Due to the propriety nature of the seismic data, the exact location of the study area is not shown (adapted from Gawloski, 1987).

as an analog for other areas along the slope. Porosity was chosen as the reservoir property to estimate in this study because, as in other areas along the slope, traps are primarily stratigraphic (upslope pinchouts and lateral facies variations) or diagenetic (varying degress of dolomitization), and the primary drilling targets are thick regions of high porosity.

1.3 Volume-Based Attribute Analysis

Seismic-guided reservoir characterization, the process of using seismic attributes to estimate physical properties of reservoirs, is becoming increasingly common in the oil industry. While the theory behind attribute-physical property relationships lags behind the applications, numerous case studies have shown that this approach can significantly improve predictions of reservoir properties over more traditional approaches such as kriging (e.g., Schultz et al., 1994; Corbett et al., 1995; Gastaldi et al., 1997; Raeuchle et al., 1997; Russell et al., 1997; Watts et al., 1997; Kidney and Sterling, 1998; Schuelke et al., 1998). However, because of the numerical nature of the attribute data and the often necessarily empirical approach, there is a tendency to treat these data as variables divorced from geology and to rely heavily on statistical significance (e.g., correlation coefficients and exclusion testing) for validation of the results. As the number of attributes available for this type of analysis continues to increase (>350 at present), so does the probability of observing spurious correlations (statistically significant yet meaningless results), and additional validation beyond statistical significance is crucial if attribute-based predictions are to be trusted. While most workers would agree that statistical significance is only one measure of validity, and that predictions should be geologically and geophysically plausible as well, few published studies directly address the need to integrate the geologic "variable" in the analysis.

Because of the thickness of the Second Sand within the study area (400'-600'), traditional horizon-based attribute analyses were unable to predict the porosity with the desired accuracy

(Pearson and Hart, 1998), and a volume-based approach was used instead. This is a relatively new technique that involves predicting reservoir properties in the x, y, and z directions with the end result being a physical property *volume*. This approach has substantial advantages over traditional horizon-based techniques in that it can be used to model small variations in reservoir properties that could be lost in the averaging process using a horizon- or interval-based approach and the resulting porosity volume provides considerably more detailed information about the distribution of reservoir properties. At present, with the exception of a few brief reviews (cf. Russell *et al.*, 1997; Schuelke *et al.*, 1998), there are no detailed studies in publicly available literature that document how a volume-based attribute analysis can be integrated with a knowledge of the geology to create a comprehensive reservoir model. Consequently, this study will provide useful information about this technique that has clear applications for many heterogeneous reservoirs where traditional attribute analyses have failed.

1.4 Thesis Overview

In this study it will be shown that the Second Sand was deposited under conditions of fluctuating relative sea level and varying siliciclastic sediment supply that resulted in the formation of a basin-floor fan, a slope fan, and a modified prograding wedge and that in contrast to most lowstand systems tract models, the best quality reservoir rocks within this field occur within the slope fan. It will also be shown that the porosity of Second Sand can be predicted using a combination of five seismic attributes. Lastly, it will be shown that by using an integrated approach to the attribute analysis it was possible to locate potential drilling targets within the slope fan and eliminate targets that were geologically and geostatistically unreasonable. This type of integration and validation of results can and, perhaps, should be used in other areas to assess the results of attribute-based predictions.

The study will be presented in two parts: a geologic section and a geostatistical section. Chapters 2 through 4 address the geologic phase of the study and will cover, in order,1) the study area and project data base, 2) the methods used in the geologic interpretation, and 3) the results and discussion of the geologic interpretation. The geostatistical phase of the study will be presented in Chapter 5 and will include both the seismic-guided estimation of log properties and the integration of these results with the geologic phase of the study.

2. Previous Work and Project Data Base

2.1 Study Area

2.1.1 Geologic setting

The Bone Spring Formation, the slope and basinal equivalent of the Abo and Yeso Formations on shelf, is a Leonardian (Permian) age deposit that occurs in the Delaware Basin of southeastern New Mexico and west Texas (Figure 2.1). During this time, the Delaware was a deep, subsiding basin surrounded by rimmed carbonate platforms (Figure 2.2). Along

SYSTEM	SERIES	DELAWARE BASIN	CENTRAL BASIN PLATFORM	EASTERN SHELF	SLOSS SEQUENCES
QUATERNARY	Holocene	Holocene Sand	Holocene Sand	Alluvium	Tejas
TERTIARY	Pliocene	Ogallala	Ogallala	Gravels	
CRETACEOUS	Gulfian Comanchean	Limestone Sand	Limestone	Limestone	Zuni
JURASSIC	Absent	/////	/////	/////	
TRIASSIC		Dockum	Dockum	Dockum	
PERMIAN	Ochoa	Dewey Lake / Rustler / Salado / Castile	Dewey Lake / Rustler / Salado	Dewey Lake / Rustler / Salado	Absaroka
PERMIAN	Guadalupe	Bell Canyon / Cherry Canyon / Brushy Canyon (Delaware Mt.)	Tansill / Yates / SevenRivers / Queen / Grayburg (Artesia Gr.)	Artesia Group	Absaroka
PERMIAN	Guadalupe	Victorio Peak	San Andres / Glorieta Ss.	San Andres / San Angelo	Absaroka
PERMIAN	Leonard	Bone Spring Limestone	Clear Fork / Wichita-Abo (Yeso)	Clear Fork / Wichita	Absaroka
PERMIAN	Wolfcamp	Wolfcamp	Wolfcamp	Wolfcamp	Absaroka
PENNSYLVANIAN	Virgil	Cisco	/////	Cisco	Absaroka
PENNSYLVANIAN	Missouri	Canyon	/////	Canyon	Absaroka
PENNSYLVANIAN	Des Moines	Strawn	Strawn	Strawn	Absaroka
PENNSYLVANIAN	Atoka	Atoka	Atoka	Bend	Absaroka
PENNSYLVANIAN	Morrow	Morrow	Morrow	Bend	Absaroka
MISSISSIPPIAN	Chester	Barnett	/////	/////	Kaskaskia
MISSISSIPPIAN	Meramec	Mississippian Limestone	Osage-Meramec	Mississippian Limestone	Kaskaskia
MISSISSIPPIAN	Osage	Mississippian Limestone	Osage-Meramec	Mississippian Limestone	Kaskaskia
MISSISSIPPIAN	Kinderhook	Mississippian Limestone	Kinderhook	/////	Kaskaskia
DEVONIAN	Upper Middle	Woodford / Thirty one	Woodford / Thirty one	/////	Tippecanoe
SILURIAN	Middle	Wristen / Fusselman	Wristen / Fusselman	/////	Tippecanoe
ORDOVICIAN	Upper Middle	Montoya / Simpson	Montoya / Simpson	/////	Tippecanoe
ORDOVICIAN	Lower	Ellenburger	Ellenburger	Ellenburger	Sauk
CAMBRIAN	Upper	Cambrian	Cambrian Ss.	Cambrian Ss.	Sauk
PRE CAMBRIAN		Pre Cambrian	Pre Cambrian	Pre Cambrian	

Figure 2.1: Stratigraphic column for the Delaware Basin and adjacent regions (Frenzel *et al.*, 1988).

PALEOGEOGRAPHIC MAP
OF
WEST TEXAS & SOUTHEAST NEW MEXICO
DURING LATE WOLFCAMP (EARLY PERMIAN) TIME
ABOUT 205,000,000 YEARS AGO
BY W. FLOYD WRIGHT
GEOLOGIST
MIDLAND, TEXAS
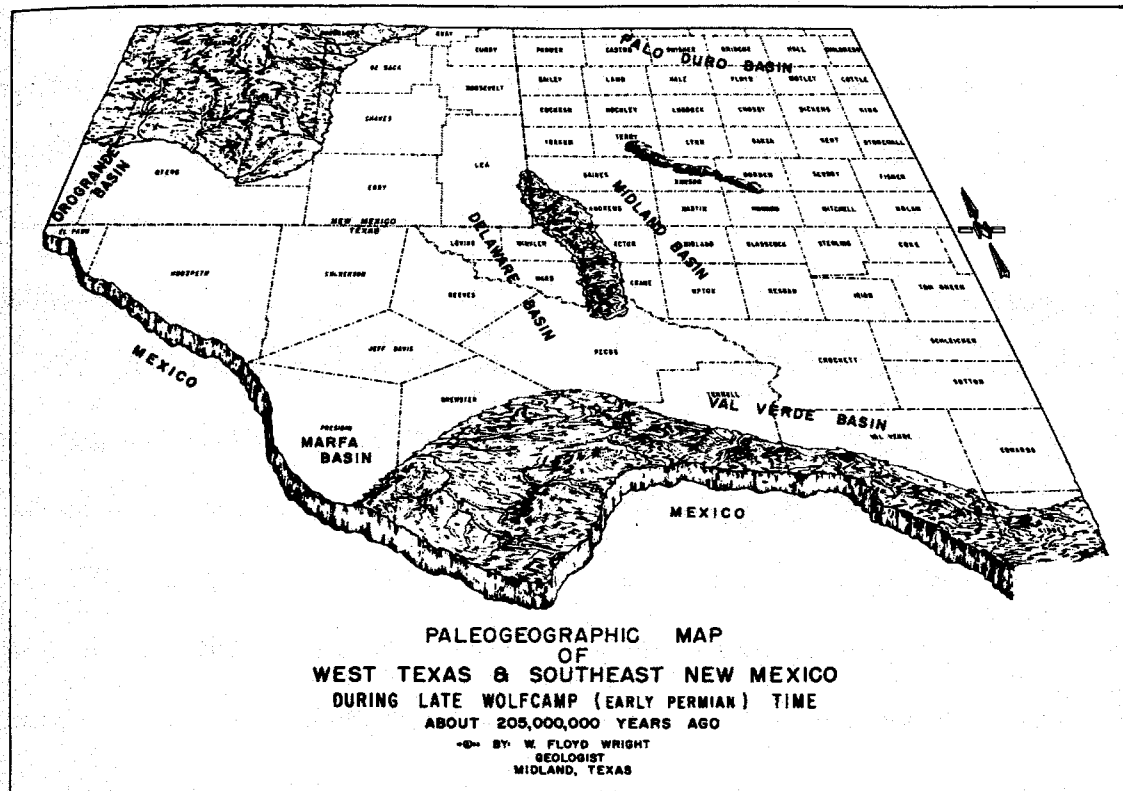
Figure 2.2: Paleogeographic reconstruction of the Delaware Basin during the Early Permian (Frenzel *et al.*, 1988)

the northern margin of the basin, the depositional relief is estimated to have been approximately 1,500'-2,000' (Wiggins and Harris, 1983; Gawloski, 1987) with localized variations in shelf progradation and vertical building due to variations in subsidence rates and underlying structure (Saller *et al.*, 1989).

The Bone Spring Formation is a mixed carbonate and siliciclastic sequence with a maximum thickness of 1067 m (3500') that is believed to be the result of reciprocal highstand-lowstand sedimentation (Silver and Todd, 1969; Gawloski, 1987). The Bone Spring Formation has been informally subdivided into six members which are, in order of increasing depth, the First Carbonate, the First Sand, the Second Carbonate, the Second Sand, the Third Carbonate, and the Third Sand (Figure 2.3).

The Bone Spring carbonates are believed to have been deposited during relative sea level highstands when the shelves were flooded, and carbonate production was at a maximum. The carbonates consist largely of spiculitic, carbonaceous wackestones and lime mudstones (basinal), laminated dolomitic mudstone (slope), and dolomitized megabreccias (slope) (Gawloski, 1987).

The siliciclastic members, in contrast, are thought to have been deposited during periods of falling sea level and relative sea level lowstands. Sediment may have been brought to the shelf edge by fluvial and/or aeolian processes (Silver and Todd, 1969; Messa *et al.*, 1996; Hart, 1997; Montgomery, 1997). This sediment was later redistributed by submarine gravity flows into a complex assemblage of overlapping submarine fan lobes along the slope and extending out into the basin (Messa *et al.*, 1996). The siliciclastic units are gray, fine to very
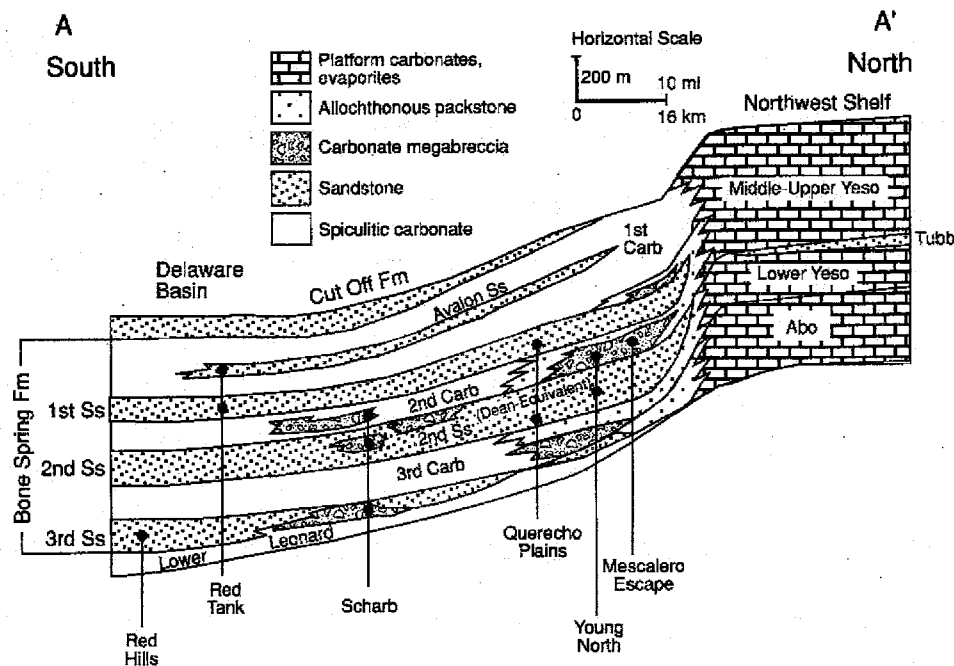
Figure 2.3: Schematic cross-section through the northern Delaware Basin from the shelf margin (right) south out into the basin (left) showing the members of the Bone Spring Formation and the intervals from which several of the Bone Spring fields produce oil and gas (Montgomery, 1997).

fine, silty, angular, moderate to well sorted, laminated, locally crossbedded, dolomitic subfeldspathic quartz arenites and siltstones. The primary porosity is partially occluded by dolomitic cement, quartz overgrowths, pore-filling clays (clay content may be as high as 15 %), and minor amounts of siderite and authigenic pyrite (Gawloski, 1987; Saller *et al.*, 1989). These sediments are interpreted as turbidite deposits. Complete Bouma sequences are rarely seen due to the fine-grained nature of the sediment (Gawloski, 1987; Messa *et al.*, 1996). Carbonate debris flow deposits similar to those found in the Second and Third Carbonates occur as discrete lenses within the Second and Third Sands.

Previous work on the Second Sand Member by Messa *et al.* (1996), reproduced by Montgomery (1997), based on analyses of well logs and core samples showed that within the study area the Second Sand contains three fine-grained, silty quartz sands, informally named the "A", "B", and "C" sands, separated by layers of dark silty dolomite. The deepest of these sands, the "C" sand, is the best quality reservoir and has been the most extensively studied. Cores from the "C" sand show that it consists of a ripple-crossbedded channel facies, a laminated levee/overbank facies, a levee/overbank slump facies, and a pelagic facies. Similar facies relationships are presumed by Messa *et al.* (1996) to exist in the other two sands. The channel and overbank/levee facies form the best reservoirs with average core porosities of 10.31% and 9.1%, respectively.

2.1.2 Production history

Production within the study area is from porous zones within the Second Bone Spring Sand as well as from lenses of dolomitized megabreccias within the overlying Second Bone Spring Carbonate (Messa *et al.*, 1996; Montgomery, 1997). The most productive region occurs in the north central portion of the field (Figure 2.4). The permeability is typically low (<6 md), and

9
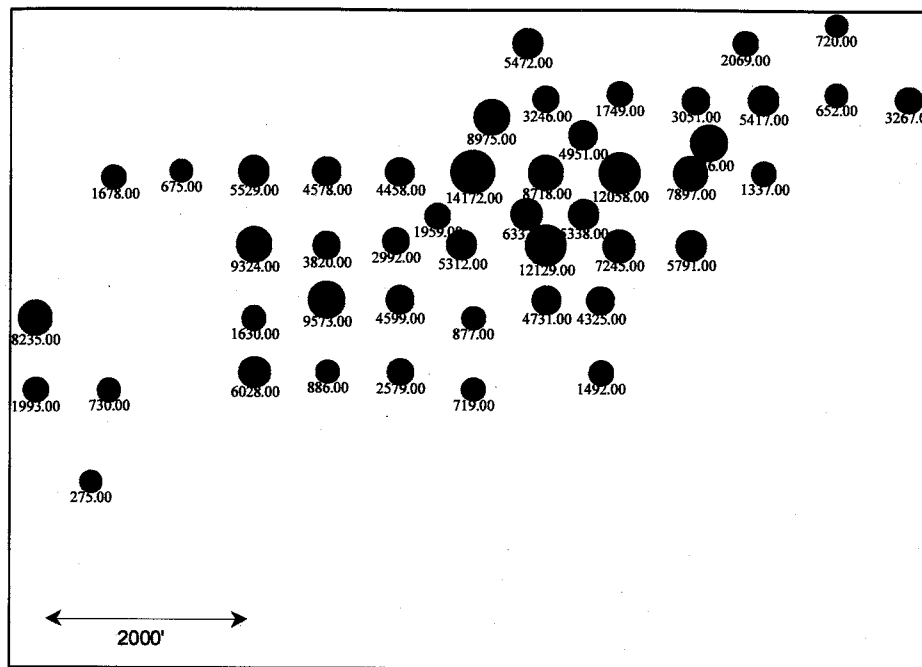
Figure 2.4: Maximum monthly oil production (barrels) for wells within the field. Production is comingled from the Second Carbonate and Second Sand. North is vertically up.

producing wells are often sand-fractured to increase their effective permeability (Gawloski, 1987). Production is enhanced in some areas by solution gas drive (Montgomery, 1997). Production peaked in 1990 and has declined fairly steadily since then (Figure 2.5). However, significant reserves do still remain (estimated at over 20 million barrels of original oil in place), and there will undoubtedly be continuing interest in this field (Montgomery, 1997). Upslope pinch outs and complex facies relationships within the Second Sand make a detailed knowledge of the stratigraphy and porosity distribution essential for determining the best locations for infill drilling.

2.2 Project Data Base

The data set used in this study consists of a 3-D seismic survey, wireline logs from 34 wells within the survey area, production data for all wells, and the results of a previous study of core samples.

Total Oil Production & Number of Wells
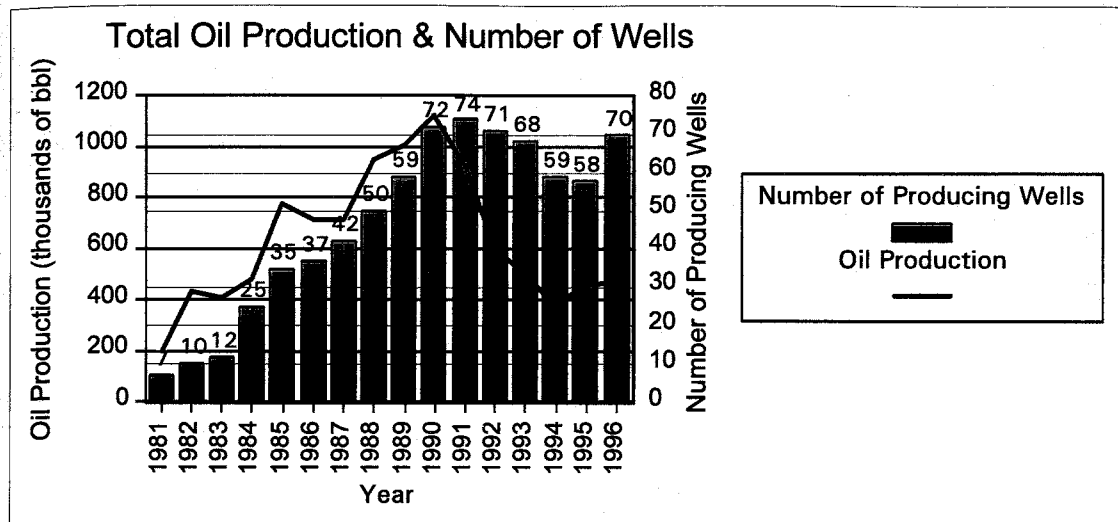
Figure 2.5: Yearly oil production for the field from 1981 to 1996 (curve) and the number of wells producing during a given year (bars).

2.2.1 Seismic data set

The 3-D seismic survey covers an area measuring approximately 2.4 by 2.4 miles (~5.75 mi^2) with bins measuring 110' x 110'. The survey was shot on a rectangular grid using a Vibroseis source. Crosslines trend north-south, approximately perpendicular to the regional strike at the Bone Spring level. The data extend from the surface down to 2 s and is sampled at 2 ms intervals. The seismic data is post-stack time-migrated with processing performed by the acquisition company that provided the data. Additional post-stack processing was limited to the application of a time-varying gain function. This was applied only to aid in interpretation by making deeper reflections easier to track throughout the volume.

Data quality varies with depth; acquisition footprints dominate in the uppermost 500ms of the volume (Figure 2.6), but this gradually fades and is not of consequence at the Bone Spring level (>700 ms). Vertical striping is also a prominent feature on the boundaries of the survey. Because this data set is part of a much larger seismic survey, this is probably due to static correction problems rather than low fold in these areas. Although a bandpass filter was

11
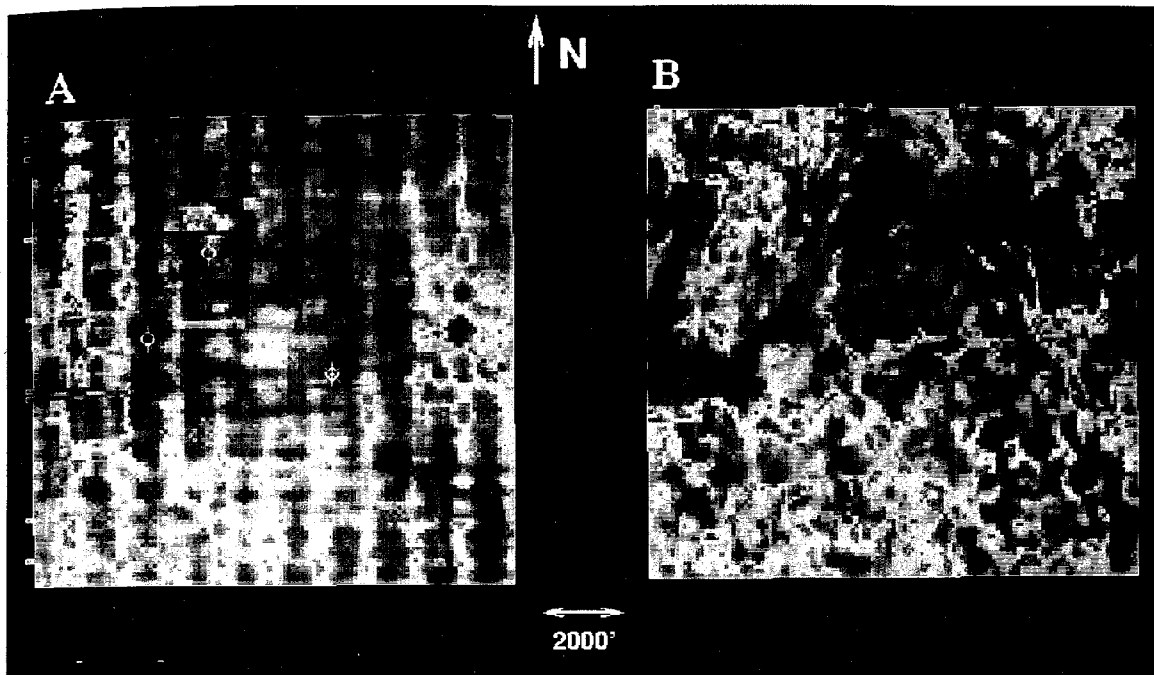
Figure 2.6: Amplitude maps from a shallow unit (left, the Seven Rivers Formation occurring between 415ms to 480ms) and from the top of the Second Sand (right). The prominent checkerboard pattern of the amplitude map on the left is a reflection of the survey pattern (i.e. an acquisition footprint). While there are still some possible remnants of this pattern at depth, it clearly is no longer the dominant feature on the amplitude map.

applied in the processing phase, some noise is still present and can be seen when an F-K fan filter (a filter that operates on data in the frequency-wavenumber domain) is applied (Figure 2.7) to remove events with dips outside the range of +/- 6ms between traces (roughly the maximum stratigraphic dip seen in the data). Although these data quality issues did not significantly hinder the geologic interpretations, they did affect the reservoir characterization results to be discussed later.

2.2.2 Wireline logs

Well logs were available for 34 wells within the study area. The well spacing is on average approximately 0.25 miles, and the wells cover a NE-SW 1.2 mile wide swath of the study area with a few additional wells providing control in the southernmost portion of the area
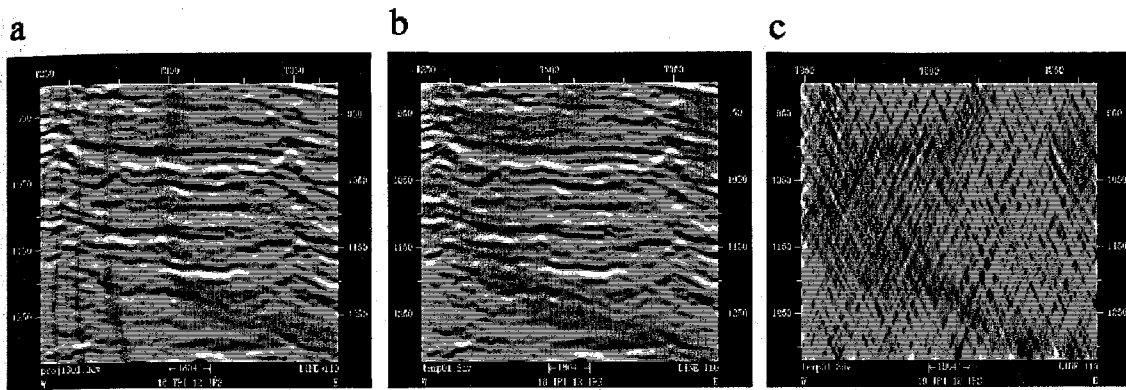
Figure 2.7: a) 2-D seismic transect through the unfiltered seismic data, b) the same seismic transect after application an F-K filter to remove only the most steeply dipping noise, and c) the data rejected (removed) by the F-K filter. While most of the steeply dipping rejected data is clearly noise, a close inspection does reveal a faint impression of stratigraphy.

(Figure 2.4). Digitized log suites typically contain gamma ray logs, deep, medium, and shallow resistivity logs, neutron porosity logs, bulk density or density porosity logs, and caliper logs. For some wells, photoelectric factor and sonic logs were also available. All of the logs are sampled at 2' intervals with the exception of the sonic logs which have a 0.5' sampling rate. All density and neutron porosity logs were based on a limestone matrix. With few exceptions, the logs vary in age from 1980-1997. Because the majority of the logs were recorded after 1980, having significantly different vintages of logs (i.e., old, outdated tools vs. modern tools) was not a problem.

2.2.3 Core data

Also available for this project were the results of a detailed core study conducted by an independent consultant for the Harvey E. Yates Company. These results include facies descriptions, cross-sections, core porosity, and petrographic work. The core spans a total of 250' and was taken from four wells within the study area (Figure 2.8).
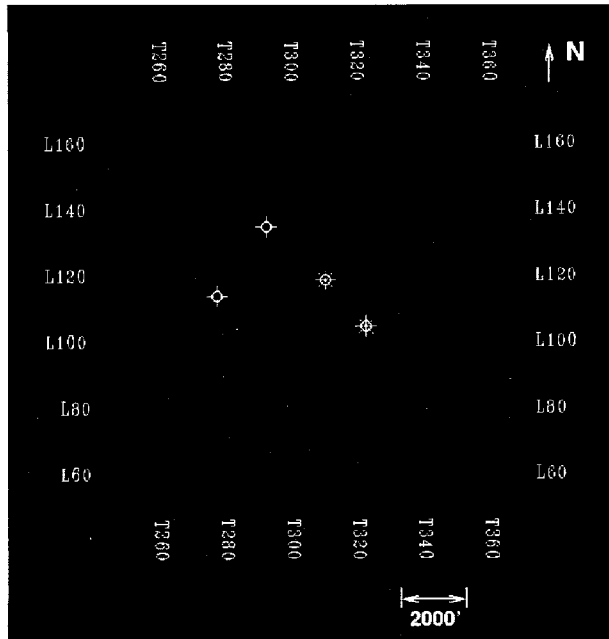
Figure 2.8: Map view showing the locations of wells which have been cored in the Second Sand interval.

3. Geologic Interpretation of Seismic Data—Methods

The data set (seismic and well data) was loaded into Landmark Graphics' Seisworks interpretation package, available at the New Mexico Bureau of Mines and Mineral Resources, for the geologic interpretation phase of the study. While these procedures are commonly used in industry, they are seldom, if ever, documented in publicly available literature. Consequently, I will describe them in detail. Readers unfamiliar with the geologic interpretation of seismic data, should see Appendix 1.

3.1 Gain Function

Because our seismic data had already been processed, the only "in-house" processing necessary was to apply a gain function that varied exponentially with depth. This function was applied iteratively until the optimal gain function for display purposes was found.

3.2 Procedure for Tying Well Data to Seismic Data

The first step in interpreting the data was making the well-seismic tie. Although six sonic logs were available within the area of the 3-D seismic survey (Table 3.1), no checkshot data or vertical seismic profiles were available to calibrate the sonic logs. Consequently, the method used in creating the well-seismic tie was somewhat more involved than usual. Each of the six wells was successfully tied to the seismic data via the method described below using Hampson-Russell's STRATA, a stratigraphic analysis and inversion software package.

Well Name	Log Vintage	Well Total Depth	Sonic Log Starting Depth	Sonic Log Ending Depth	Density Logs Available?	Porosity Logs Available?	Sampling Rate (sonic log)
Well #1	1990	11000'	2900'	11000'	Yes	Yes	0.5'
Well #2	1968	12096'	712'	12050'	No	No	0.5'
Well #3	1991	9291'	6407.5'	9250'	Yes	Yes	0.5'
Well #4	1995	9100'	2727.5'	9060'	Yes	Yes	0.5'
Well #5	1991	10950'	8250'	10950'	Yes	Yes	0.5'
Well #6	1984	9330'	2800'	9300'	Yes	Yes	0.5'

Table 3.1: Sonic log information

Well-seismic tie procedure:

1. The sonic log was examined for washouts, portions of the well where the formation has caved in or been damaged, and for regions of bad data, characterized by very spiky, unrealistic log values. The washed out zones were identified using caliper logs and sonic logs. Caliper logs measure the diameter of the hole in inches, and high values indicate washouts. Where washouts occurred, a zone of extreme low velocity (<10,000 ft/s) was recorded due to the greater distance that the acoustic signal traveled through the drilling mud. The washouts were corrected by replacing the low velocities with more appropriate values. The corrected values were determined by examining the sonic log responses above and below the washed out zone and interpolating between these zones. If possible, the sonic log being corrected was also compared with the responses recorded for the same interval at nearby locations. Where extreme transit times (generally <<10,000 ft/s or offscale) were recorded, the remaining logs in the suite were evaluated to determine if there was any possible geological reason for the extreme values. For example, if the photoelectric factor, gamma ray, and resistivity curves all showed an interval to be a fairly uniform, clean sand while the sonic log appeared very spiky with extreme high and

low values, the sonic data were considered suspect, and the largest spikes were replaced with more reasonable values. If it was still ambiguous after examining the log suite, the sonic log was not edited.

2. The edited sonic log was integrated with respect to depth to give two-way travel times, and this time-depth relationship was used to convert the density and sonic logs to two-way travel time.

3. If a density log was unavailable, an estimate of the density log was calculated using Gardner's rule.

4. The sonic log was converted to a velocity log and multiplied by the density log to produce an acoustic impedance log.

5. The reflectivity series was calculated from the acoustic impedance log

6. A statistical wavelet was extracted from the seismic data, assuming the phase spectrum is zero. For the interested reader, the theory behind wavelet extraction techniques is described in greater detail in Appendix 1. The steps implemented by the software program in the wavelet extraction are as follows:

   i. *Specify a time window and the traces to be used in the extraction.* Wavelet extraction was performed within a time window of 500-1000 ms using a taper of 10 time samples (20 ms) or ¼ of the window length, whichever was less. The time window covers the majority of the Bone Spring Formation, and trace data was limited to traces within a capture radius of 110' from the wellbore (a total 5 traces per well location).

   ii. *Calculate the autocorrelation of the data window.* The length of the autocorrelation is equal to half of the length of the desired wavelet (user specified). The length of the wavelet used in this step was estimated by examining the autocorrelation function for various traces

throughout the data set. The length (in time) of the first large amplitude segment of the autocorrelation function was taken as the length of the wavelet (cf. Yilmaz, 1987).

    iii.   *Calculate the amplitude spectrum of the autocorrelation, and estimate the wavelet in the time domain.*

    iv.   *Sum the wavelets from each trace within the capture radius to produce the final wavelet estimate.*

7. The extracted wavelet was convolved onto the reflectivity series to create a synthetic seismogram. The purpose of this synthetic was not to get a good character match with the seismic data, but only to remove bulk time shifts and get a good preliminary time-depth relationship. This step was critical because there were no checkshot surveys.

8. The match between the synthetic and the seismic data near the well location was evaluated by (1) a visual examination, (2) a cross correlation plot, and (3) the correlation coefficient. In order to be considered acceptable at this point, the synthetic seismogram and the seismic data must look similar in terms of major reflection events, the correlation coefficient must be greater than approximately 0.40, and the correlation graph must be symmetric with its maximum at zero.

9. If step 8 did not produce an acceptable match, the prominent peaks and troughs on the synthetic were identified in the seismic data, and the logs were stretched and squeezed or a bulk time shift was applied to align these events. Such stretching, squeezing, and shifting was unavoidable given the lack of checkshot surveys and VSP data with which to calibrate the log. It should be emphasized, however, that after an initial bulk shift to

account for the shallower portion of the well where no sonic data was available, the adjustments needed were fairly minor (generally less than 10 ms).

10. The match between the synthetic seismogram and the seismic data was re-evaluated (step 8).

11. A new wavelet was extracted using both the well data and the seismic data. The purpose of this additional wavelet extraction was to obtain a better character match between the synthetic seismogram and the seismic data. This made it possible to identify in the seismic data the individual zones (the "A", "B", and "C" sands) within the Second Sand that were seen in the log data. This type of well-seismic wavelet extraction seeks to resolve the wavelet problem by calculating the least squares shaping filter which solves the following:

$$s(t) = w(t)*e(t)$$

where e(t) is again the reflectivity series of the earth. Because the number of time samples in the wavelet is generally much less than the number in s(t), and the reflectivity series can be calculated from the well log data, this system is overdetermined and can be solved with least squares methods (Yilmaz, 1987). The steps followed in the wavelet extraction are unique to this software package, and as such, are described in detail below.

    i. *Define the trace and time window and extract the sonic, density, and seismic data over this window.* The time and trace windows and the applied taper were defined in the same manner as was used for the statistical wavelet extraction with the added constraint that the well logs have data within the interval and are of good quality.

    ii. *Calculate the least squares shaping filter.* This filter provides an estimate of the seismic wavelet. Instead of calculating a single wavelet from the time window, the goal of this

technique is to extract the "best" wavelet. To this end, the software algorithm extracts wavelets from numerous intervals within the window using a user defined minimum window length and window/wavelet increment. For example, if the time window chosen is 700-1300 ms and the minimum window length is set to 200 ms with a window/wavelet increment of 50 ms, the software will extract wavelets of varying sizes and locations as shown in Table 3.2.

For each of the wavelets extracted, the "effective length criterion" was calculated. This process essentially ranks the wavelets, with the "best" or most compact wavelets with the majority of the energy concentrated at the center being given the smallest effective lengths (Hampson and Galbraith, 1994). In this way the portion of the well log and seismic trace data that produces the best wavelets can be found. This method produces a large number of wavelets. The best of these are averaged to produce a single best wavelet at each trace location.

iii. *Sum the wavelets calculated from all the traces to produce a single best wavelet at the well location.*

iv. *Using the Hilbert transform, calculate the amplitude envelope of the wavelet.*

v. *Filter out high frequency components to stabilize the extracted wavelet.* Frequencies that correspond to amplitudes in the original data that are less than ¼ of the maximum amplitude are set to zero in the extracted wavelet.

Wavelet length (ms)	200	250	300	350	400	450
Window Locations (ms)	700-900	700-950	700-1000	700-1050	700-1100	700-1150
	750-950	750-1000	750-1050	750-1100	750-1150	750-1200
	800-1000	800-1050	800-1100	800-1150	800-1200	800-1250
	850-1050	850-1100	850-1150	850-1200	850-1250	850-1300
	900-1100	900-1150	900-1200	900-1250	900-1300	
	950-1150	950-1200	950-1250	950-1300		
	1000-1200	1000-1250	1000-1300			
	1050-1250	1050-1300				
	1100-1300					

Table 3.2: An example of the wavelets and window locations used in the well log based wavelet extraction.

This type of wavelet extraction requires that the well and seismic data be already fairly well tied. The accuracy of the extracted wavelet depends on the strength of this earlier time-depth relationship. In particular, errors in the time-depth relationship can result in a loss of the wavelet's high frequency component, a "distortion of the phase spectrum", and "unrealistic side lobes" (Hampson and Russell, 1994).

12. A new synthetic based on the semideterministic wavelet described above was created.

13. The match between the synthetic and seismic data was re-evaluated. If the correlation was found to be weak (correlation coefficient < 0.65), steps 6-12 were repeated using different parameters (e.g. choosing a new window for the statistical wavelet extraction, re-evaluating any adjustments made to the logs in step 9, and rechecking for washouts). The correlation time window was restricted to the zone of interest (where the wavelet was

were extracted), but there was generally a good match between the synthetic and the seismic were above the Bone Spring Formation as well.

One remaining question to be addressed regarding the seismic wavelet is: What is the phase of the data? No wavelet processing was done during processing before the data was received for this study. The data were deconvolved, however, to compress the wavelet into a short, near zero-phase wavelet. The wavelets extracted bear out this claim: they are less than 250 ms in length, and the majority of the energy is centered on time zero, though they are not truly zero-phase (see Figure 4.1 in Chapter 4). Post-stack wavelet processing was attempted for this study. Using the knowledge of the wavelet from those extracted, it was possible to create a spatially varying filter that would in theory convert the embedded wavelet to zero-phase. Although numerous shaping filters such as these were created, it was impossible to assess their effectiveness without checkshot or VSP data with which we could calibrate a zero-phase synthetic for comparison. As a result, the only way to evaluate the filtered result was by extracting a new wavelet and seeing if it was indeed zero-phase. Following this strategy, it was shown that none of the filters applied made the data truly zero-phase. It was impossible to determine if this was due to errors in the spatially varying filter (i.e., errors in the extracted wavelet) or due to error in the final quality control wavelet that was extracted. Given this ambiguity, it was decided that wavelet processing would only introduce more unpredictable error.

3.2 Horizon Interpretation Methods

The peaks and troughs corresponding to formation tops and units of interest were identified in the seismic data at the wells that had synthetic seismograms. When the reflection events

22

were not zero phase, the closet peak or trough was chosen. The reflection events (horizons) were then picked on a grid of seed lines

&c: The density of the seed line grids varied from every 5th inline and crossline to every 20th inline and crossline depending on the data quality (e.g., artifacts, acquisition footprints, low S/N), structural and stratigraphic complexity, and reflector continuity. The horizons were picked on a combination of color variable area displays (good for seeing offset reflectors and seismic character), wiggle trace displays (often the easiest way to follow discontinuous reflectors and to look for asymmetric peaks or troughs), and phase displays. After picking the seed lines, the interpretation was then checked by examining loops and arbitrary lines through the data volume to see if the pick was consistent and geologically reasonable.

The horizon was then autotracked throughout the entire volume (Figure 3.1), and the quality of the result was carefully checked. Additional seed lines were added to constrain the autotracker in regions where it had done poorly, and the horizon was autotracked again. This process was repeated numerous times until an acceptable horizon was generated. At this
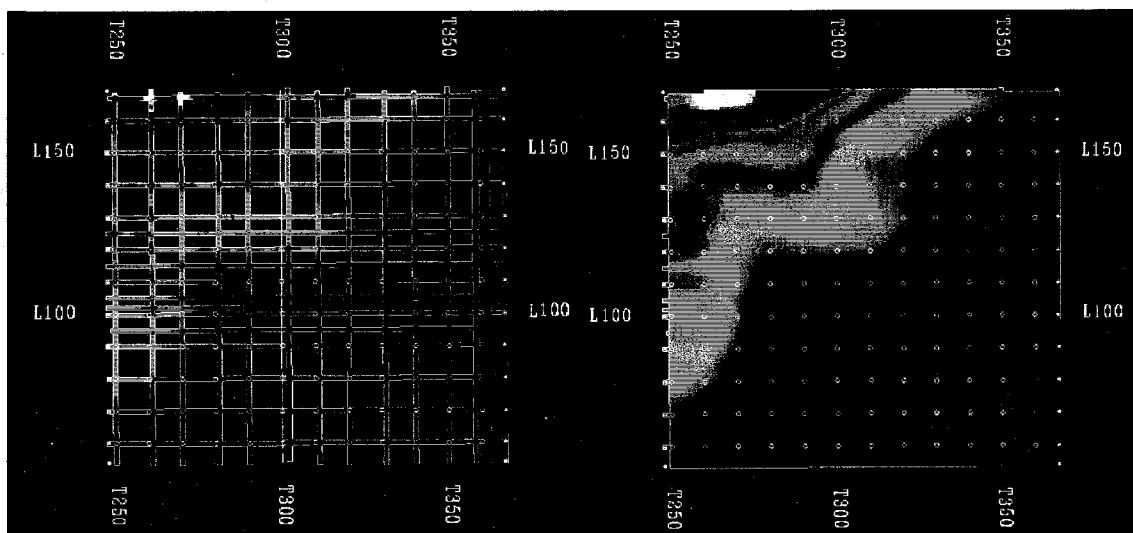
Figure 3.1: An example of the horizon interpretation method: The grid of seed lines (left) picked on 2-D seismic transects, and (right) the final smoothed, autotracked horizon.

point, any remaining "holes" in the horizon that were not being filled in during the autotracking process were filled in by interpolating the horizon (essentially a best fit surface across the holes). Lastly, the horizon was smoothed using an equally weighted, 3x3 or 5x5 trace, smoothing filter to remove the locally erratic nature of the autotracked horizon. The result of this interpretation process was a time structure map. To gain further insight into the geometry of the reservoir, isochron maps were created from the time-structure maps.

The geologic interpretation of the Second Sand was based on an examination of the time-structure maps, isopach maps, and the internal reflector configuration. The internal reflection configuration (i.e., toplap, downlap, onlap, bypass, progradation, etc.) was determined by examining a series of 2-D lines, including crosslines, inlines, and arbitrary lines. As was mentioned earlier, the crosslines are approximately perpendicular to the regional slope at the Bone Spring level, and, as a result, they best illustrate the internal reflection configuration.

3.3 Fault Interpretation Methods

The simplest expression of a fault in seismic data is an offset in reflections. However, if this is to be used as a criterion to recognize faults in seismic data, the throw on the fault must be seismically resolvable. When the throw is small, the fault may be represented by a sharp bend in a reflection across the fault, thinning of units across the fault zone, or by just a discontinuity in the reflection. Because not all faults produce resolvable offset and minor changes in reflection character across a fault may be hard to distinguish from stratigraphic-related character changes, additional methods were necessary to locate faults within the data. The methods used in this study were (1) manipulation of the color palette (Brown, 1996a), (2) continuity (Bahorich and Farmer, 1995; Marfurt *et al.*, 1998), (3) dip maps (Dalley *et al.*, 1989), and (4) first-octave filters (Hardage *et al.*, 1998).

The continuity volume created to locate faults in this study consists of minimum coherency calculated from 4 adjacent traces using a correlation window of 30 ms and a maximum shift of 5 ms, the maximum stratigraphic dip between adjacent traces within the study area. The continuity cube was created using Landmark Graphics' Poststack/PAL program. The first-octave filtered version of the seismic data was used in this study to locate some of the deeper basement faults where the signal-to-noise ratio is low. The filter applied to the seismic data consisted of a 2-8-16-25 bandpass filter.

4. Geology of the Second Bone Spring Sand—Results and Discussion

4.1 Results

Using the procedures described in Chapter 3, the well logs were integrated with the seismic data, and formation tops and units were identified and mapped. The goal of this work was to define the stratigraphy and structure of the Second Sand and in so doing, gain insight into the geologic history of the unit. The results of the study will be presented in this section, and interpretations will be discussed in the following section (4.2). It should be kept in mind that unlike descriptive or quantitative results, the results of a 3-D seismic interpretation can never be completely objective. However, interpretations must: a) be internally consistent, b) integrate and reconcile the different types of data (well logs, seismic, and core data), and c) be geologically plausible. When possible and appropriate, I have tried to include alternative interpretations. That said, the results will be presented in the order in which they were obtained: (1) well-seismic tie, (2) seismic character of horizons identified, (3) basement structures, (4) time-structure maps, (5) internal reflection configuration, and (6) post-depositional deformation.

4.1.1 Well-seismic tie

As outlined in Chapter 3, integrating the well logs with the seismic data is a two-part procedure: (1) preliminary well-seismic tie using a statistical wavelet and (2) a final well-seismic tie based on the semi-deterministic wavelet. The best way to quantify the strength of the correlation between the synthetic and seismic data is with correlation coefficients. The results from the first phase of the well tie procedure are summarized in Table 4.1 below.

Well Name	Correlation Window (ms)	Correlation Coefficient
Well #1	900-1250	0.800
Well #2	1050-1150	0.500
Well #3	850-1170	0.751
Well #4	700-1170	0.428
Well #5	1075-1360	0.633
Well #6	950-1120	0.447

Table 4.1: Preliminary well-seismic tie results

The wavelets used at this point are zero phase (defined to be so) with amplitude spectra that vary with location. In general, this first step results in a good match of major reflections; large acoustic impedance contrasts produce peaks and troughs in the synthetic that can be matched to events in the seismic data, but individual internal reflections between these major events do not correlate well.

The second step of the well tying procedure begins with the extraction of a new wavelet. These wavelets vary with location and are fairly close to zero phase (Figure 4.1). As a result, most major lithologic contacts do correspond to a peak or trough in the seismic data. Using these wavelets resulted in greatly improved well-seismic ties (Figure 4.2). Although these correlation coefficients were restricted to the Second Sand and adjacent units, the correlation is fairly strong even beyond this zone. The strength of the correlations can be best appreciated by a visual comparison of the synthetic and seismic data. By examining Figures 4.3-4.8, it is clear that the new wavelets have done a significantly better job of reproducing the internal reflections of the Second Sand.

a

b
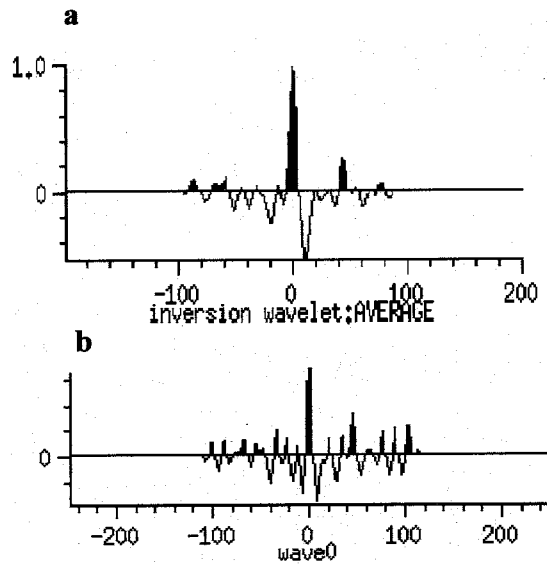
Figure 4.1: Examples of extracted wavelets from phase II of the well tying procedure: a) the arithmetic average of the extracted wavelets, and b) the wavelet extracted at well #1.

Figure 4.2: Final well-seismic tie results

Well #1		900-1250	0.851
Well #2		1050-1150	0.591
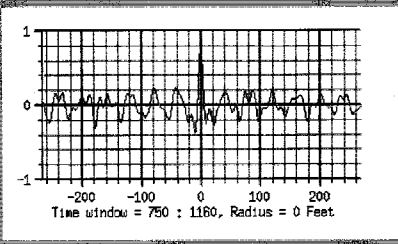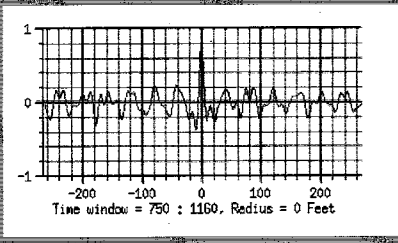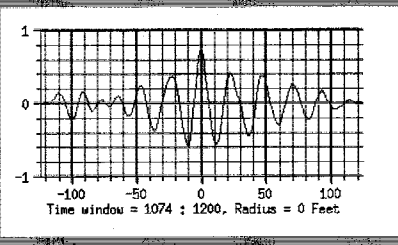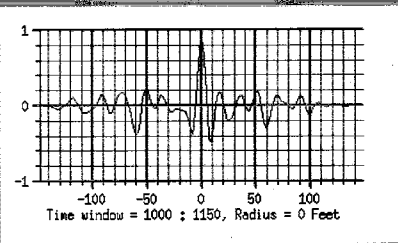
Well #3	Time window = 750 : 1160, Radius = 0 Feet	870-1160	0.799
Well #4	Time window = 750 : 1160, Radius = 0 Feet	750-1160	0.805
Well #5	Time window = 1074 : 1200, Radius = 0 Feet	1075-1360	0.776
Well #6	Time window = 1000 : 1150, Radius = 0 Feet	1000-1150	0.826

Figure 4.2 (cont.): Final results of the well-seismic tie procedure
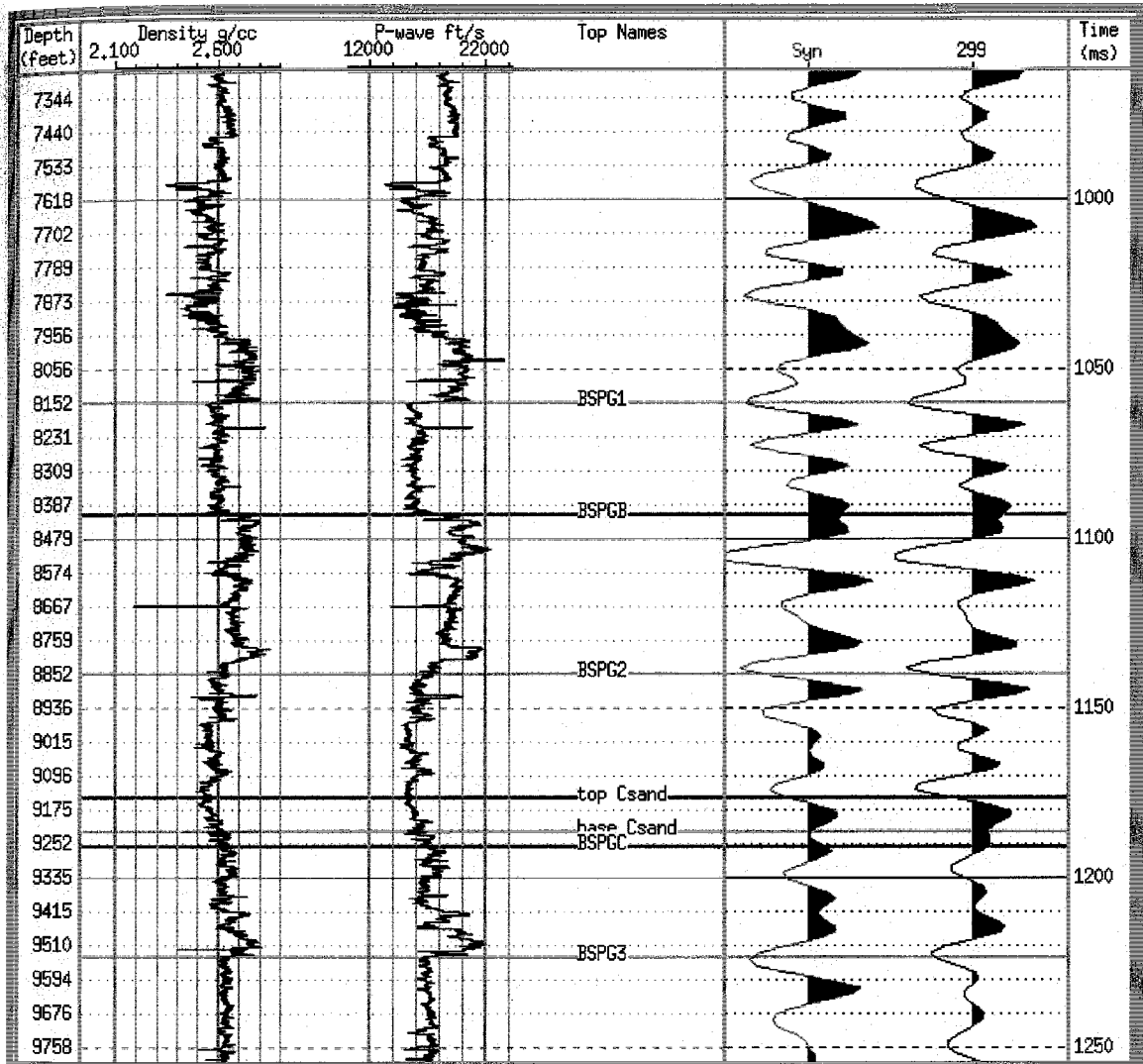
Figure 4.3: Synthetic seismogram at Well #1. From left to right, the curves are 1) density log, 2) velocity log, 3) synthetic trace (blue), and 4) seismic trace (black). The horizontal red lines indicate the position of unit tops: BSPG1, First Sand; BSPG2, Second Sand; top Csand, "C" sand; base Csand, base "C" sand; BSPGC, Third Carbonate; and BSPG3, Third Sand.
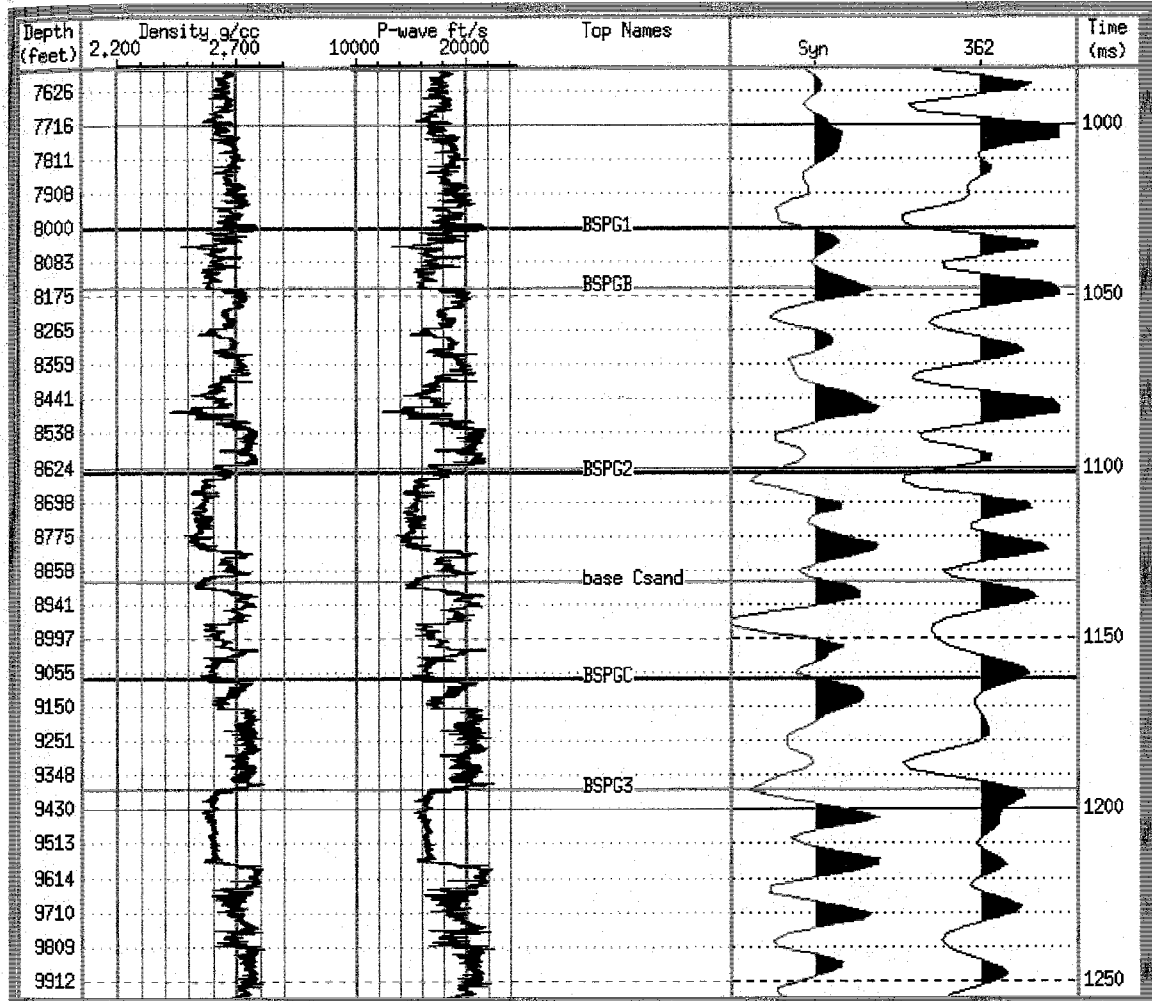
Figure 4.4: Synthetic seismogram at Well #2. From left to right, the curves are 1) density log, 2) velocity log, 3) synthetic trace (blue), and 4) seismic trace (black). The horizontal red lines indicate the position of unit tops: BSPG1, First Sand; BSPG2, Second Sand; BSPGC, Third Carbonate; and BSPG3, Third Sand.
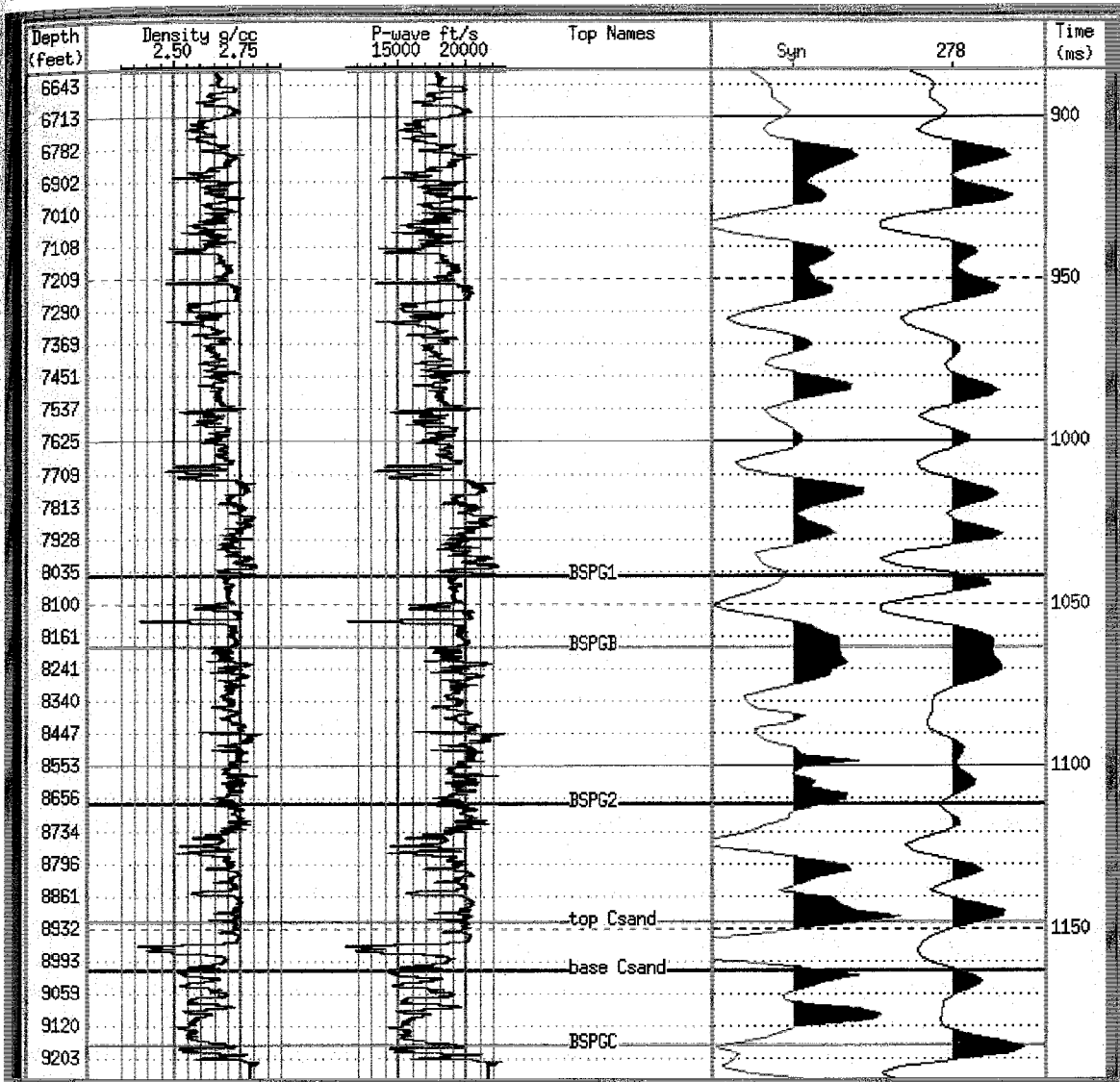
Figure 4.5: Synthetic seismogram at Well #3. From left to right, the curves are 1) density log, 2) velocity log, 3) synthetic trace (blue), and 4) seismic trace (black). The horizontal red lines indicate the position of unit tops: BSPG1, First Sand; BSPG2, Second Sand; and BSPGC, Third Carbonate.
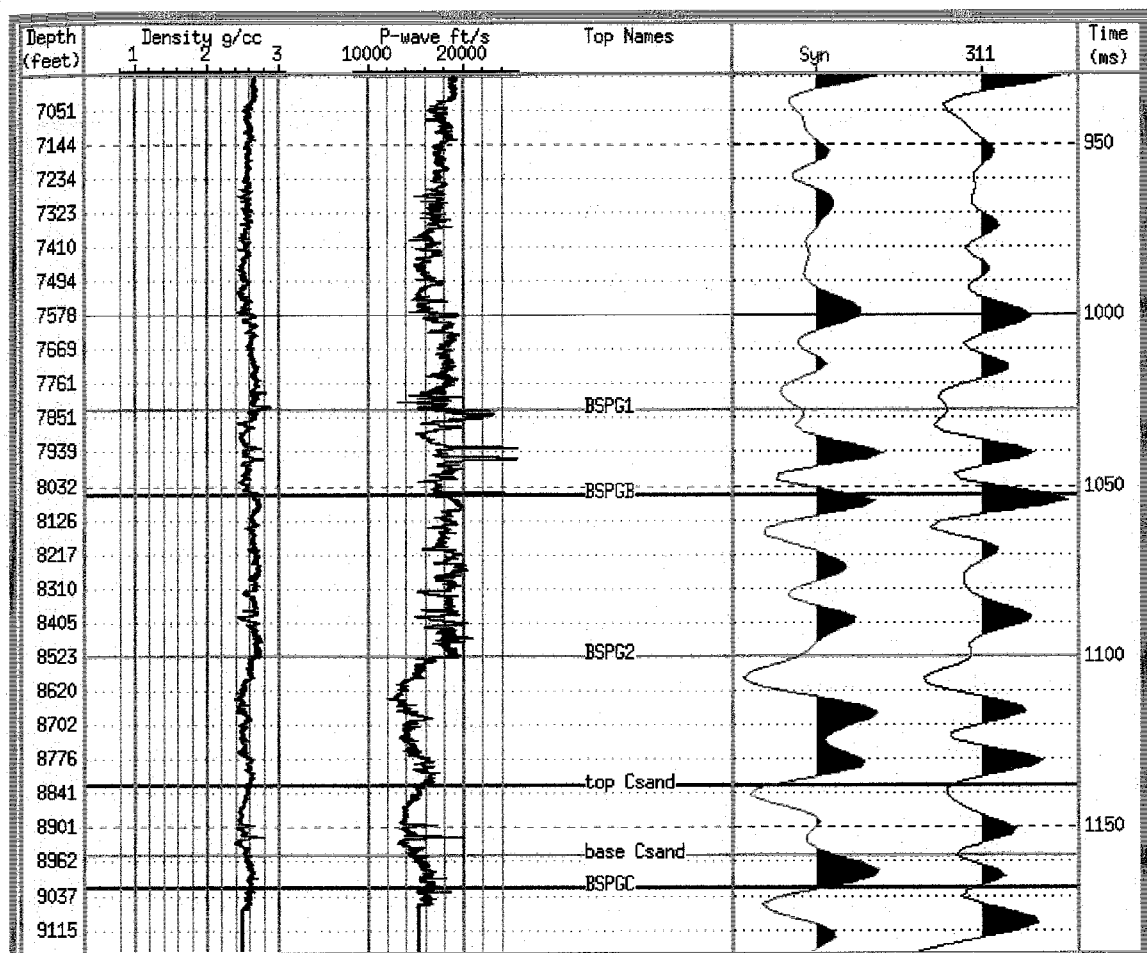
Figure 4.6: Synthetic seismogram at Well #4. From left to right, the curves are 1) density log, 2) velocity log, 3) synthetic trace (blue), and 4) seismic trace (black). The horizontal red lines indicate the position of unit tops: BSPG1, First Sand; BSPG2, Second Sand; BSPGC, Third Carbonate; and BSPG3, Third Sand.
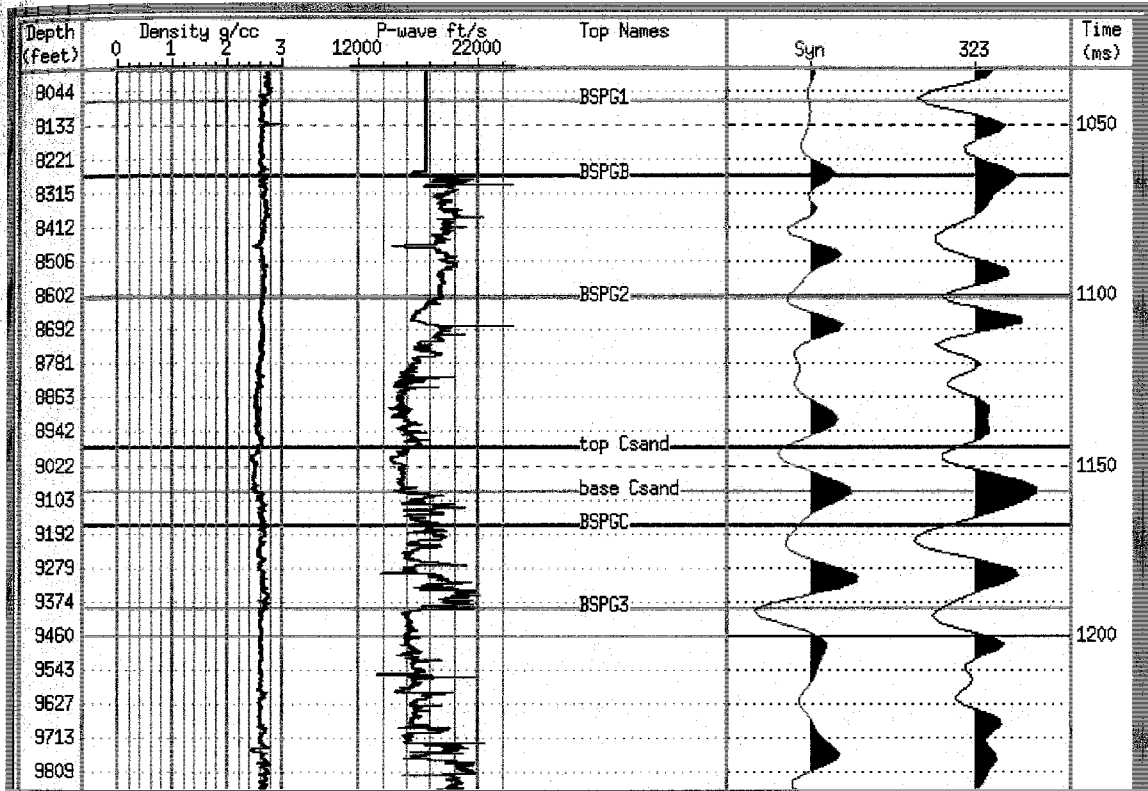
Figure 4.7: Synthetic seismogram at Well #5. From left to right, the curves are 1) density log, 2) velocity log, 3) synthetic t race (blue), and 4) seismic trace (black). The horizontal red lines indicate the position of unit tops: BSPG1, First Sand; BSPG2, Second Sand; BSPGC, Third Carbonate; and BSPG3, Third Sand.
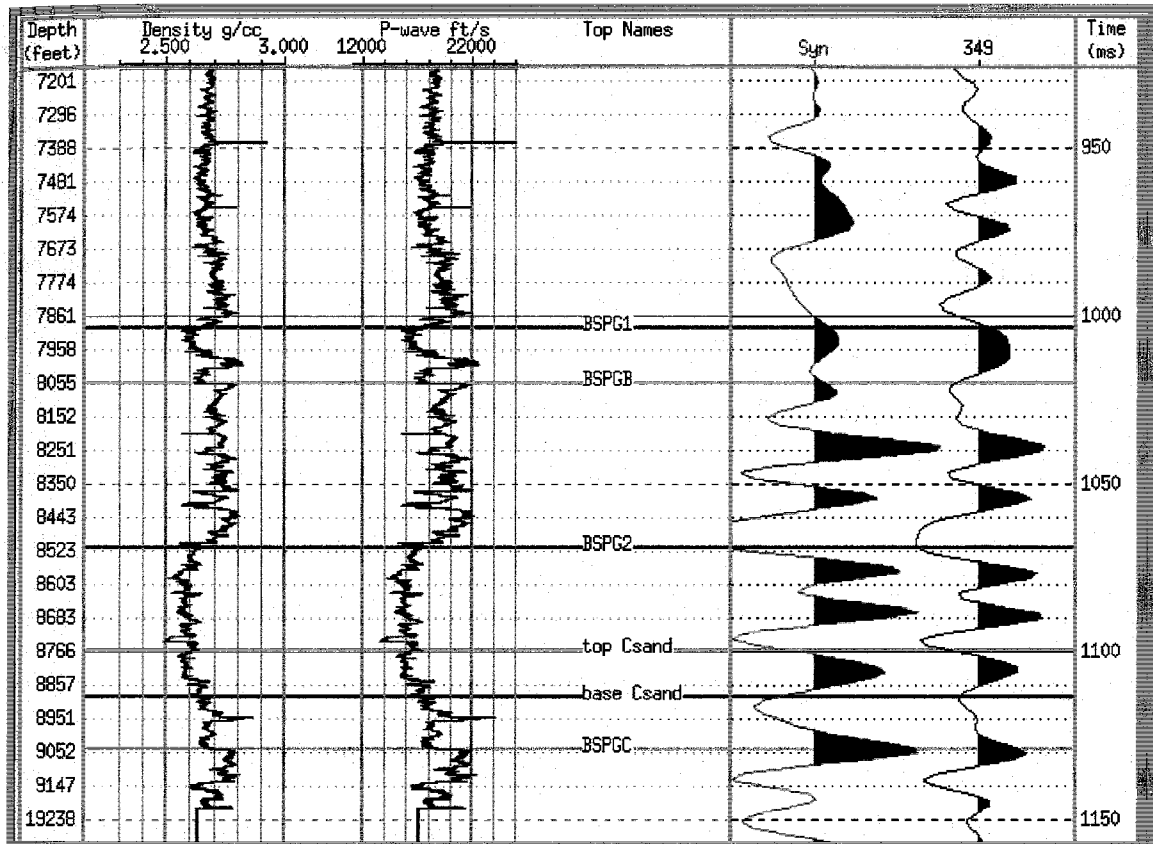
Figure 4.8: Synthetic seismogram at Well #6. From left to right, the curves are 1) density log, 2) velocity log, 3) synthetic trace (blue), and 4) seismic trace (black). The horizontal red lines indicate the position of unit tops: BSPG1, First Sand; BSPG2, Second Sand; and BSPGC, Third Carbonate.

4.1.2 Seismic character of horizons

Based on the synthetic seismograms, the peaks and troughs corresponding to formation tops and other units identified in well logs were located in the seismic data and tracked throughout the volume. Formations both above and below the Bone Spring Formation were identified and mapped to aid in the well tying procedure (Figure 4.9). The seismic character of each of these events as well as the reflection configuration of some intervals are summarized below.

Yates Formation: This pick ranges from 390 ms to 430 ms and consists of a low amplitude trough underlain by a discontinuous low amplitude peak (discontinuities are due to the acquisition footprint) and overlain by a relatively continuous, moderate amplitude peak (Figure 4.9).

Seven Rivers Formation: This pick ranges from 415 ms to 480 ms and is a continuous, moderate amplitude, moderate frequency (which increases markedly to the south) trough that underlies a low amplitude peak.

Queen Formation: This horizon occurs at 440 ms to 560 ms and is a relatively flat horizon marked by a moderate to high amplitude, high frequency trough that is the lower portion of a doublet (a reflection event that is the composite of two peaks or troughs). A discontinuous, low amplitude, high frequency peak separates the upper and lower trough of the doublet. A prominent "checkerboard" acquisition footprint dominates this portion of the survey. The Queen horizon overlies an interval (25 ms thick) of low amplitude highly discontinuous reflections.

Grayberg Formation: This pick ranges from 570 ms to 630 ms and is an undulating, continuous moderate amplitude peak underlying a trough doublet with a discontinuous low amplitude peak at its center. The spacing of the undulations in the Grayberg horizon correlate with the discontinuities in the peak above, both of which are controlled by the acquisition footprint.
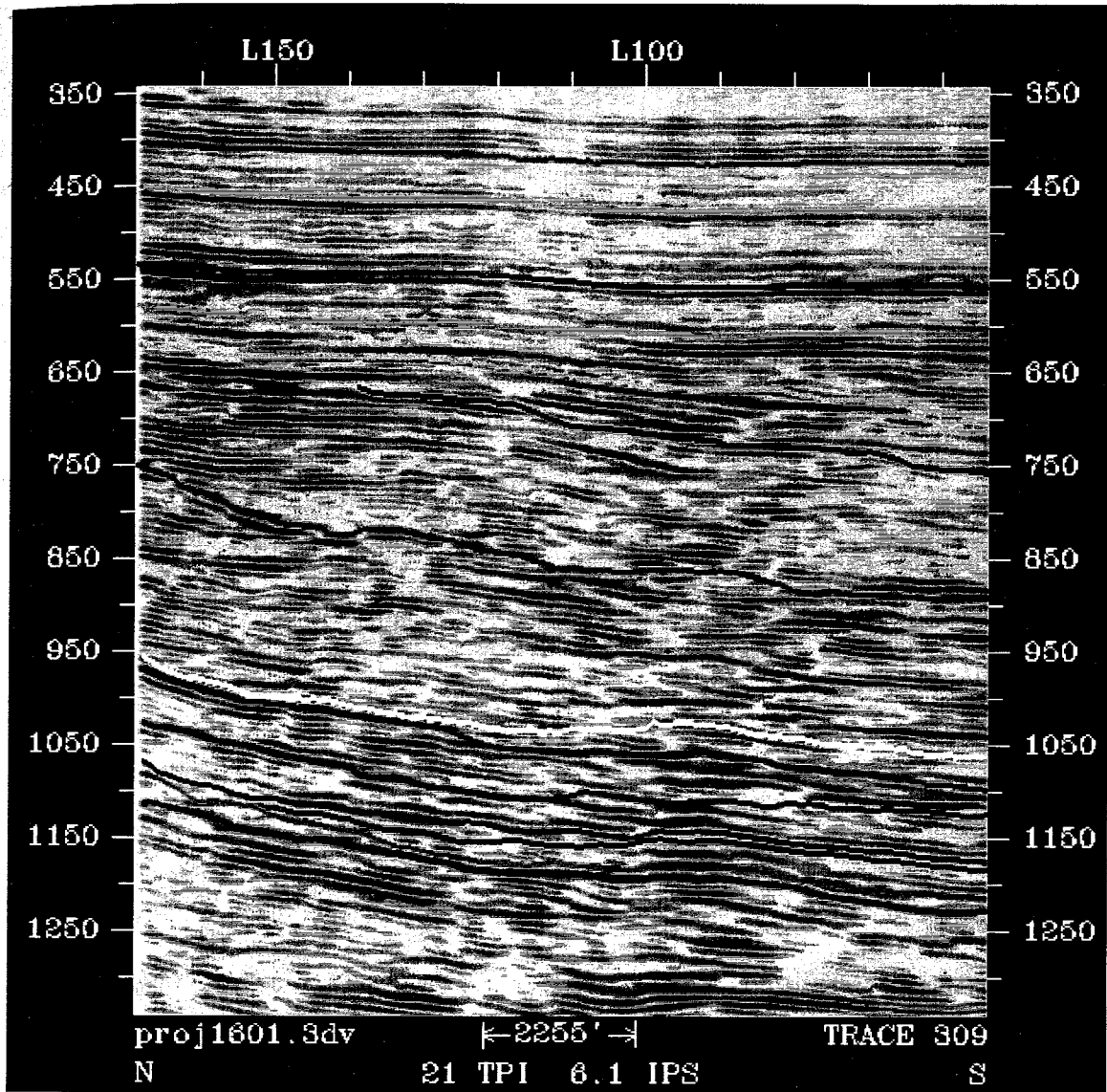
Figure 4.9: N-S seismic transect showing all interpreted horizons. From top to bottom, the horizons shown are: Yates (light purple), Seven Rivers (very pale pink at 450-470 ms), Queen (red at ~550 ms), Grayberg (dark pink), San Andres (light pink), Delaware (black), First Carbonate (purple), First Sand (yellow), Second Carbonate (purple at 970-110 ms), Second Sand (purple), top "C" sand (red), base "C" sand (black), Third Carbonate (green), and Third Sand (red). The vertical axis is two-way travel time (ms). For the transect location, trace 309, see Figure 4.10.
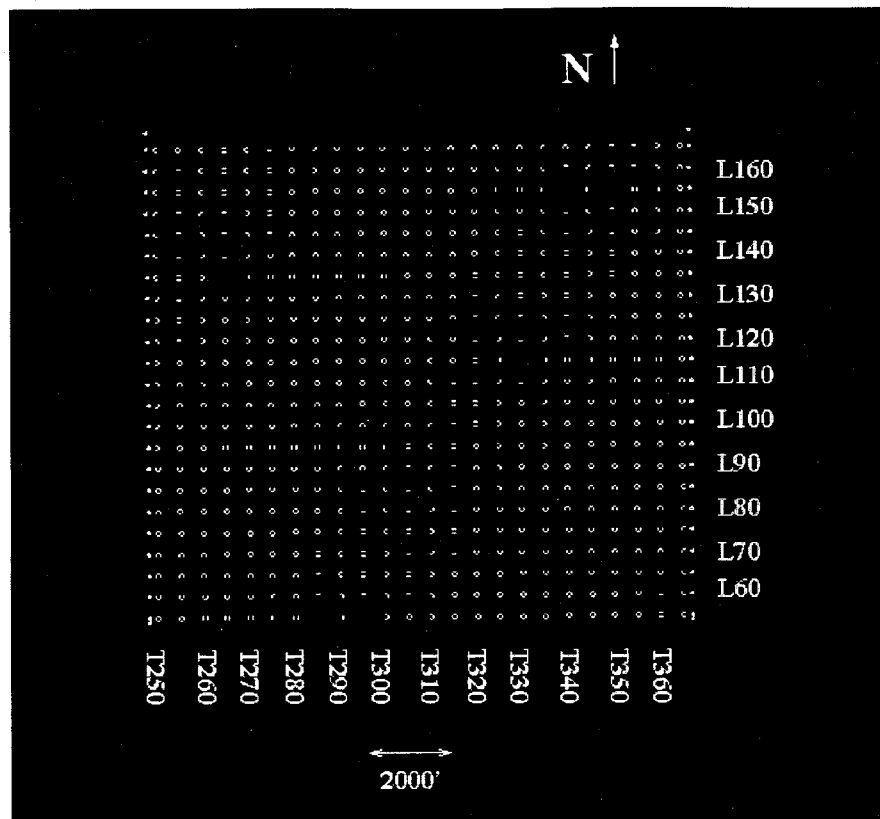
Figure 4.10: Reference map for well and seismic transect locations. The vertical axis gives the inline number, and the horizontal axis gives the trace or crossline number.

San Andres Formation: Occurring between 610 ms and 710 ms, this pick is a very high amplitude, continuous peak. It is underlain by a low frequency trough with variable amplitude.

Delaware Mountain Group: This horizon ranges from 650 ms to 760 ms and consists of a segmented, variable amplitude, moderate to high frequency trough.

First Bone Spring Carbonate: This pick occurs between 755 ms and 950 ms and is a generally high amplitude, undulating, discontinuous peak. A distinctive, irregularly shaped, low frequency trough with variable amplitude occurs directly below the First Bone Spring

Carbonate peak. This was used as a guide when the peak became difficult to follow due to noise, artifacts, faulting, or lithologic variability.

First Bone Spring Sand: This horizon occurs between 940 ms and 1070 ms and is a moderate amplitude, moderate to low frequency, fairly continuous trough overlain by a discontinuous, irregularly shaped peak.

Second Bone Spring Carbonate: Ranging from 760 ms to 1110 ms, this pick is a high amplitude, medium frequency, fairly continuous peak. The reflections within the overlying First Bone Spring Sand onlap the second carbonate along the upper slope.

Second Bone Spring Sand: This pick ranges from 940 ms down to 1140 ms and is a high frequency, moderate amplitude trough. In the northern half of the study area, this trough is relatively continuous. To the south, it becomes discontinuous and generally has lower amplitude. It was identified in the southern half of the survey area by its relationship with the underlying units (internal reflections within the Second Sand). The top of the Second Sand is interpreted as being the upper boundary to a wedge of prograding clinoforms.

Top "C" Sand (pay zone within Second Sand): Occurring between 1050 ms and 1180 ms, this horizon is a fairly continuous, moderate amplitude trough whose frequency increases to the south. It is conformable with the underlying peak, and it is downlapped by the reflections above it.

Base "C" Sand: This pick ranges from 1080 ms down to 1190 ms and consists of a fairly continuous, somewhat undulating, moderate to low amplitude peak with variable, but generally high, frequency. It lies above a series of overlapping "shingles" in the central portion of the survey area.

Third Bone Spring Carbonate: This horizon extends from 1055 ms down to 1220 ms and is a fairly low frequency, high amplitude peak. In the central portion of the study area (inlines 275 to 330), it is a continuous reflection that is conformable with the underlying low

frequency trough and downlapped by the overlying reflections. In the remainder of the study

area, it becomes more discontinuous (in a few areas it changes to high amplitude trough).

Third Bone Spring Sand: Ranging from 1070 ms down to 1235 ms, this pick is a moderate

amplitude trough with variable, but usually low, frequency. Localized discontinuities

become more abundant on the east and west edges of the survey.

Strawn Formation: Found between 1324 ms and 1505 ms, this horizon is a moderate

amplitude, medium frequency, continuous peak conformable with the underlying trough

which has similar reflection strength and frequency. It is overlain by a very irregularly

shaped, low amplitude trough.

4.1.3 Basement structure

For this study, the term 'basement' is being used loosely to refer to units at and below the

Strawn level. The basement structure controls the physiography of the shelf margin over

which the Wolfcamp and Bone Spring slope deposits prograded, and the Strawn Formation

was chosen to illustrate this structure because it produces a high amplitude reflection that is

easy to track through the seismic data. The relevance of these structures to the deposition of

the Second Sand will be addressed in Section 4.2.

The time-structure map of the Pennsylvanian Strawn Formation shows the main

structural elements present at this level (Figure 4.11). A prominent ridge trends N-S along

the eastern border of the survey area. This ridge is an upthrown fault block bounded by a

series of north-south trending reverse faults. The N-S trending reverse fault that bounds the

western side of this ridge dies off with depth and is not visible beyond approximately 100ms

below the Strawn (Figure 4.12). In contrast, the fault bounding the eastern margin of the

ridge extends to significantly greater depths, is steeper, and has substantially more offset. In

a first octave filtered version of the data set, this appears to be a single, high angle fault

(Figure 4.12) that can be followed to great depth until it becomes lost in noise below 1950ms. In the unfiltered data, it seems that this fault is actually made up of a series of small, more shallowly dipping reverse faults that would be more accurately characterized as a fault zone rather than a single fault (Figure 4.12). West of this ridge, a gently downwarped flexure covers the central section. Small reverse faults within this central flexure form subtle horsts that interrupt the smoothness of the topography, but do not result in significant relief (Figure 4.13). This flexure is bounded on the west by another N-S trending, fault-bounded ridge. The two reverse faults bounding this ridge have angles greater than those seen in the small reverse faults bounding the eastern ridge (accounting for the greater prominence of this ridge in the northern half of the survey area). These faults appear to have largely died out to the south by inline 90. To the north, the central flexure intersects the upper slope. Along this juncture, small E-W trending faults occur between the N-S faults forming an inverted "U" clearly visible in time slices through a continuity cube generated from the seismic data (see Figure 4.14).
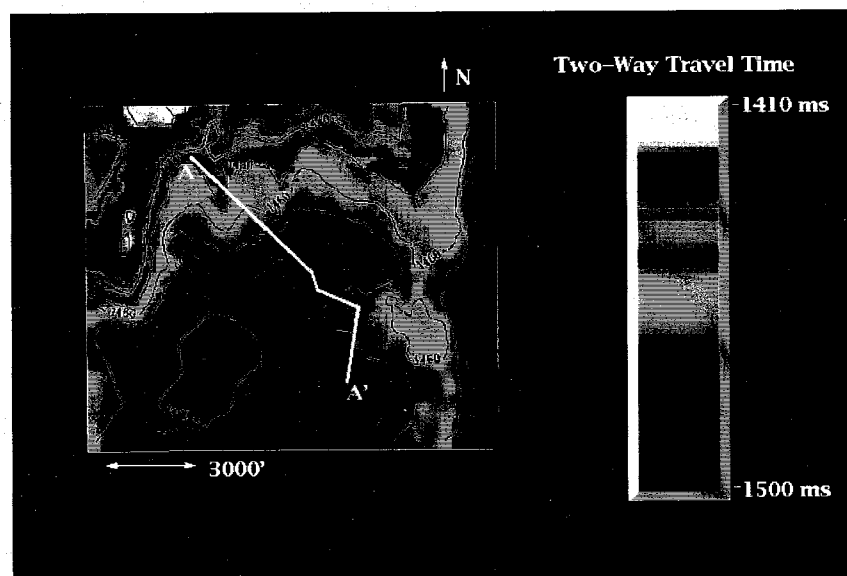
Figure 4.11: Time-structure map of the Strawn Formation. The main structural elements are two N-S trending, fault-bounded ridges joining a gently downwarped central flexure.
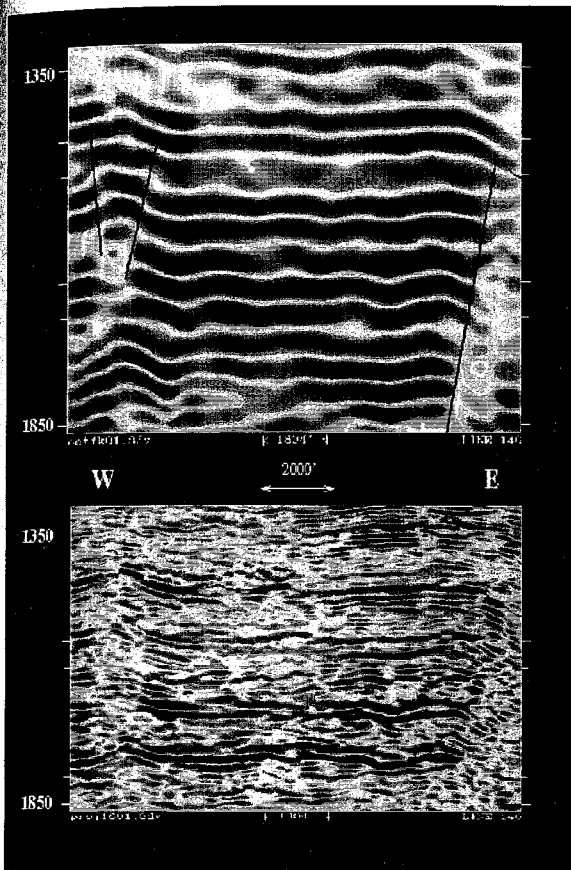
Figure 4.12: E-W seismic transect showing reverse faults (red lines) bounding the N-S trending ridges at the Strawn level (red horizon) in the 1st octave filtered version of the data (upper) and in the original data (lower). The faults bounding the western ridge die off more rapidly with depth than those bounding the eastern ridge.
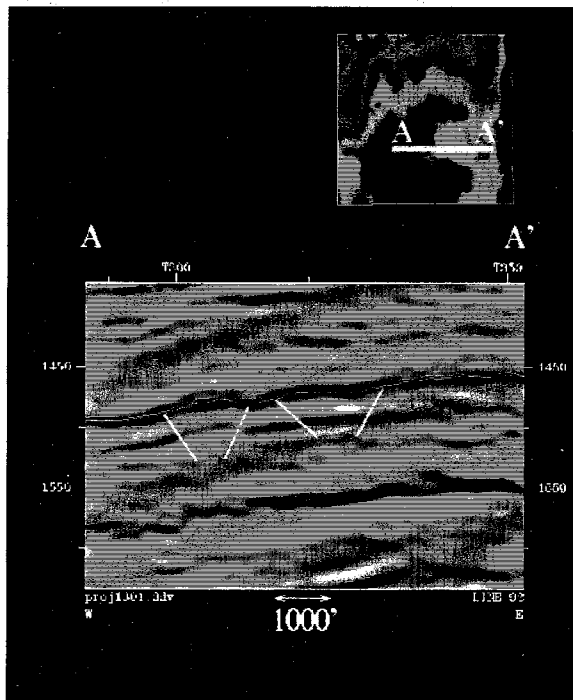
Figure 4.13: E-W seismic transect showing horsts (faults indicated in yellow) within the central flexure at the Strawn level (red horizon). The location of the cross-section in shown in the map view of the Strawn Formation at the top of the figure.
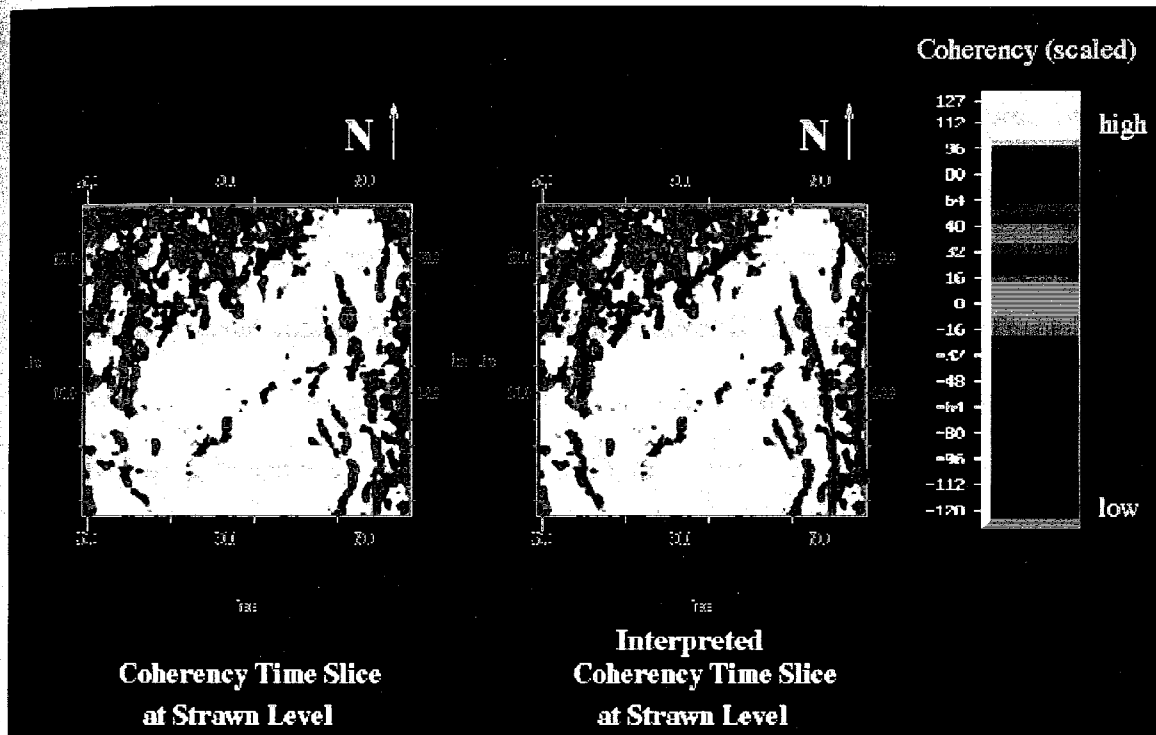
Figure 4.14: Time slice through the coherency/continuity cube at the Strawn level (left) and faults interpreted from this slice (blue lines on right). Faults appear as regions of low continuity (red, blue, and green).

4.1.4 Horizon time-structure maps

By the onset of Second Sand deposition the relief present at the Strawn level had been modified by the deposition of later sediments, but the overall pattern imposed by the underlying structure is still evident. A time-structure map of the base of the Second Sand (top of the Third Carbonate) shows a regional slope to the south, an E-W depositional strike, and two N-S trending ridges joined by a central flexure (Figure 4.15). The relief of the western ridge has been reduced while the eastern ridge is still a prominent feature. The total relief from the uppermost slope to the deepest portion of the sub-basin has actually been increased from the 90 ms seen at the Strawn level to 160 ms at the Third Carbonate level. The most noticeable change at the Third Carbonate level is the increased prominence of the re-entrant in the upper slope in the center of the area. Although this re-entrant appears channel-shaped (concave up) in cross-section (Figure 4.16), there is no clear evidence in the seismic data to indicate that this is an erosional feature. It is possible that it was scoured out by erosive density currents, but the truncated beds that would provide evidence of this may
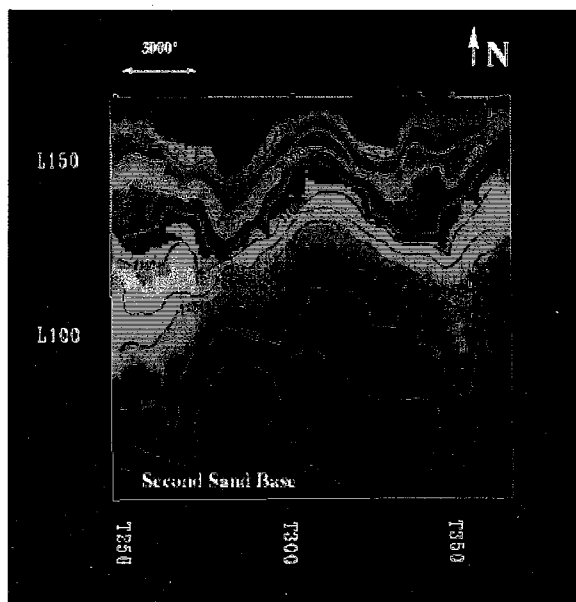
Figure 4.15: Time-structure map of the base of the Second Sand. Note the continued presence of the N-S trending ridges and the increased prominence of the large re-entrant in the upper slope. The contour lines are two-way travel time in ms.

simply below the seismic resolution. A time-structure map of the top of the Second Sand (Figure 4.17) shows that the reentrant continued to be a prominent feature throughout the time of Second Sand deposition. It is also apparent from this map that the deposition of the Second Sand resulted in the near-complete filling of the central flexure. This is confirmed by examining an isochron map of the Second Sand (Figure 4.18). This map shows a striking similarity to the time-structure map of the Strawn. The thickest regions of the Second Sand roughly conform to the shape of the deepest part of the sub-basin most visible at the Strawn level (compare Figures 4.11 and 4.18). The Second Sand thins upslope and to the east and west over the ridges.
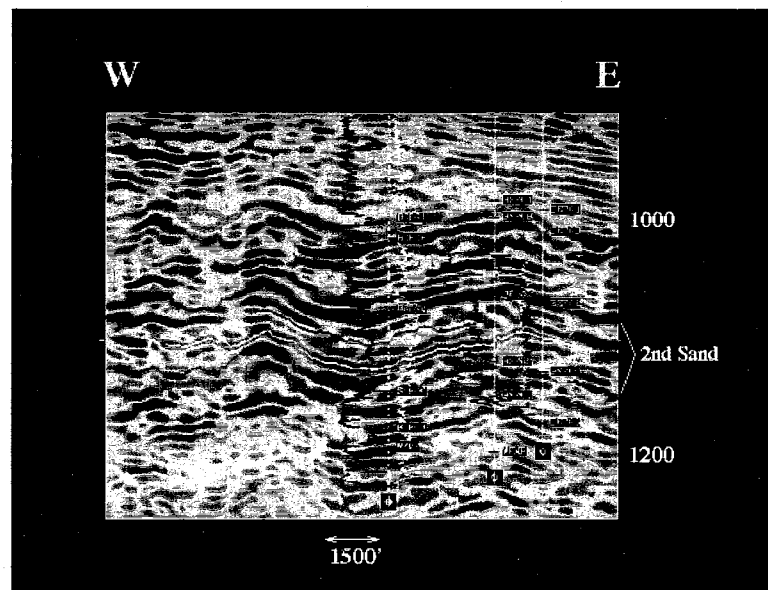
Figure 4.16: E-W seismic transect through the Second Sand through the center of the study area. Note the "channel-shaped" cross-section of the fan. Well logs are superimposed on the seismic data in green (gamma ray log) and white (sonic log). The vertical axis is two-way travel time in ms.

Figure 4.17: Time-structure map of the top of the Second Sand. Note the continued prominence of the central re-entrant in the upper slope.
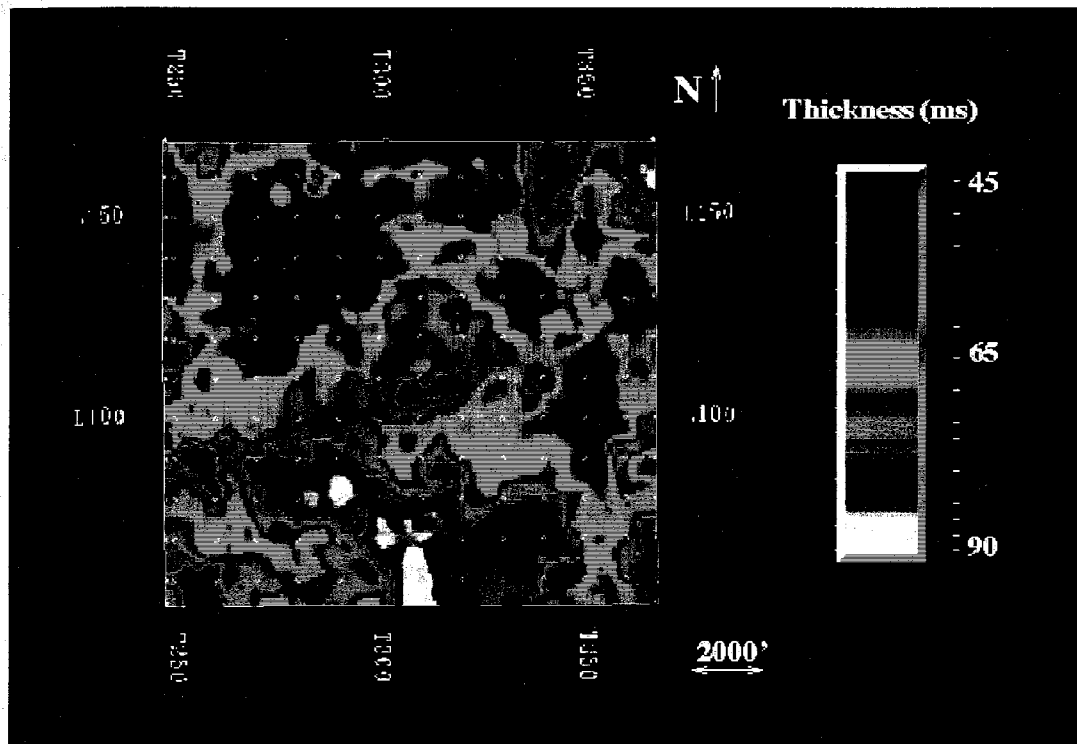
Figure 4.18: Isochron map of the Second Sand. Deposition of the Second Sand resulted in near complete filling of the sub-basin.

4.1.5 Internal reflection configuration and log character of the Second Sand

Based on the internal reflection configuration and seismic character, the Second Sand can be subdivided into three units: the early, middle, and late periods (Figure 4.19 and 4.20). On well logs, these intervals correspond respectively to (1) the zone beneath the "C" Sand (henceforth called the "D" zone), (2) the "C" sand, and (3) the pelagic sediments and the "A" and "B" sands that overlie the "C" sand (Figure 4.21).

Reflection Configuration, Early Period: The first phase of Second Sand deposition consists of a package of clinoforms that downlap the underlying Third Carbonate reflection. In a NW-SE cross section (Figure 4.19) through the Second Sand, these clinoforms can be seen prograding to the southeast. Small troughs occur where the adjacent shingles meet (see features marked with a "T" in Figure 4.19). Time-structure maps of each of the shingles shows that they are fan- to lobate-shaped features that pinch out at the base of the upper slope. The entire package is confined to the central flexure and eastern ridge (Figure 4.22). The first or westernmost of these shingles is aligned roughly N-S and is very narrow (Figure 4.23). The apex is directly north of a prominent re-entrant in the upper slope. The second shingle (Figure 4.24) is more areally restricted, elongated in the E-W direction, and overlaps the eastern edge of the first shingle. A prominent apex to this lobe cannot be seen in the seismic data. At its upslope termination, the reflection rapidly loses its amplitude standout and is no longer detectable within the space of 5 E-W survey lines (a lateral distance of 550' in the N-S direction) with little decrease in the E-W length of the reflection. In some areas these two shingles appear to merge and can only be separated by subtle differences in seismic character (Figure 4.25).

Although these lobes could be alternatively interpreted as a single, locally discontinuous reflection, the choice made here to separate them into two distinct reflection events is believed to be justified because: 1) On NW-SW transects, particularly those that cut through the upper portion of lobe 1 and the middle region of lobe 2 (Figure 4.19), there is clear separation between these events; 2) The seismic character of the shingles differs (in particular the wavelet asymmetry and amplitude, see Figure 4.25); and 3) the geometry of a composite horizon of lobes 1 and 2 appears geologically unreasonable. There is no topographic obstruction present east of lobe 1 that would adequately account for the sudden termination of lobe 2 at inline 100 if these were actually one event. Given these arguments, interpreting these as two separate reflection events seems the most logical choice. The viability of this interpretation was tested by creating a simple 2-D geologic model with the geometry of the shingles based on the seismic data and physical properties obtained from well logs. A pseudo 2-D seismic survey "shot" over this model showed similarity to the actual seismic data indicating that this model is a geologically and geophysically plausible, though not necessarily unique, interpretation.

The third or easternmost shingle is still within the central flexure, but it extends further east, draping the eastern ridge, and also to the south to an unknown distance outside the study area (Figure 4.26). The apex of this shingle is east of the central re-entrant in the upper slope. It is located below a small re-entrant in the upper slope just west of the eastern ridge.
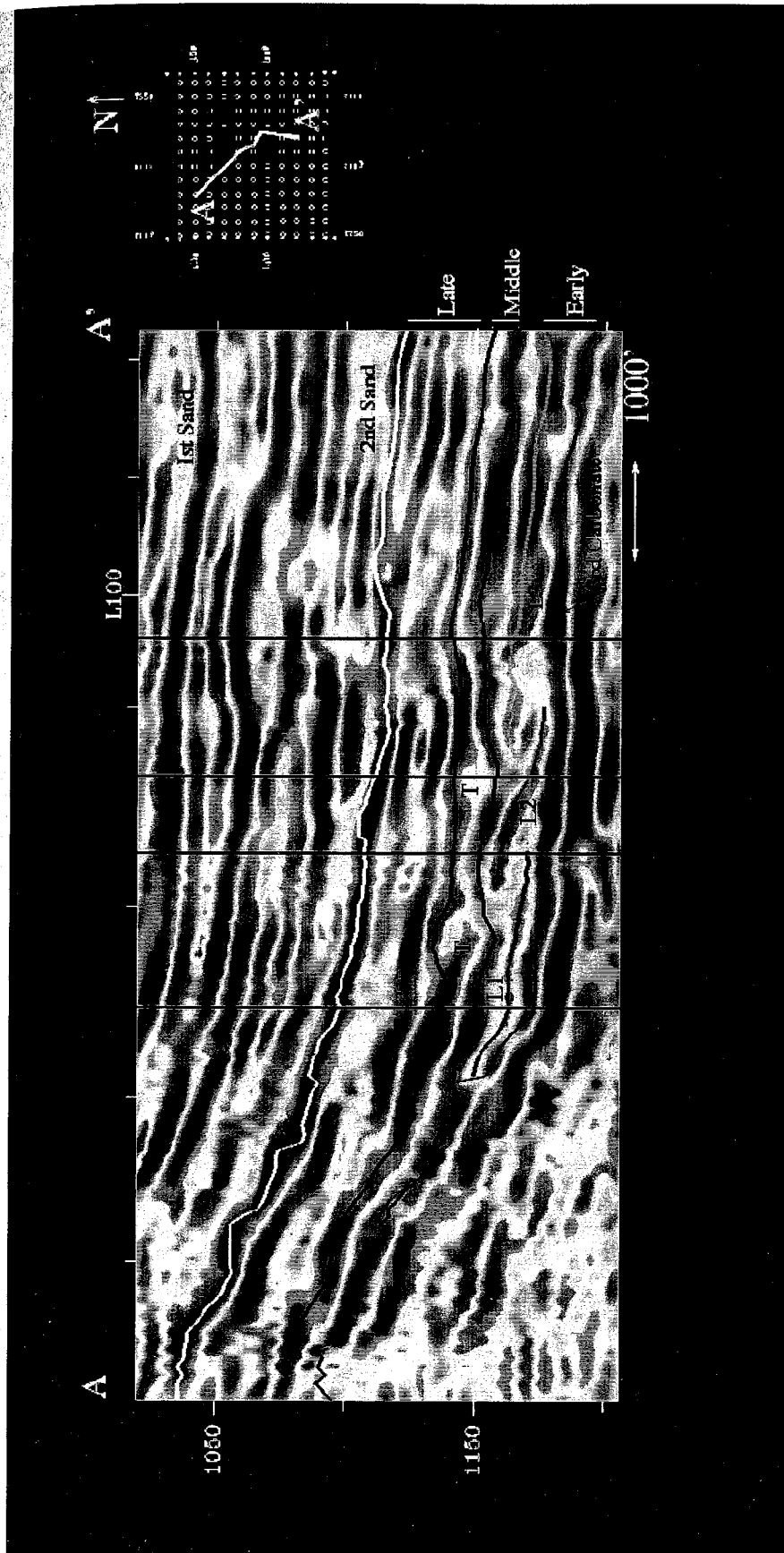
Figure 4.19: NW-SE cross-section (location given in indicator map in upper right) showing the early, middle, and late periods in the depositional history of the Second Sand. L1-L3, the lobes of the early period, overlie the sequence boundary (top of the Third Carbonate). The middle period, the "C" sand, is marked by the black horizons. Note thickening of "C" sand above the paleobathymetric lows (marked by "T"'s) formed where adjacent lobes overlap. The late period consists of the prograding wedge of reflections between the top of the "C" sand and the top of the Second Sand. The vertical axis is two-way travel time in ms.
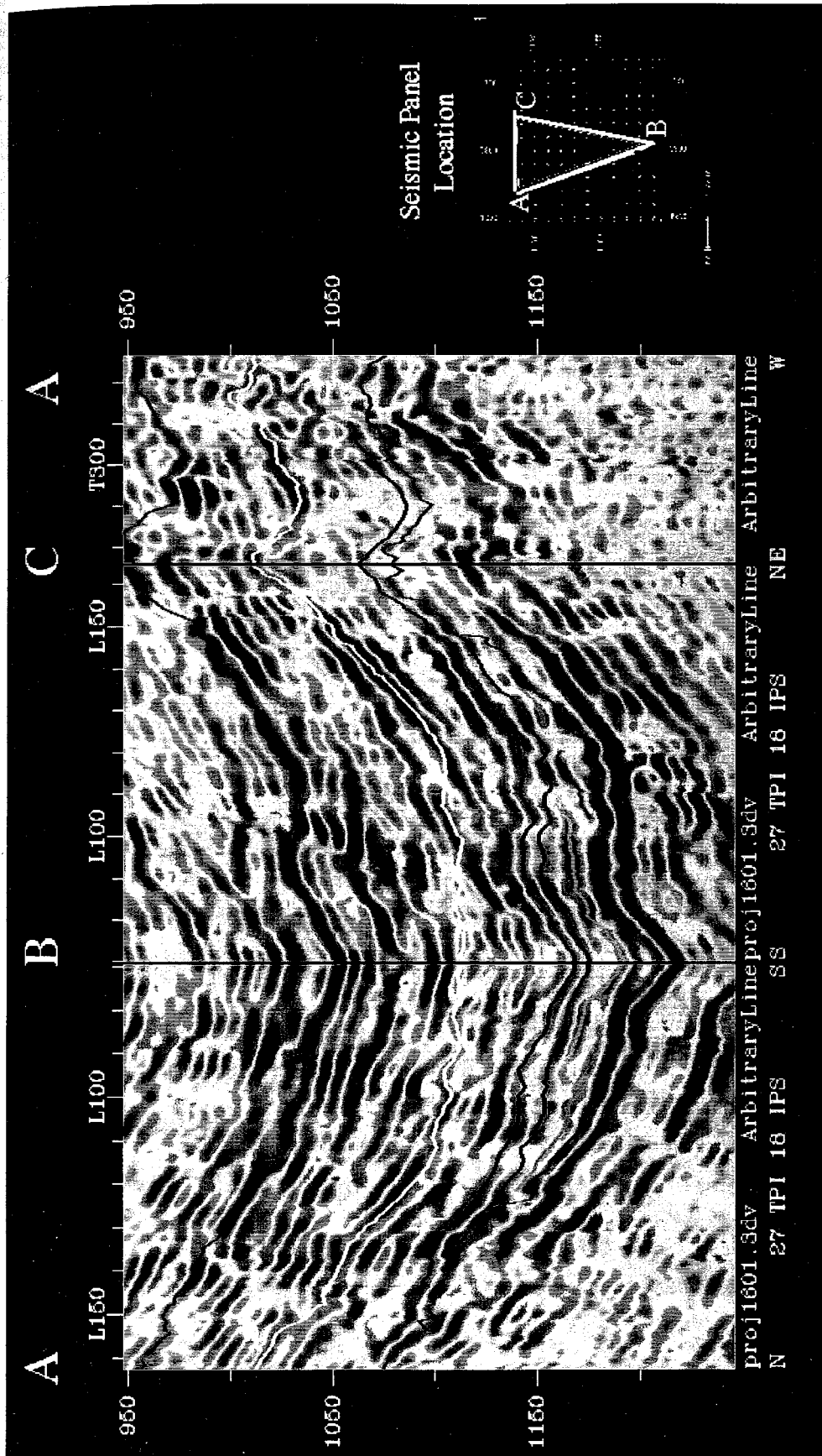
igure 4.20: A fence diagram through the seismic data showing a different perspective of the three periods in Second Sand deposition. The location of the fence diagram s given on the right. The location of the fence diagram is again shown in black; and he top of the Second Sand is outlined in yellow.
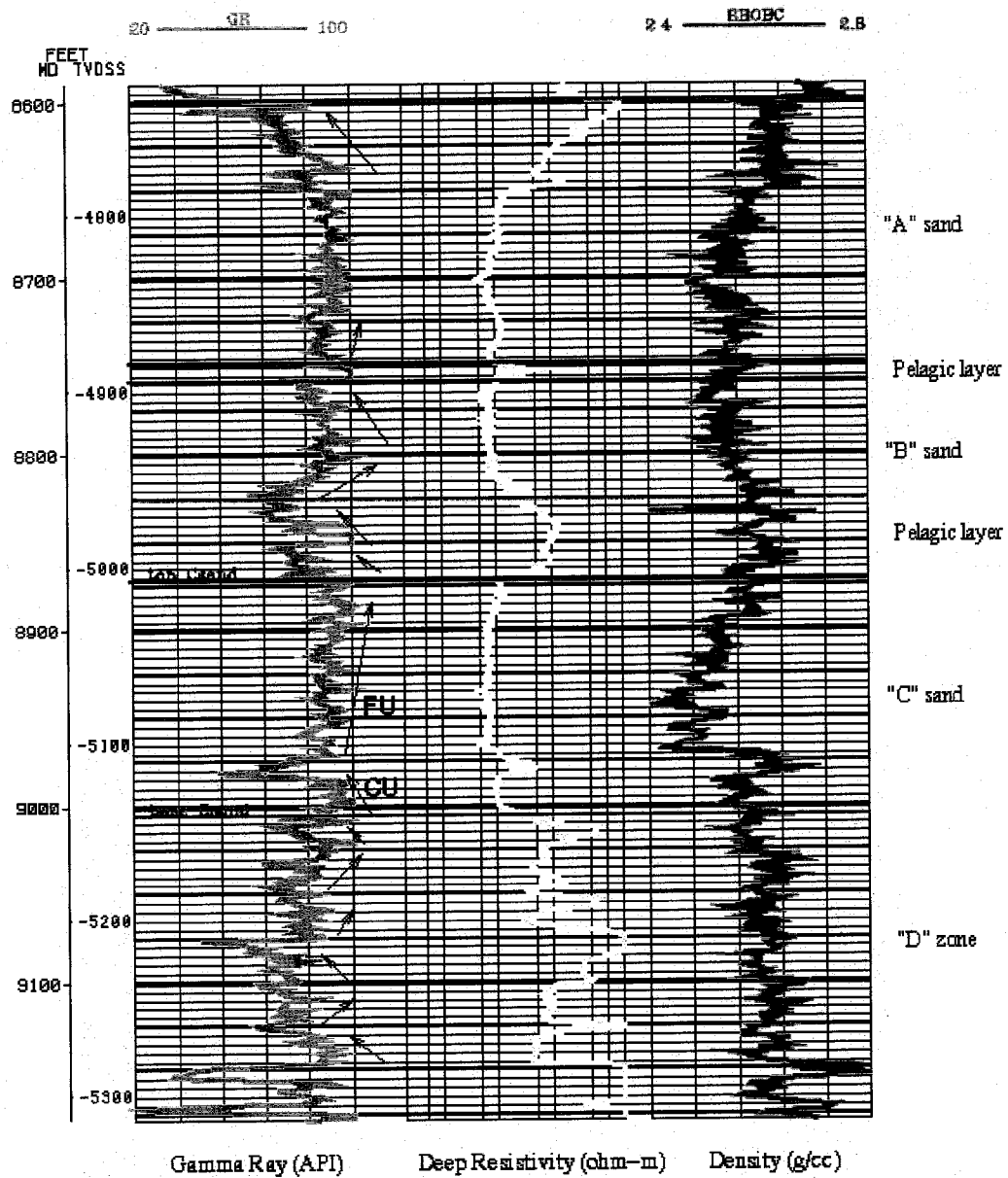
Figure 4.21: Type log for the Second Sand along the upper and middle slope. Coarsening up (CU) and fining up trends (FU) in the gamma ray logs are indicated by arrows. See text for discussion of log character.
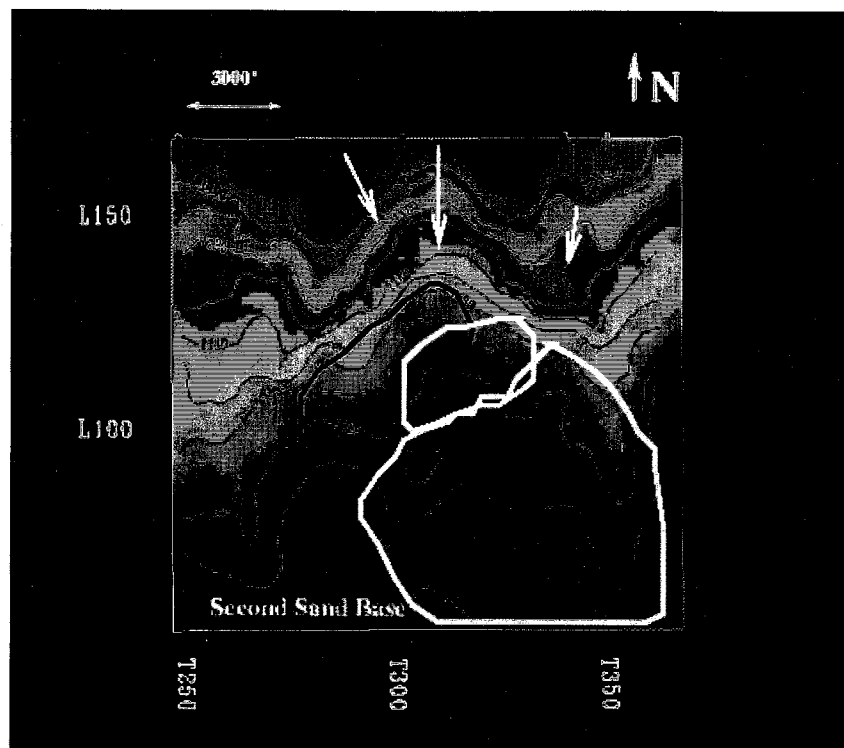
Figure 4.22: Distribution of the three lobes of the early period. The red, white, and yellow outlined lobes correspond to L1, L2, and L3, respectively, of Figure 4.18. Arrows indicate possible sediment transport directions. The underlying colored time-structure map shows the paleotopography during the early period (base of the Second Sand time-structure map).
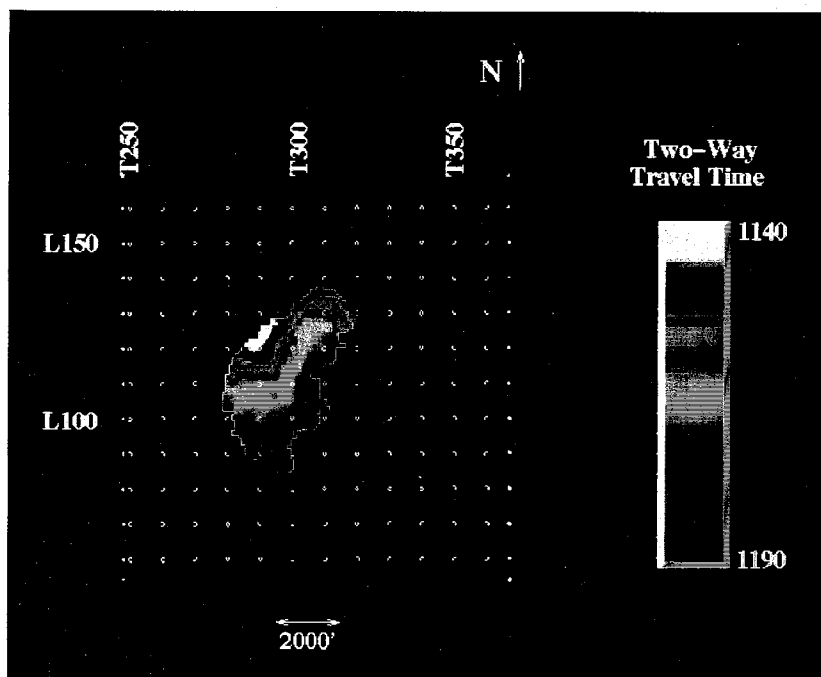
Figure 4.23: Time-structure map of lobe 1 of the early period. Note the N-S elongation and the concave upward western margin in the northern portion of the lobe.
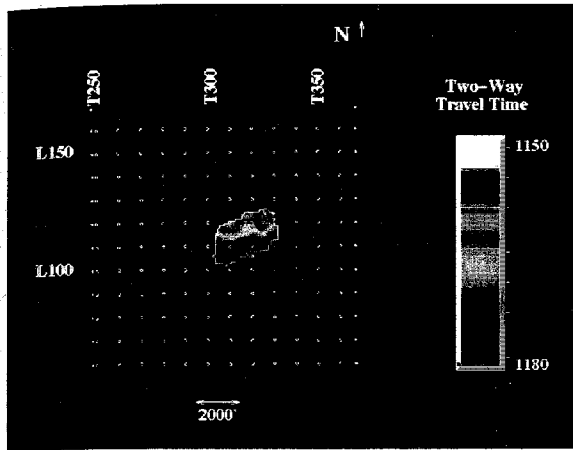
Figure 4.24: Time-structure map of lobe 2 of the early period.
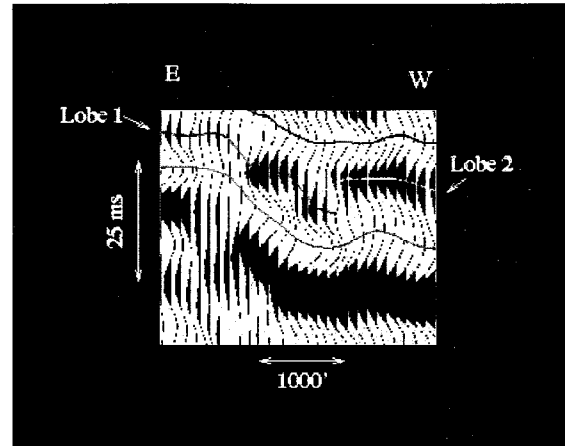
Figure 4.25: Close up view of a wiggle trace display showing the overlap zone between lobes 1 and 2. Note the greater asymmetry of lobe 1's trough. The green horizon is the base of the Second Sand, and the black is the base of the "C" sand.
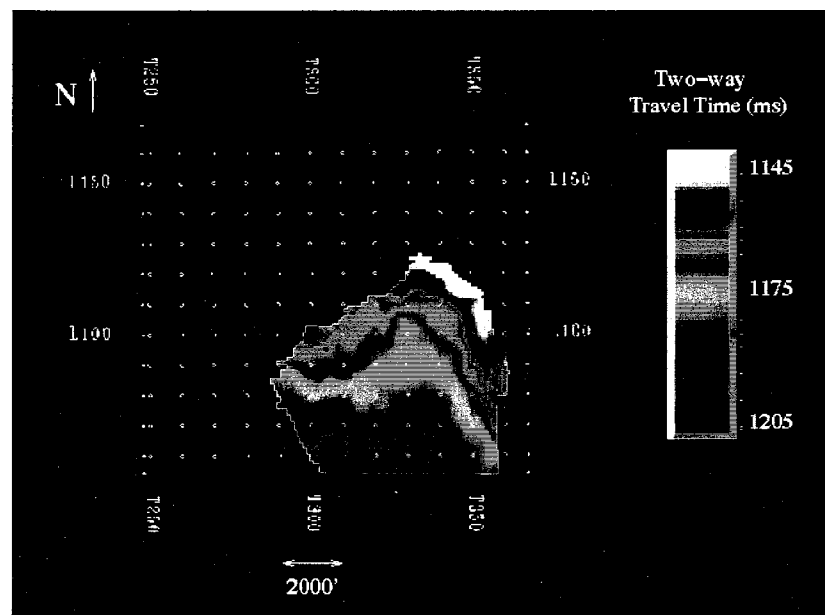
Figure 4.26: Time-structure map of lobe 3 of the early period. Note the more easterly location of this lobe, the well defined fan shape, and the pinch out to the east.

Log Character, Early Period: The early period identified in the seismic data corresponds on well logs to the poor reservoir quality "D" zone and the overlying pelagic layer that separates it from the "C" sand. The log character of the "D" zone is best illustrated on deep resistivity and gamma ray curves (Figure 4.21). From these it appears that the interval consists of interbedded porous and nonporous zones with highly variable bed thicknesses ranging from 10' to 50'. Where photoelectric factor logs are available, the average values for this zone range from 2.5 to 3.0 barns/electron which are within the range of dolomitic siltstones or silty dolostones. For comparison, pure quartz has a photoelectric index of 1.81, and pure dolomite has a value of 3.14 barns/electron. The "D" zone gamma ray logs are typically serrate, and the trends (i.e. coarsening up or fining up sequences) vary with location or are simply not present. Where trends are visible, the interval appears to consist of a series of alternating fining up and coarsening up sequences. The total number of sequences and the relationship between the coarsening up and fining up trends varies with location (Figure 4.27). Density curves through this interval are also serrate, but fairly constant, with average values of approximately 2.6 g/cc (for comparison, dolomite ranges from 2.4 g/cc to 2.8 g/cc), higher than any other interval within the Second Sand. Due to the wide spacing between wells logged in this interval, it is not possible to track individual units from well to well within this zone.

The pelagic layer separating the "D" and "C" is continuous throughout the area and is approximately 25' thick. The top of the pelagic layer is marked by an abrupt increase in resistivity, a decrease in porosity, and slightly lower gamma ray counts than the overlying "C" sand. Photoelectric indices show that the composition of this layer is intermediate between quartz and dolomite.
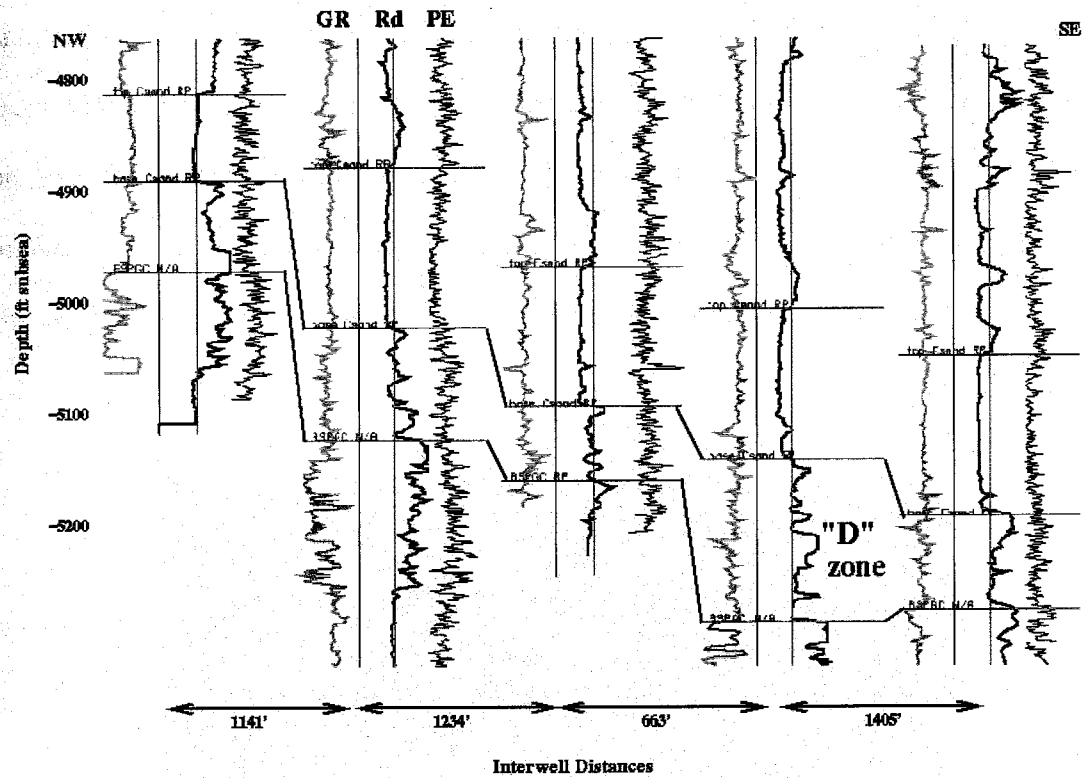
Figure 4.27: NW-SE structural log cross-section showing the variability of the "D" zone across the study area. Each log suite contains a gamma ray log (green,GR), a deep resistivity log (heavy black, Rd), and a photoelectric factor log (thin black, PE). All curves increase to the right.

Reflection Configuration, Middle Period: The middle period consists of a trough and peak that onlap the upper slope and define the top and base of the "C" sand (Figure 4.19). In plan view, each of these reflections has a broad fan shape that narrows to the north and pinches out high on the upper slope. The apex of each of these units is located in or near the central re-entrant in the upper slope. As can be seen in Figures 4.28 and 4.29, these units thin over the N-S ridges, ultimately pinching out over the ridges in the northern portion of the study area and extend to an unknown distance beyond the southern boundary of the survey area. Because the reflections terminate outside the area, it is impossible to tell if these reflections prograde (i.e. downlap onto the underlying reflection) as did those in the early period. As the reflections widen to the south, they appear to be more passively draped over structural highs. An isochron map of this interval shows that the "C" sand thins over the N-S ridges and
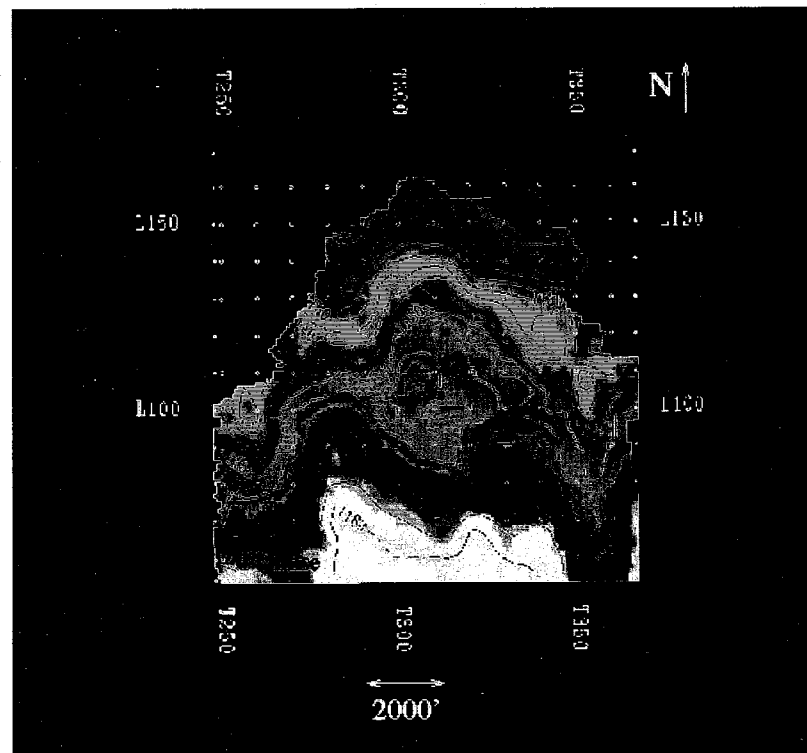
Figure 4.28: Time-structure map of the base of the "C" sand. Contour lines are two-way travel time (ms).

57

reaches a maximum thickness in the center of the survey area (Figure 4.30). The thickest regions occur in elongate zones that trend N-S to NE-SW.

Core Study Results and Log Character, Middle Period: As previously mentioned, the "C" sand has been cored and is believed to consist of channel, laminated levee/overbank, and levee/overbank slump facies. It is overlain and underlain by a pelagic facies (Figure 4.31 and 4.32). In the present study, the base of the "C" sand is at the top of the underlying pelagic layer, and the top of the "C" sand is placed at the base of the overlying pelagic facies.
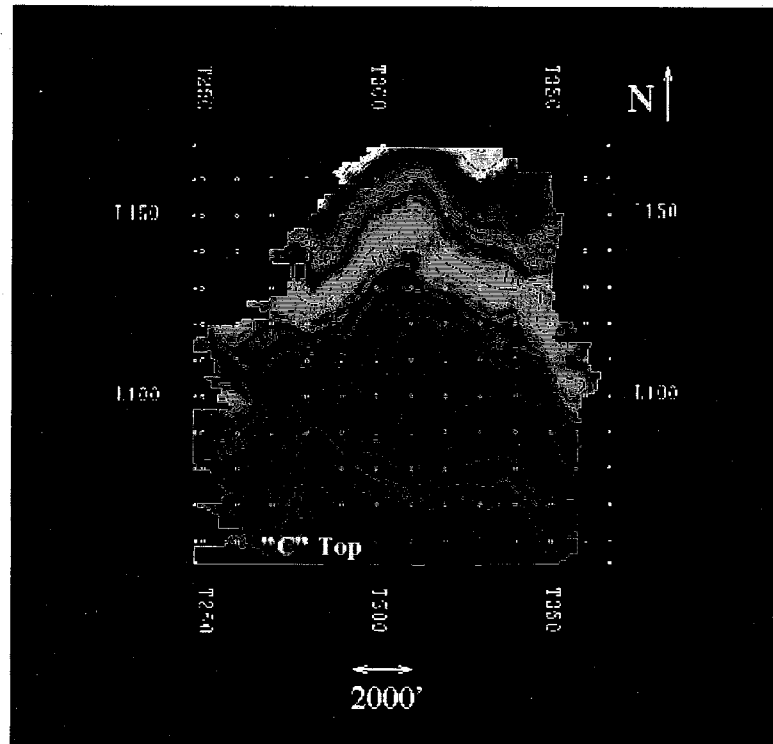
Figure 4.29: Time-structure map of the top of the "C" sand. Contour lines are two-way travel time (ms).
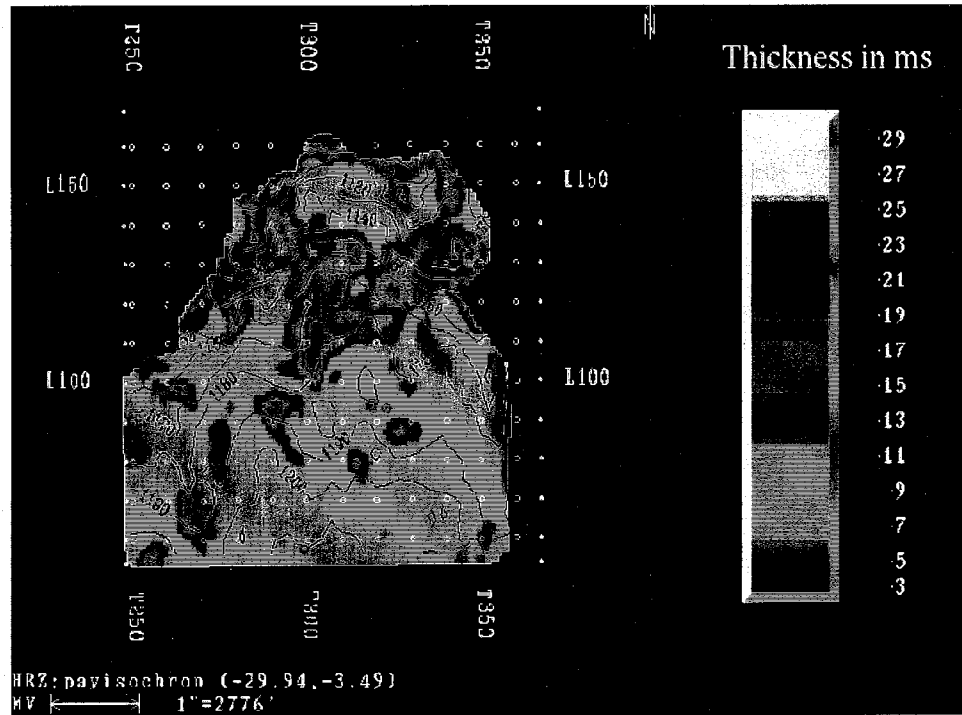
Figure 4.30: Isochron map of the "C" sand (thickness reported in ms). Sediment thicks are located below the central re-entrant in the upper slope and trend N-S to NE-SW.

**Rippled Crossbedded   Laminated Levee/Overbank Facies   Pelagic Facies
Channel Facies**
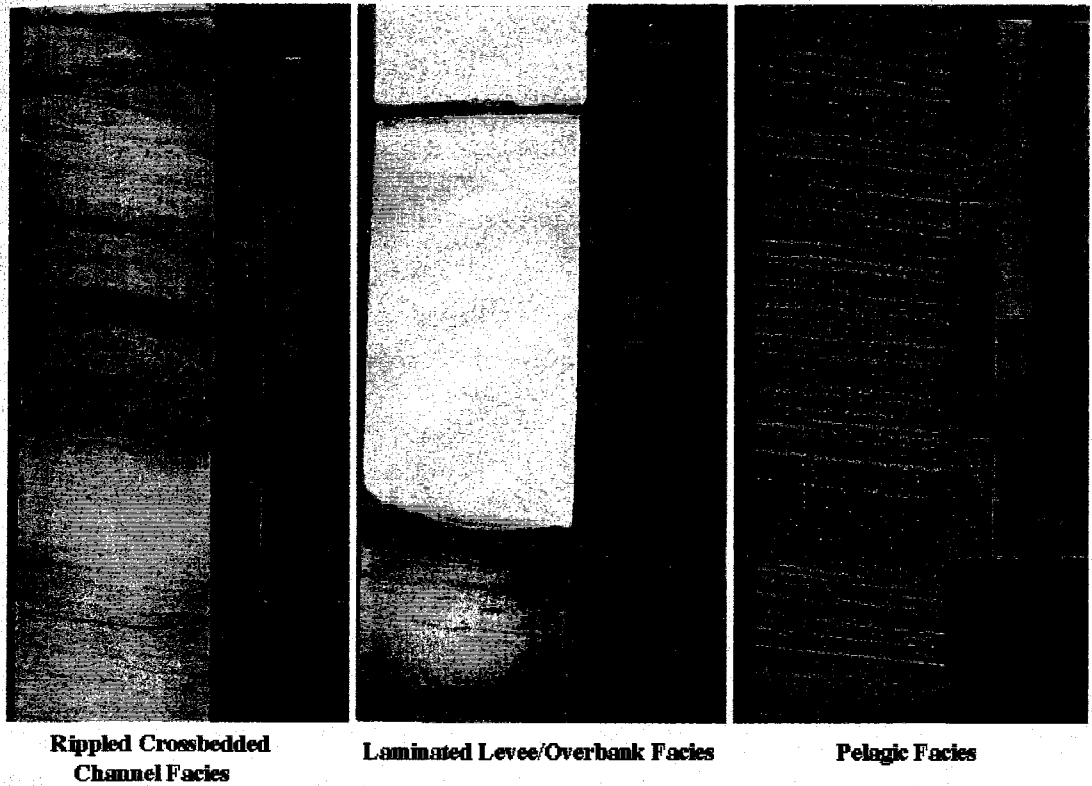
Figure 4.31: Core photographs taken under UV light of the different facies identified within the "C" sand (adapted from Messa *et al.*, 1996)
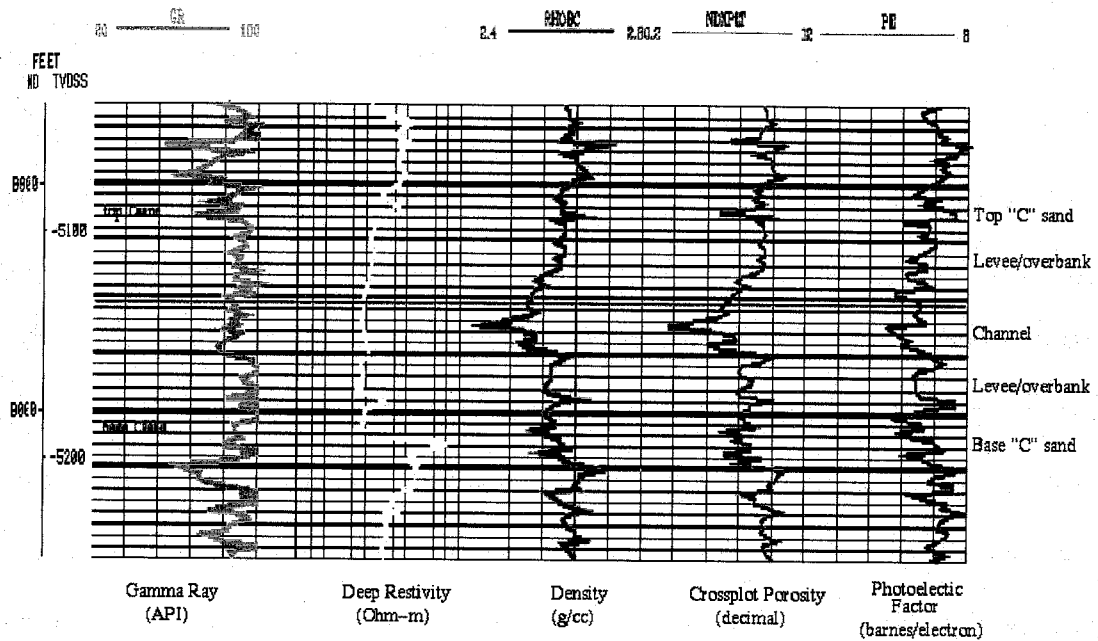
Figure 4.32: Type log for the "C" sand within the study area. The channel facies is most visible on the density and crossplot porosity logs. See text for full discussion of the log character of the "C" sand.

The channel facies consists of well-sorted, coarse siltstone to very fine-grained sandstone with scour marks, current ripples, planar tabular crossbedding, and flame structures (Messa *et al.*, 1996). Messa *et al.* (1996) have interpreted these deposits as turbidites (the B and C units of the Bouma sequence). The laminated levee/overbank facies is made up of normally graded, fine to coarse siltstone with minor amounts of very fine sand (Messa *et al.*, 1996). Sedimentary structures include thin, inclined parallel laminations and abundant fluid escape structures. These are believed to be thin-bedded turbidites lacking the A unit of the Bouma sequence (Messa *et al.*, 1996). The levee/overbank slump facies is lithologically identical to the laminated levee/overbank facies, but differs in that slumping has resulted in a reduction in porosity along slump scars, convoluted bedding, and shearing (Messa *et al.*, 1996). The "C" sand is overlain and underlain by a pelagic facies consisting of "very finely laminated, pyritic, argillaceous, dolomitic siltstone" and "dark, thinly bedded calcareous siltstones"

61

(Messa *et al.*, 1996). The pelagic facies has very low porosity and permeability and acts as a seal for the reservoir (Messa *et al.*, 1996).

Using the well data alone, the laminated levee/overbank and levee/overbank slump facies identified in cores cannot be separated, and the channel facies can only be identified as a high porosity zone on crossplot porosity curves (Figure 4.32). As a whole, the "C" sand is marked by a change to low deep resistivity values and a blocky resistivity curve with moderate separation between deep and shallow curves (indicating infiltration of a permeable zone). The density log is quite variable depending on location, but overall it has a bell shape (decreasing density with depth) with the lowest densities of 2.4 g/cc occurring slightly above the base of the "C" sand (within the higher porosity channel facies). Within both the channel and levee/overbank facies, the gamma ray log is serrate, and average values vary from mid-seventies to low nineties (in API units). The gamma ray log shows a thin basal coarsening up sequence overlain by a weak fining upward trend in some areas. Unfortunately, there are no true shales within the area to use as a base line, so the shale fraction cannot be quantified. Above and below the "C" sand, the resistivity and density increase abruptly and the porosity and gamma ray counts generally decrease as the pelagic facies is encountered.

The facies identified in cores appear to be beyond the resolution of the seismic due possibly to a combination of the small or gradual acoustic impedance contrasts associated with the facies changes, and the relative thinness of the individual units with respect to the frequency content of the seismic data. The results of simple geologic and seismic modeling that incorporates the facies framework determined by core and log studies (performed by the Harvey E. Yates Company) are strongly dependent on the wavelet used in the modeling process. With a Ricker wavelet (a somewhat idealized wavelet because it is of very short duration), some of the facies can be resolved, although there is some interference between reflections as the facies thin or pinch out. To obtain a more realistic wavelet, a zero-phase

band pass filter (an inverse filter that produces a zero-phase wavelet with a user-specified frequency content) with roughly the same frequency content as the seismic data was used to create a second model. In this model, internal reflections produced by the pelagic, overbank/levee, and channel facies were difficult to separate from the reflections produced by the top and base of the unit. Due to software limitations, it was not possible to create a model that used the actual seismic wavelet extracted from the data. However, the synthetic seismograms created during the well tying process using wavelets extracted from the data are essentially 1-D models themselves. These indicate that at least at the well locations with synthetic seismograms, the individual facies are not resolvable. The reflection picked as the top of the C sand appears in most areas to correspond to a composite reflection produced by the acoustic impedance contrasts between the "B" sand and pelagic layer and the lower velocity and density channel / levee-overbank complex of the "C" sand. The reflection picked as the base of the "C" sand is produced by the acoustic impedance contrast between the "C" sand base and the underlying "D" sand or the third carbonate depending on the thickness of the "D" sand. In the seismic data these picks are complicated by variations in phase of the top and base of the "C" sand.

Reflection Configuration, Late Period: Similar to the early period, the last phase of deposition of the Second Sand is characterized in the seismic data by a series of prograding reflections that are represented in cross-section by a series of clinoforms that downlap onto the top reflection of the middle period (Figure 4.19 and 4.20). The seismic character of the final period differs from that of the early period in that individual reflections tend to be more discontinuous and occasionally somewhat chaotic in nature, giving the top of the Second Sand a slightly hummocky appearance in the southern quarter of the study area. In addition, the reflections in the upper portion of the late period lack the distinctive fan shapes of the

earlier shingles, and the progradation is to the south rather than the southeast. The lowermost reflections are the most laterally extensive, covering the upper slope down to the southern boundary of the survey area. Each of the overlying reflections covers an increasingly smaller portion of the upper slope. By the end of the late period, reflections begin along the lower slope (line 90) and extend south beyond the boundary of the study area. As a whole, this package of reflections covers the entire study area and is the thickest, both in two-way travel time and depth, of the three periods within the Second Sand.

Log Character, Late Period: The late period corresponds to the "A" and "B" sands identified on well logs and the pelagic layer separating the "C" sand from the "B" sand. With the exception of one or two wells, the "A" and "B" sands are not economically viable reservoirs in this oil and gas field. No cores have been taken, and, as a result, the log can not be calibrated with core data to provide a facies framework to characterize these sands. However, it is assumed (based on the similarity of the depositional settings and the log responses) that the "A" and "B" sands contain facies similar to those seen in the "C" sand. The log signatures of the "A" and "B" do differ within the study area, and therefore will be discussed separately below.

"B" Sand Log Character: Along the upper and middle slope, the "B" sand can be identified by (1) a blocky, cylindrical resistivity log pattern, (2) a slight increase in density with depth, and (3) a serrate gamma ray log with a basal fining up sequence overlain by a weak coarsening up sequence (Figure 4.21). The gamma ray log is serrate but still relatively uniform throughout the majority of the "B" sand in the upper and middle slope areas. In contrast, to the south along the lower slope the gamma ray log exhibits increasing variability, and the "B" sand contains a greater proportion of alternating layers of high and low gamma ray counts (Figure 4.33). A corresponding pattern is not seen in the resistivity logs which

still retain their blocky shape. Along the upper and middle slope, the "A" and "B" sands are separated by a relatively thin (generally less than 35') layer with high resistivity values and moderate to high gamma ray counts identified by Messa *et al.* (1996) as pelagic, dark, silty dolomite or dolomitic siltstone (Figure 4.21). To the south along the lower slope, this layer is hard to correlate between wells, and the "A" and "B" sands must be distinguished by differences in their log character (to be discussed below).

"A" Sand Log Character: Along the upper and middle slope the "A" sand , like the "B", is characterized by low deep resistivity values with a relatively blocky shaped curve. The gamma ray signature is highly variable but generally shows two to three fining up sequences capped by a coarsening up trend that corresponds to a gradual increase in resistivity values and an abrupt change to higher densities (Figure 4.21). The log character at locations within the lower slope is markedly different (Figure 4.33). Here the "A" sand is difficult to recognize. The logs show a pattern of alternating layers of high and low resistivity approximately 30'-50' thick. Similar patterns can be seen in both the density and gamma ray logs. Based on these curves and available photoelectric factor logs, the "A" sand in this region appears to be composed of thickly bedded sandstones, siltstones, dolomitic siltstones, and possibly siliceous or dolomitic limestones or calcareous dolomite (high resistivity, low gamma ray counts, and photoelectric factors near 4 barns/electron).

4.1.6 Post-depositional deformation

An examination of the seismic data shows that in the study area faults within the Bone Spring and overlying formations are generally relatively small-scale, N-S trending reverse faults, largely confined to the boundaries of the N-S ridges. Mapping out individual faults within the Second Sand is problematic. Linear features that may be faults can be seen in a continuity cube generated from the seismic data. On dip maps, these features correspond to arcuate to

linear regions with greater dips than the surrounding surface (Figure 4.34). However, the small offsets or bends in reflectors associated with the majority of these features makes them difficult to identify and follow in the original seismic data. In addition, they generally die off rapidly with depth (often only affecting a few reflections) which makes them hard to resolve with first octave filters as well. It is likely that for many of the faults within the study area, there was sufficient offset to produce the bends or steeply dipping areas seen in the dip map but not enough to produce seismically resolvable offset. As a result, only the largest faults within the Second Sand which could be identified and tracked through the seismic data with certainty were fully mapped.

The largest mappable fault within the Second Sand runs N-S along the western boundary of the eastern ridge from inline 106 to inline 155 (Figure 4.35). In cross-section, it can be seen to offset reflections by 10 ms, roughly half a cycle (Figure 4.36). Several other reverse faults of comparable size and orientation can be seen penetrating the Second Sand at this location as well.

4.2 Discussion

4.2.1 Basin physiography/depositional setting

Three-dimensional seismic mapping has shown that the distribution of the Second Sand is largely controlled by the structure of the underlying units. The orientation and timing of the basement faults indicate that they are related to the Mississippian to Early Permian tectonic activity that resulted in the formation of the Delaware Basin (Mazzullo, 1995). In addition to major uplifts that separated the ancestral Permian Basin into the Delaware, Midland, and Marfa Basins, it appears that this tectonic activity also resulted in the formation of a small sub-basin or intraslope basin which acted as a local depocenter during the deposition of the

Second Sand in Leonardian time (as evidenced by the Second Sand isopach map which shows that the majority of the deposition was concentrated within the central flexure and by the similarity of this sediment distribution and the geometry seen in the Strawn time-structure map). At the Strawn level, this basin is bordered by N-S trending fault bounded ridges on the eastern and western sides of the study area and to the north by the upper slope. The deposition of later sediments modified this topography to some extent. In particular, the prominence of the ridges decreased while the overall relief increased. Presumably, this is the result of continuing subsidence of the basin accompanied by vertical buildup of the shelf margin during highstand carbonate deposition. The physiography of the sub-basin at the onset of Second Sand deposition is characterized by (1) east-west depositional strike, (2) north-south regional dip with a local NW-SE dip within the central flexure, and (3) a steep upper slope grading into a fairly gently sloped basin floor/lower slope. The most notable difference between the structure at the Strawn level and basin configuration at the onset of Second Sand deposition is the change in the geometry of the upper slope. The rather complex series of small re-entrants in the upper slope above the central flexure at the Strawn level has been replaced by a relatively smooth upper slope with only a few more prominent re-entrants, namely the broad re-entrant located in the center of the slope and the smaller more easterly re-entrant just west of the eastern ridge. Whether these re-entrants are the result of erosion by gravity flows, slope failure prior to the deposition of the Second Sand, or some other process could not be determined. Whatever their origin, it is likely these features acted as conduits for the sediment gravity flows that largely filled the sub-basin during the deposition of the Second Sand.
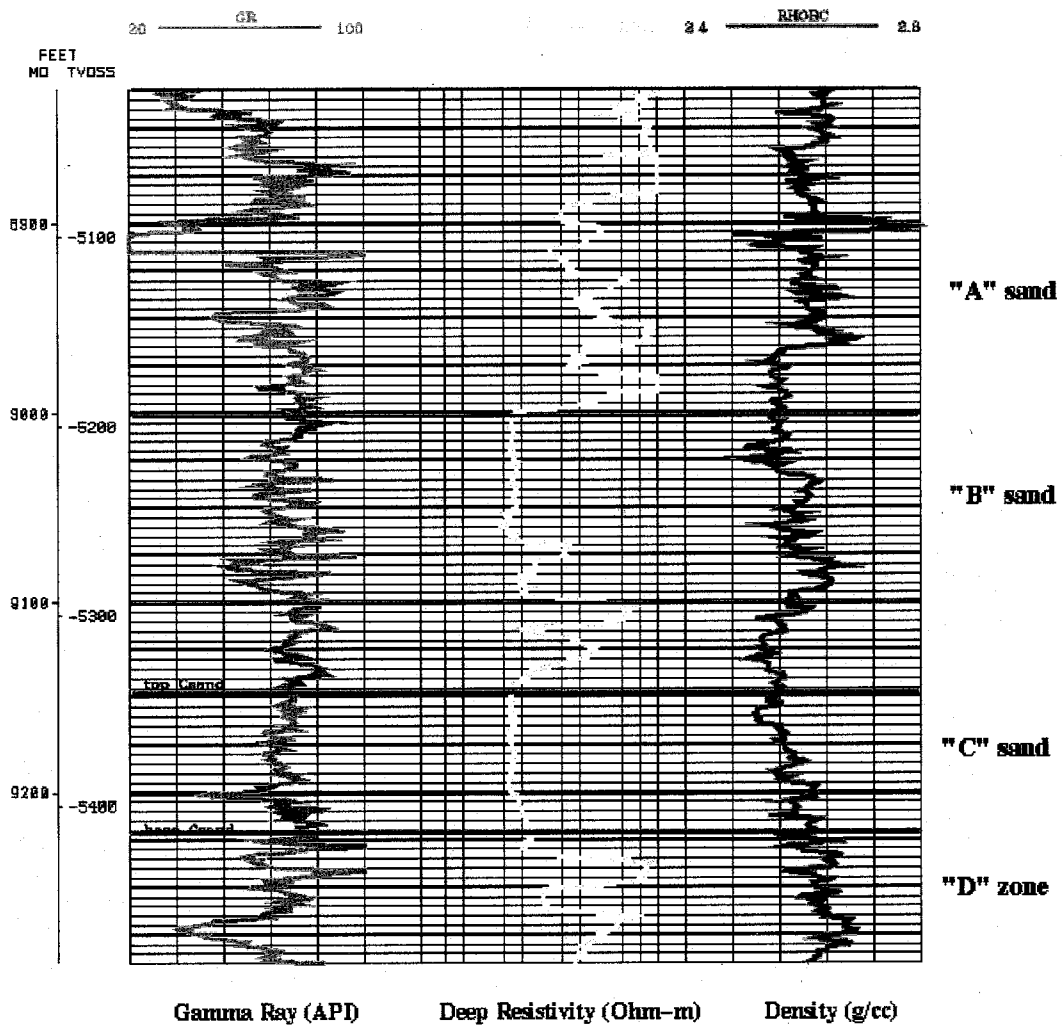
Figure 4.33: Type log for the Second Sand along the lower slope (southernmost portion of the study area). Note the change in the log character of the "A" sand which is now composed of alternating layers of high and low resistivity and gamma ray counts. Compare with the relatively uniform log response of the "A" sand in Figure 4.21.
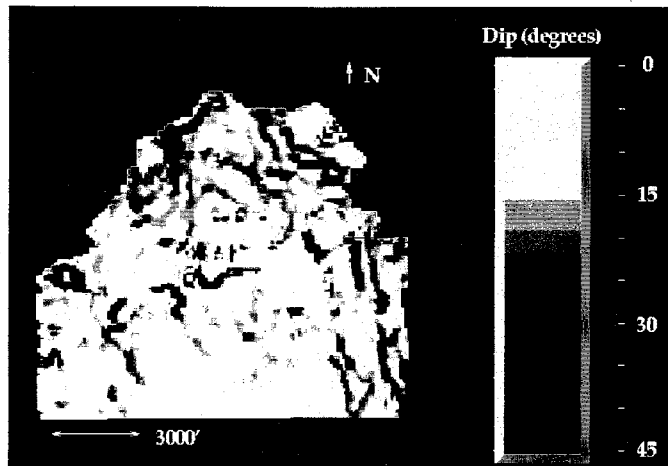
Figure 4.34: Dip map of the top of the "C" sand. Arcuate, steeply dipping regions shown in red correspond to planar features in the coherency cube and may or may not have visible offset in the seismic data..
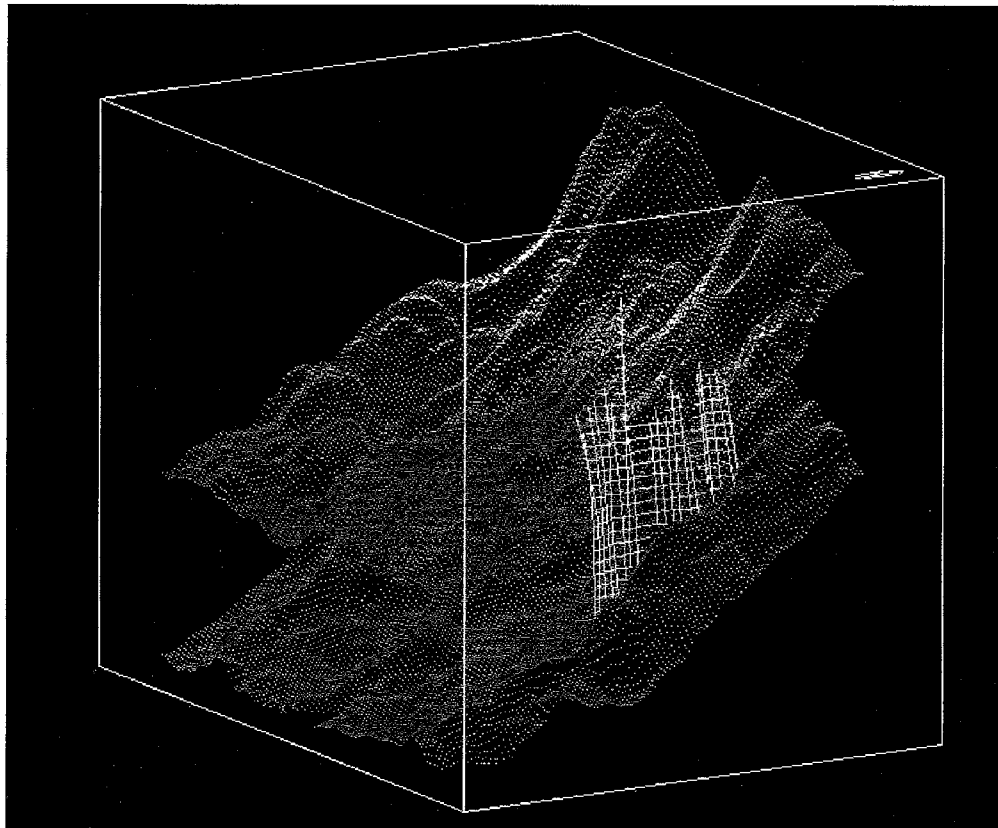
Figure 4.35: Perspective view (looking NW) of the top and base of the Second Sand (colored horizons) and a N-S trending reverse fault cutting the unit (white grid).
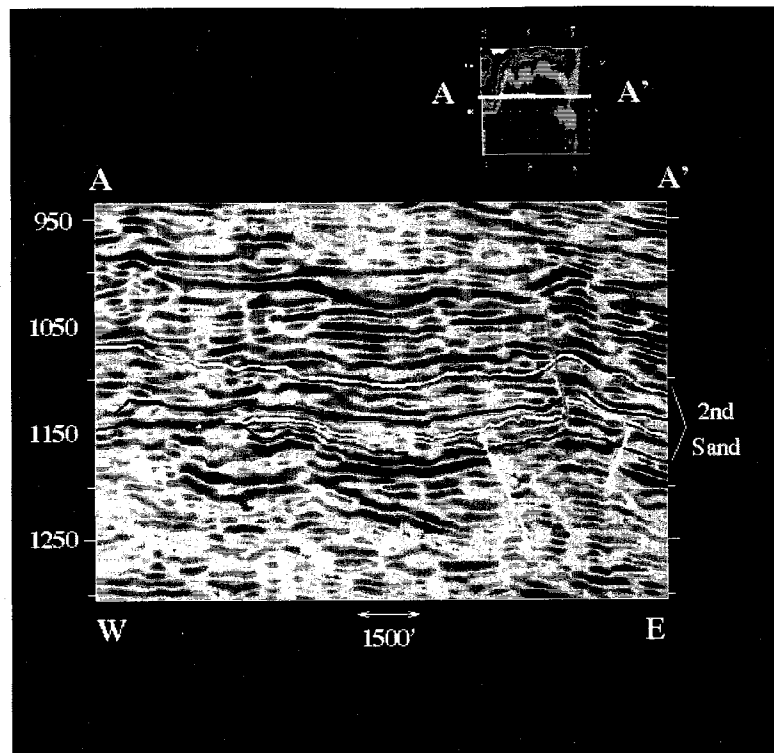
Figure 4.36: W-E cross-section through the seismic data showing faults within the Second Sand. The location of the transect is given in the map view at the top of the figure. The fault shown in green is the same as that in Figure 4.34. The black and yellow horizons within the Second Sand are the top and base of the "C" sand, respectively.

4.2.2 Discussion overview

A discussion of the depositional history and features of the Second Sand is best done within either a facies or depositional model or a sequence stratigraphic framework. In the past few decades, a wide variety of models have been proposed to classify submarine fans and explain their origin and evolution under conditions of changing of sediment supply, sea level, and tectonic activity (see Appendix 2 for a discussion of submarine fan models). The diversity of the models and the somewhat conflicting terminology used to describe ancient and modern submarine fan deposits in the literature is due, in large part, to the different types of data and widely varying scales (e.g. outcrop and oceanographic data vs. seismic data). Although

depositional/facies models provide greater insight into the depositional processes that formed ancient submarine fans, these models are difficult to apply at the scale available with 3-D seismic data. Consequently, the discussion of the geology of the Second Sand will be given terms of a sequence stratigraphic framework.

4.2.5 Sequence stratigraphic model, Second Sand Member of the Bone Spring Formation

Before describing the Second Sand in a sequence stratigraphic framework, it is important to address the issue of scale. Sequence stratigraphic models are based on large-scale features and were developed from extensive 2-D seismic lines or 3-D surveys that provide a regional view of the shelf-slope-basin environment. The present study deals with a 5.75 km^2 survey, a relative "postage stamp" of 3-D seismic data. The shelf and the uppermost slope as well as the true basin plain environment are not represented, and the portion of the slope represented is small in comparison with the total size of the slope adjacent to the Northwest Shelf. Given these limitations, it should be stressed that the sequence stratigraphic model presented below is by no means thought to be representative of the general stratigraphy along the slope of the Northwestern Shelf. Additional data is needed to test the validity of these interpretations in other areas along the northern margin of the Delaware Basin.

Based on their location within the lowstand systems tract, seismic response, and log character, the early, middle, and late period of the Second Sand can be interpreted as (1) a lowstand/basin-floor fan, (2) a slope fan, and (3) a modified lowstand wedge (to be discussed below), respectively. The features seen in the seismic, log, and core data that led to this interpretation, the depositional history, and the departures from the standard lowstand systems tract model will be discussed for each of the three periods in turn below.

71

1. *Lowstand/basin-floor fan:* The three lobes that make up the early period of the Second Sand are interpreted as a basin-floor fan deposit, based on the following observations: (1) In dip views they form a series of clinoforms that downlap the underlying type 1 sequence boundary; (2) individual reflections are fan- to lobate-shaped in plan view; (3) the reflections separate upslope, and the units thin or pinchout over paleobathymetric highs; (4) the upper boundary of the package of reflections is conformable with the overlying slope fan reflections; (5) the reflections are restricted to the base of the slope and basin floor; and (6) the lobes are located downslope from major re-entrants in the upper slope (cf. Posamentier *et al.*, 1988; Posamentier and Vail, 1988; Van Wagoner *et al.*, 1988; Posamentier and Erskine, 1991).

The early period in the deposition of the Second Sand is characterized by bypassing of the upper slope and uppermost middle slope and infilling of the central flexure resulting in an overall reduction in depositional relief. During this period, sediment that bypassed the upper slope was carried out to the lower slope following topographic lows and was deposited in three discrete fan- or lobate-shaped shingles that prograde to the southeast. These shingles are interpreted as being successive lobes within the basin-floor fan with the westernmost lobe (lobe 1) being the oldest and the easternmost (lobe 3), the youngest. The lobes mark the beginning of the lowstand systems tract deposition in this area.

Lobes 1 and 2 appear to have been sourced from the central re-entrant in the upper slope based on their proximity to this feature and their orientation. The effect of the basin topography was most pronounced during the deposition of lobe 1 which is confined to an elongate region adjacent to the western ridge. The slight convexity of the western margin of lobe 1 (the result of basin margin wedging), the upslope pinchout along the western ridge, and the N-S elongation of this lobe, all indicate that sediment gravity flows were moving N-S down the slope and lacked sufficient velocity to flow upslope over the western ridge as they

spread laterally and instead were funneled south along this margin. Overall the effect of this lobe on the basin configuration was to infill a small elongate portion of the basin resulting in a minor smoothing of the topography along the eastern boundary of the western ridge.

The second lobe contrasts markedly with the first in that it is smaller, more radial in plan view, and elongated in the east-west direction. The more radial distribution of lobe 2 sediments may be due to the combined effects of (1) greater sand content which generally results in radial rather than elongate fans (Stow *et al.*, 1996) and (2) decreased topographic constraints in this more central location. The change from deposition on lobe 1 to deposition on lobe 2 is most likely the result of lateral migration of the first fan lobe in response to an increase in or shift to sediment supply from the northwest.

During the deposition of lobe 3, sediment was bypassing approximately the same portion of the slope as during the deposition of lobes 1 and 2, but it was being deposited much further out into the basin (Figure 4.22). Lobe 3 also differs from the earlier lobes in that it had a more easterly sediment source, perhaps the small re-entrant located just west of the western boundary of the eastern ridge (Figure 4.22). Unlike lobe 1, the ridge adjacent to lobe 3 does not appear to have acted as a barrier that focused flow in the N-S direction and prohibited deposition on top of the ridge. Instead sediment appears to have been draped over the ridge indicating a greater component of deposition from suspension or more energetic flows with sufficient velocity to travel up slope onto the ridge. After the deposition of lobe 3, a high frequency rise in relative sea occurred, and active deposition on the fan ceased as evidenced by the well log data which shows a thin layer of pelagic sediment draped over the fan surface.

Based on the log responses, the sediments that make up the basin-floor fan appear to be a mix of shelf-derived siliciclastics and dolomite. Because this interval has not been cored and is not routinely logged, it is not possible to determine if the dolomite is authigenic or detrital (i.e., subaerial erosion of the newly exposed shelf and/or shelf margin carbonates or

submarine erosion of the upper slope). If erosion of the upper slope did occur during this period, it is below the resolution of the seismic data. In addition, there is no clear evidence within the well logs or the seismic data that would indicate a channel/levee system existed at this time.

From the above discussion, it is clear that this basin-floor fan differs substantially from the idealized lowstand fan model. These differences can be attributed to the rate, volume, and type of sediment supplied to the basin and the basin configuration. The model predicts that basin-floor fans should have relatively high sand:mud ratios (with good reservoir potential) due to fluvial incision on the shelf and the erosion of submarine canyons. The fan, ideally, would have fairly well developed channel/levee systems feeding lobes on the basin floor. In cross-sectional views parallel to depositional strike, these lobes would have mounded profiles and bidirectional downlap. This is clearly not the case for the basin-floor fan described above. This portion of the Second Sand contains thin-bedded, low porosity, decidedly sand-poor sediments in small lobes with no upslope channel/levee facies. The most likely explanation for these variations is that there was not a well developed fluvial system on the shelf capable of bringing mixed sand and mud to the shelf edge to be remobilized into sediment gravity flows. Sediment supply appears instead to have been somewhat limited in volume (evidenced by the small size of the lobes and the thinness of individual beds) and restricted in grain size. What siliciclastic sediment was available, may have been brought to the shelf margin by ephemeral streams and aeolian processes (which would favor the preservation of detrital dolomite; Davies, 1997a). When sediment gravity flows were initiated, they appear to have been passively funneled through the pre-existing re-entrants in the upper slope and deposited in detached lobes at the base of the slope. The shape of the individual lobes was controlled by the basin topography, particularly the N-S trending ridges. The mounded shape diagnostic of fan lobes requires deposition on a relatively structureless

basin plain. Thus, instead of mounded cross-sections and bidirectional downlap, we instead see reflections that onlap stuctural highs (western and eastern margins of lobes 1 and 3, respectively) or adjacent lobes (western margins of lobes 2 and 3) and downlap the underlying sequence boundary only when unobstructed (eastern and southern margins of lobes 1 and 2).

2. *Slope fan:* The middle period (the "C" Sand) in the depositional history of the Second Sand corresponds to the slope fan in the lowstand systems tract. This interpretation is supported by (1) the position of the unit within the lowstand systems tract (i.e., it is above the lowstand fan, below the prograding wedge, and occurs on the slope), (2) the onlapping onto the sequence boundary on the upper slope, (3) the fan shape of the reflections in plan view, (4) the pinchouts against paleobathymetric highs, (5) the downlap of the overlying wedge reflections onto the upper boundary, and (6) the existence of a channel/levee system (cf. Posamentier *et al.*, 1988; Posamentier and Vail, 1988; Van Wagoner *et al.*, 1988; Posamentier and Erskine, 1991).

The onset of the middle period marks the beginning of deposition along the upper slope. The two reflections that make up this period, the top and base of the "C" sand, define the upper and lower boundaries of the slope fan. Although it is difficult to draw many conclusions about the slope fan based on the seismic data alone (because there are no internal reflections), some observations can be made regarding the deposition and distribution of the "C" sand. Based on the N-S orientation of the two fan shaped reflections, their location below the central re-entrant, and their upslope pinchouts within it (Figure 4.28 and 4.29), it appears that the re-entrant acted as a conduit for sediment gravity flows throughout the deposition of the "C" sand. Furthermore, flows exiting the confines of the re-entrant spread laterally depositing their sediment load, ultimately burying the lobes of the basin-floor fan, and extending south to an unknown distance beyond the boundaries of the study area. In the

southernmost reaches of the study area, the reflections drape the pre-existing topography to a greater extent implying a larger component of deposition from suspension in this more distal environment. To the east and west, the "C" sand thins and pinches out over the N-S ridges indicating that the ridges were still influencing the distribution of sediment as they had in the early period.

The isopach map of the "C" sand (Figure 4.30) shows that the underlying topography is the primary control on the distribution of the "C" sand. In strike views, the "C" sand appears to have a "channel" shape instead of the typical mounded geometry of a submarine fan (Figure 4.16). Similar geometries have been reported for other ancient submarine fans forming in confined basins where the structural grain runs parallel to the sediment transport direction (Figure 4.37). The thickest regions of the "C" sand are concentrated within the central flexure showing that deposition was largely restricted to the fault-bounded sub-basin. Within the central flexure, individual elongate sediment thicks are oriented roughly N-S. It is possible that these correspond to the axes of small channels within the channel-levee/overbank system. It should also be noted that some of the thicks correspond to small depressions formed where the underlying lobes of the early period overlap (Figure 4.19). Submarine channels of the middle period may have preferentially been located in these topographic lows.

An example of a somewhat similar channel configuration in an ancient submarine fan can be seen in the Miocene age Stevens Fan in the subsurface of the San Joaquin Valley, California. Macpherson (1978) observed a pattern of alternating stacked channel sands with depth in the Stevens fan. He proposed a differential compaction mechanism to account for this pattern. Muds and silts separating channels tends to compact more readily than the channel sands, thus changing the channels into topographic highs. Subsequent turbidity flows would naturally seek the lowest depth and would tend to follow the interchannel areas

Confinement model
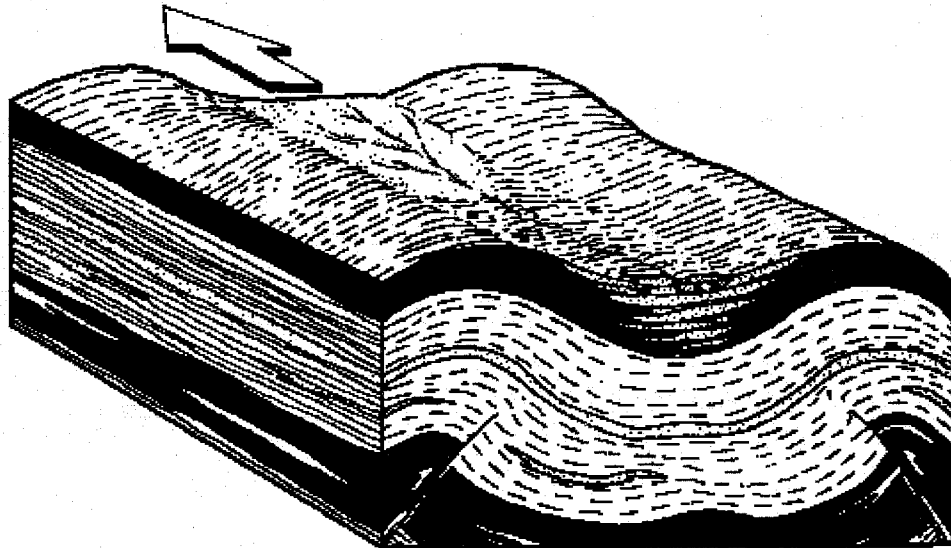
Figure 4.37: Diagrammatic sketch of the Miocene Stevens fan showing the effect of syndepositional tectonic activity on the fan morphology. Sediment gravity flows were funneled along the axis of the trough giving the fan a "channel-shape" geometry in cross-section. Note the similarity between this configuration and that of the Second Sand shown in Figure 4.15 (adapted from Reading, 1996).

creating a series of channels that are offset with depth (Figure 4.38). Although we do not see a series of offset stacked channels with depth (because there are no channels within the early period), the orientation of sediment thicks seen in the "C" sand may be the result of a similar mechanism whereby differential compaction has enhanced the topographic lows present where the edges of adjacent lobes overlap.

The most important aspect of the middle period deposition, namely the development of a sand-rich source area, cannot be imaged with seismic data. By integrating well logs and cores with the seismic data, it becomes apparent that the most striking difference between the early and middle periods is the change from the deposition of low porosity, dolomite-rich sediments to more porous siliciclastic sediments, albeit with a very limited range in grain size (fine silt to very fine sand). This increase in the siliciclastic sediment supply could be due to the establishment of a more effective fluvial transport system that was capable of transporting
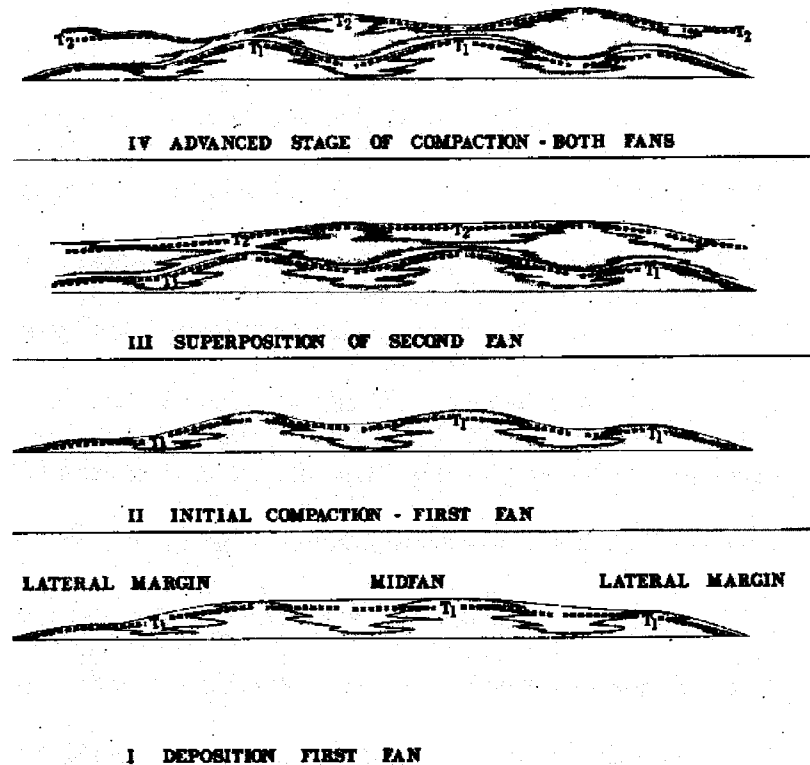
Figure 4.38: Offset, stacked channels in the Miocene Stevens Fan. T1 and T2 are time lines showing how the surfaces of the fan changed due to differential compaction (MacPherson, 1978).

sediment out to the shelf margin or due to rising sea level intercepting sediment supply systems already existing on the shelf. However, the increased sand content of the slope fan could also be explained by an increase in aeolian activity. Previous workers (Silver & Todd, 1969; Gawloski, 1987; Saller *et al.,* 1989; Messa *et al.*, 1996) have suggested both fluvial and aeolian components to the sediment supply for the siliciclastic members of the Bone Spring Formation. Similar aeolian sources have also been proposed for the turbidites in the overlying Delaware Mountain Group (Kocurek & Kirkland, 1998). An aeolian component is favored by these workers because of the limited range of grain sizes present, the well sorted nature of the sediments, the noticeable lack of mud, and the unique climatic conditions existing during the Permian and Triassic. During this time, the supercontinent Pangea

extended from as far north as latitude 85N down to a latitude of 90S (Davies, 1997b). Paleoclimatic models suggest that with a substantial exposed landmass such as this, the atmospheric circulation patterns would be disrupted on a global scale creating a unique climatic system that transcended latitudinal boundaries (Davies, 1997b). This climate has been described by some as "megamonsoonal" (Dubiel, 1994). Additional evidence in the form of evaporite deposits and other paleoclimatic indicators show that during the Permian, the Northwestern Shelf climate became increasingly arid with winds coming from the northeast, and fluvial systems on the shelf tended to be ephemeral (Kocurek & Kirkland, 1998). In this setting, dune fields could migrate out to the shelf margin and eventually be remobilized into sediment gravity flows and carried out into the basin.

The change in the volume, rate, and type of sediment supplied to the slope and the inferred rise in relative sea level had several effects on the deposition of the Second Sand. The focus of deposition shifted to higher up on the slope, a significantly larger fan system developed, and a channel/levee system was established that graded down fan into more distal turbidites and hemipelagic sediments. In log cross-sections the channel facies is relatively broad and shallow in comparison with the overall size of the slope fan, and parallel to depositional strike the channel facies appears to thin gradually and grade into the levee/overbank facies without any indication of steep channel walls or high-relief levees. These observations support an interpretation of deposition in an axial system of rapidly migrating channels rather than a single stable feeder channel with associated high relief levees and down slope distributaries.

Overall, the "C" sand slope fan does not differ significantly from the slope fan model. The most notable departures from the model are (1) better quality reservoir facies in the slope fan than found in the basin-floor fan, and (2) the lack of an external mound-shape geometry.

The former is a reflection of the atypical nature of the basin-floor fan while the latter is due to the basin geometry.

3. *Modified lowstand wedge:* The seismic expression of the sediments that were deposited during the late period has many features in common with the prograding lowstand wedge described in the literature. For example, the late period has an overall wedge-shaped geometry; it occurs above the slope fan; its upper boundary is the top of the lowstand systems tract; the internal reflections are a series of clinoforms (progradational to aggradational reflection configuration); and there is a greater proportion of chaotic reflections in the down slope region of wedge (potential debris flow deposits). However, there is nothing to indicate that these deposits are the result of a delta prograding onto the slope, the common interpretation given in lowstand systems tract models (e.g. Posamentier *et al.*, 1988; Posamentier and Vail, 1988; Van Wagoner *et al.*, 1988; Posamentier and Erskine, 1991). Hence, there is a need to adjust the model to make it applicable to the late period of the Second Sand. This new model will be referred to as the modified lowstand wedge. The main difference between the two is the *way* in which the reflections prograde. Consider the original progradation wedge model shown in Figure A2-2 (Appendix 2). In this model, sediments prograde from the shelf out onto the slope, and the seismic reflections expected would onlap the shelf and prograde on the slope. Compare this with the modified progradational wedge shown in Figure 4.39. In this model, the initial deposition is aggradational with reflections extending over entire slope. Later sediments progressively bypass the upper slope resulting in a toplap reflection configuration along the upper boundary. This type of geometry could be the result of fan deposition during rising sea level followed by period of sea level fall. Intitially during the period of rising sea level, there is ample accommodation space, and a fan forms and is fed by a feeder channel or submarine canyon which joins down slope with a channel/levee system. The fan builds, and the slope aggrades as the focus of deposition
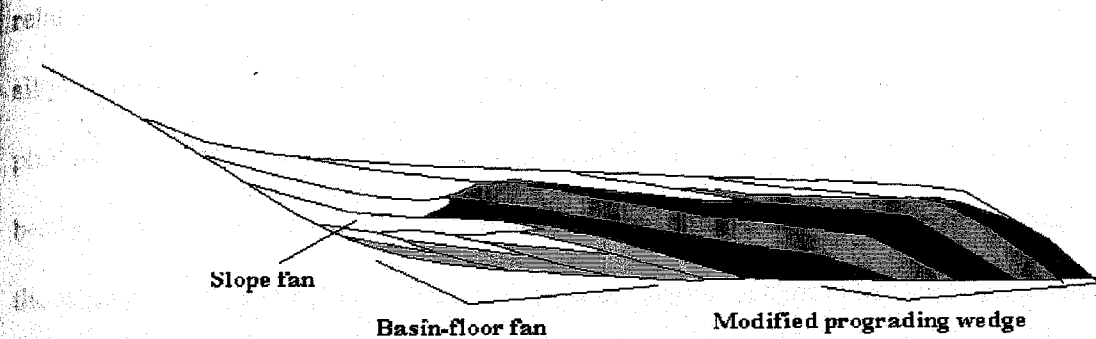
Figure 4.39: Proposed sequence stratigraphic model for the Second Bone Spring Sand.

moves upslope from its lowstand level. As the relative sea level rise slows or reverses, the available accommodation space on the slope decreases, sediment progressively bypasses the upper and middle slope, and the fan progrades out into the basin.

In terms of the late period in the deposition of the Second Sand, the rising relative sea level stage would correspond to the reflections produced by the "B" sand at the base of the late period which are continuous over the majority of the slope. Well logs through the "B" sand show that it thickens towards the north central portion of the study area and that as it thins down slope, the frequency of silty/shaley interbeds increases. The thin pelagic layer separating the "A" and "B" sands marks the end of this period of deposition. The change to pelagic sedimentation could be the result of a rise in relative sea level (a period of basin starvation) or a shift in source of the siliciclastic sediment (away from the study area) and the dominance of the background hemipelagic sedimentation. The second period within the modified prograding wedge model corresponds to the "A" sand. The seismic data show that during the deposition of the "A" sand sediment progressively bypassed the upper and middle slope. Log cross-sections perpendicular to the depositional strike illustrate the marked downslope change in "A" sand. The "A" sand thickens downslope and changes from a

relatively uniform, medium-bedded, fairly clean sandstone to interbedded sandstone and silty/sandy limestones or calcareous sandstones (low gamma ray counts, high resistivity, and photoelectric factors between 3 and 4 barnes/electron). The acoustic impedance contrasts between these interbeds could result in the series of clinoforms that make up the majority of the wedge in the seismic data. In plan view, these clinoforms tend to have a more sheet-like geometry rather than the fan shapes seen in earlier periods. This may indicate that there was no channel/levee system at this time, and sheet sands and debris flows (the mounded/chaotic facies) dominated the system.

The reservoir quality of the "A" and "B" sands is somewhat poorer than that of the "C" sand. However, the gamma ray logs do not show noticeably higher values in the "B" and "A" sands compared to the "C" sand, implying that the poorer reservoir quality seen in these sands is not due to an increase in the shale:sand ratio. Porosity within the "A" and "B" sands is on average slightly lower than the underlying "C" sand, and photoelectric factors for the "A" and "B" sands are slightly higher than those seen in the "C" sand. This may indicate that the controlling factor in reservoir quality in these sands is the proportion of calcite or dolomite cement.

4.3 Conclusions

Based on an integrated analysis of the well, seismic, and core data, the primary factors controlling the distribution and nature of sediment within the Second Sand in the study area are: (1) the structure of the underlying units, (2) sediment type and availability, and (3) high-frequency relative sea level fluctuations.

Faulting and flexures associated with the formation of the Delaware Basin created a small intraslope basin that occupies the majority of the study area. This sub-basin acted as a local depocenter during Leonardian, and Second Sand deposition within the study area resulted in

accumulations of 400' to 500' of very fine to fine sands and silts and culminated in the near complete infilling of the sub-basin.

The depositional history of the Second Bone Spring Sand in the study area can be subdivided into an early, a middle, and a late period which correspond to a basin-floor fan, a slope fan, and a modified prograding wedge, respectively. The differences in the geometry and sediment type among these periods are controlled by a combination of sediment supply and sea-level fluctuations. During the early period, the basin-floor fan developed under conditions of low sea level and limited siliciclastic sediment supply. As a result, the basin-floor fan is relatively small, confined to the deepest part of the sub-basin, and composed of low porosity, dolomitic sediments with virtually no reservoir potential. In contrast, the slope fan onlaps the upper slope and contains a significantly greater proportion of high porosity, sand-rich sediments which argue for a rise in relative sea level and the development of a siliciclastic source and sediment dispersal system on the shelf (aeolian or fluvial) capable of bringing sediment to the shelf edge where it could be remobilized into sediment gravity flows. The onset of late period deposition marks a return to a decreasing relative sea level or stillstand as evidenced by the progressive bypassing of the upper and middle slope and a change to deposition of more heterogeneous sediments that may have a greater proportion of debris flows.

Post-depositional faulting within the Second Sand resulted in minor offsets of these deposits and tends to be restricted to the boundaries of the east and west margins of the sub-basin. Although this faulting did not result in significant offsets or deformation within the Second Sand, it does have implications for the fluid flow properties of the Second Sand to be addressed in the following chapter.

5. Seismic-Guided Reservoir Characterization

5.1 Seismic Attribute Analysis Methods

The goal of this phase of the study was to predict the porosity distribution of the Second Bone Spring Sand using seismic attributes. Horizon- and window-based attribute analyses (cf. Schultz *et al.*, 1994) shed light on which attributes were related to porosity, but the results did not have the desired accuracy, so a volume-based technique (Russel *et al.*, 1997; Schuelke *et al.*, 1998) was used instead. The volume-based attribute analysis differs from the horizon or interval approach in that the goal of the volume-based approach is to correlate physical properties in the z direction as well. In other words, instead of trying to predict average porosity or feet of net pay, for example, within the Second Sand at each trace location, the goal is to predict a porosity *curve* at each trace location. To do this, instantaneous, single or multitrace attribute curves are extracted from the seismic data at each well location and used in the prediction of the porosity curve. While this may seem computationally difficult, in reality it is quite simple. The methods used are similar to the horizon-based approach using average attributes and porosity ($a_{i\ avr}$, and ϕ_{avr}, respectively), but the data set changes from a set of points of the form (x, y, ϕ_{avr}, $a_{1\ avr}$, $a_{2\ avr}$, ..., $a_{n\ avr}$) to data points of the form (x, y, t, $\phi(t)$, $a_1(t)$, $a_2(t)$, ..., $a_n(t)$) at each well location where t is two-way travel time, $a_i(t)$ are instantaneous attributes, and $\phi(t)$ is porosity. A volume can be created using the predictive relationship to transform each seismic trace or wiggle into a porosity log.

The main drawbacks of this technique are the restrictions placed on the wells that can be used in the analysis. Every well used must be tied properly at each time sample, i.e., there must be a strong similarity between the synthetic and seismic traces throughout the analysis window, both for major and minor events. The obvious disadvantage of this is that it

decreases the number of wells that can be used in the study (generally to those with a sonic log or some type of pseudo sonic log) and makes the well data set less able to represent the lateral heterogeneity of the reservoir. However, if the analysis window is sufficiently wide, by using every time sample within the window the reservoir heterogeneity will be captured in the vertical direction instead, and the number of data points may actually be greater than if every available well had been used. For the interested reader, additional information on the principles behind seismic-guided reservoir characterization and a summary of the earlier horizon-based attribute analysis are available in Appendices 3 and 4, respectively.

The methods used in the volume-based attribute analysis of the Second Sand can be divided into nine steps:

1. Defining/creating the well data set
2. Defining the analysis window
3. Attribute selection
4. Primary attribute extraction
5. Secondary attribute extraction
6. Generalized linear regression
7. Cross validation testing
8. Creating the porosity volume
9. Creating porosity and net pay map

Step 1—creating the well data set: The goal in creating the well data set was to pick a subset of wells that 1) had the necessary data to construct effective porosity logs, 2) were representative of the area, and 3) could be adequately tied to the seismic data. To meet the first requirement, the well data set was limited to those wells that had both density and neutron porosity logs. This was necessary because porosity well logging tools do not actually measure porosity directly, but instead they measure a variety of properties that can be related back to porosity. The most common porosity tools use radioactive sources that

emit gamma rays (density porosity tools) or thermal and epithermal neutrons (neutron density tools). The gamma rays and neutrons pass through the formation and the returning energy is measured at a detector slightly uphole from the source. The way in which a formation slows or absorbs gamma rays or slows or captures neutrons provides information about the electron density of the formation and the hydrogen index, respectively. Both of these properties can be related back to porosity if the lithology is known. Because lithology is generally unknown, it is necessary to assume values for the matrix and fluid density in order to calculate porosity from the response of a single tool. The matrix assumed is usually limestone, dolomite, or sandstone, and the resulting porosity is reported in limestone, dolomite, or sandstone porosity units. In order to convert these units into the actual porosity of the formation, a combination of two tools is necessary to determine the two unknowns, porosity and lithology.

For this reason, the subset of wells to be used in the seismic attribute analysis was narrowed down to those that had both a neutron density and density porosity or bulk density log. The two curves were crossplotted to produce a "crossplot" or effective porosity log for each well. In the porosity determination the fraction of shale was assumed to be negligible. This assumption is based on earlier work by Messa *et al.* (1996) which showed that the volume of shale was below 15 %. Measured core porosities were also reported by Messa *et al.* (1996), but the correlation between core porosity and log porosity is somewhat weak (Figure 5.1). Because of the ambiguity in this relationship, I have chosen not to correct the effective porosity logs using the linear regression equation because this correction could easily be applied to the predicted porosity volume after the analysis if so desired (thus, circumventing the additional error that the core-corrected porosities could bring to the seismic attribute analysis).
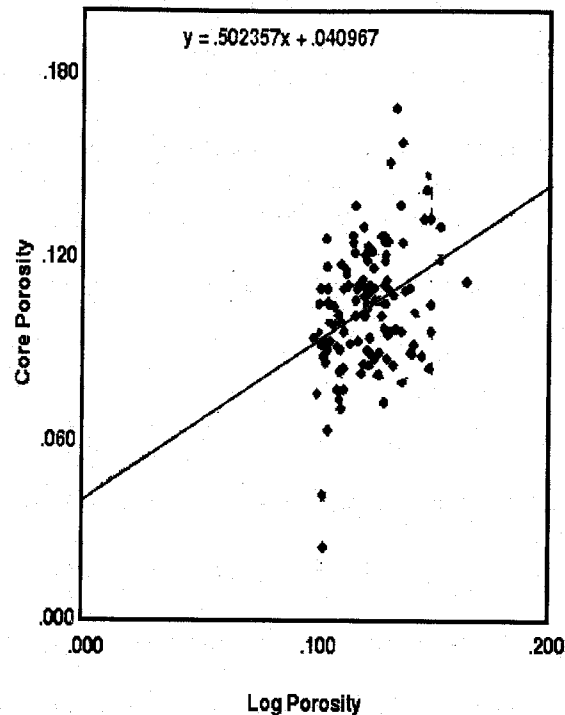
Figure 5.1: Core porosity versus porosity measured by well logs from four cored wells within the study area (adapted from Messa *et al.*, 1996).

The set of wells was next restricted to five wells that were tied to the seismic data using the methods described in Chapter 3, and one additional well for which a pseudo-sonic log was created. The pseudo-sonic log was generated with a standard multiple linear regression technique using well logs from the five other tied wells. The five sonic logs were the independent variables, and the dependent variables were the deep resistivity and porosity logs. The method used to determine the optimal number of dependent variables is the same as that used in the multiattribute analysis that will be described in detail in Step 6. The effective porosity logs used in the multiattribute analysis were converted to two-way travel time using the time-depth relationships obtained from the well-tying procedure.

Step 2—defining the analysis window: While it is possible to perform an analysis over the entire length of the well log, it is not practical or reasonable to expect a single relationship to be able to predict porosity when lithologies and the factors controlling the porosity vary throughout the interval (not to mention possible variations in the wavelet with depth). The window used for the analysis is the entire Second Sand defined by the well log picks and the seismic horizons.

Step 3—choosing the attributes: Attributes were selected for correlation testing on the basis of the results from the earlier horizon-based analysis (Appendix 4) and by examining 2-D crossplots of various well logs versus effective porosity to see if any other property, such as acoustic impedance, correlated with porosity. Additionally, attributes that had been reported in the literature as being effective predictors of porosity were also considered.

Step 4—primary attribute extraction: For this study, primary attributes are those that are extracted directly from the seismic data, either from the seismic trace or the complex trace. Attributes were extracted from the seismic data within a trace capture radius of 110' at each well location using Hampson-Russell's EMERGE multiattribute analysis program. The resulting attribute curves at each well location are the average of the attribute curves from the four surrounding traces within the capture radius and the trace actually at the well bore. The primary attributes that were extracted are:

♦ Amplitude envelope
♦ Instantaneous frequency
♦ Instantaneous phase
♦ Amplitude-weighted frequency (the product of instantaneous frequency and the amplitude envelope)
♦ Amplitude-weighted phase (the product of instantaneous phase and the amplitude envelope)

♦ Average frequency (the moving average of the frequency determined by taking the average of the amplitude spectrum over a symmetric window around the point of interest)

♦ Dominant frequency

♦ Integrated absolute amplitude (the difference between the running sum of instantaneous amplitudes and the smoothed envelope)

Step 5—secondary attribute extraction: Secondary attributes are those that cannot be directly calculated from an individual trace. Two types of secondary attributes were used in this study: coherency/continuity attributes and seismic acoustic impedance. Before attribute curves could be extracted at the well locations, instantaneous attribute volumes had to be created. Two coherency/continuity volumes (average and minimum coherency) were generated using Landmark Graphics' Poststack/PAL application. The average coherency was calculated by comparing two adjacent traces over a 30ms window with a maximum shift of 5ms. The minimum coherency was determined with the same parameters but using a four trace comparison pattern instead. For the former, the average value of the coherency seen in the comparison was assigned at each time sample. For the latter, the value assigned at each time sample was the minimum coherency seen in the four trace comparison. Attribute curves were extracted from the volumes at the well locations (a capture radius of zero).

The final attribute volume created was seismic acoustic impedance. This was created by way of a seismic inversion using Hampson-Russell's STRATA interpretation and seismic data processing package. There are numerous ways in which to invert seismic data to produce an estimate of the acoustic impedance, and none of these produce a unique result. One of the ways around this difficulty is to use the well data to some way constrain the inversion. The type of inversion used in this study is a model-based blocky stratigraphic inversion. The first step in the inversion was to create a simple stratigraphic model using seismic horizons and well logs. The seismic horizons define the stratigraphic layers, and the

distribution of the acoustic impedance within the layers is constrained by sonic and density logs at the wellbores. The five wells tied with sonic logs were used in this phase, and their sonic and density logs were weighted by distance and then stretched and squeezed to fit within the seismic horizons, thus creating the initial velocity and acoustic impedance models. The software algorithm uses this information as a constraint to iteratively determine the acoustic impedance structure whose forward synthetic most closely resembles the actual seismic response. The wavelet used to create the forward synthetic was the arithmetic average of the wavelets extracted from the five wells used in the inversion. The quality of the inversion result was qualitatively checked by examining an error plot (the difference between the synthetic and real seismic data).

Seismic acoustic impedance is not considered by some to be a true seismic attribute because it depends to some extent on well data. Although the well data is necessary both to constrain the inversion and to add the low frequency component missing in seismic data, using well data (however indirectly) as a dependent variable in the analysis may compromise the resulting porosity prediction. To circumvent this problem, a 50 ms smoothing filter was applied to the inversion result to remove any high frequency component contributed by the well logs. Attribute curves were extracted at the well locations from both the original inversion result and the smoothed result.

Step 6—generalized linear regression: Generalized linear regression solves the same set of equations as a standard linear regression, but the weights are convolutional operators rather than constants. This means that instead of looking for the best single weight to be used on every time sample of a given attribute curve, a symmetric time window around each of the attribute curve's time samples is used, and a linear regression is performed to determine the best set of weights to apply to the samples within the window in order to predict the porosity

value at the center of the time window. Thus, the predicted physical property curves will be determined by convolving each set of weights onto the corresponding attribute curves and summing the result. The advantage of this is that the shape of the attribute curves can be taken into consideration in the analysis. The multiattribute analysis was performed using Hampson-Russell's EMERGE application. The algorithm looks for multiattribute correlations using a generalized linear regression technique in the following manner:

a. Nonlinear transforms are applied to both the target logs and the attribute curves.
b. A generalized linear regression analysis is completed for each attribute (both the original and transformed attributes) and porosity, and each individual attribute is ranked by its ability to predict the target logs using the root mean squared (RMS) error of the prediction.
c. The best single attribute (in terms of RMS error) is chosen.
d. This attribute is then paired with each of the remaining attributes, another generalized linear regression is performed, and the pairs are ranked by their ability to predict the target logs.
e. The best pair of attributes is chosen.
f. Similarly, this pair is then combined with each of the remaining attributes to find the best triplet and so forth.

Step 7—cross validation: The result of Step 6 is a set of predictive relationships each using an increasing number of attributes. Mathematically as the number of attributes increases, the prediction error will decrease and ultimately approach zero. However, there is a critical point at which the additional attributes are not actually improving the prediction (despite the improvement in the RMS error) but are instead modeling noise. Cross validation testing can be used to find the optimal number of attributes to be used. This is accomplished by excluding each well one at a time and predicting the excluded target logs with each of the multiattribute predictors determined in Step 6. Next, the average RMS prediction error for each of the predictors is calculated and plotted against the number of attributes used. Typically, the cross validation plot will show a decrease in the average RMS error as the number of attributes increases up to a point. At this point, the average error suddenly

increases indicating that the predictor has become too specific to the target logs and has begun to model noise. The best predictor is, therefore, the one that corresponds to the minimum point on the curve just before this jump occurs.

Step 8—creating the porosity volume: Once the best multiattribute predictor was found, the set of convolutional weights was applied to the attributes. The end result is that the traces in the seismic data volume are used to generate psuedo-porosity logs. Because the software automatically processes the entire seismic volume in this fashion, it is important to keep in mind that outside the analysis window (defined in the seismic data by the interpreted horizons) the porosity logs have no meaning. It cannot be assumed or even expected that a predictive relationship developed in the Second Sand will be a good predictor in the surrounding carbonate units where the porosity may be controlled by entirely different factors.

Step 9—creating porosity and net pay maps: In order to generate maps of average porosity and net pay, the porosity volume was treated as a seismic data volume and loaded into Landmark's seismic interpretation package. From this platform, it was possible to extract attributes from the porosity volume. In this case, extracted reflection amplitudes are actually the predicted porosities. Average amplitudes were extracted over windows defined by the structural horizons to create maps of average porosity. A second attribute, "percent greater than" (a formation attribute that measures the fraction of amplitudes over a threshold value), was used in the net pay determination. The threshold used was the net pay cutoff porosity. The net pay map was created from the attribute map using the following equation:

$$\text{net pay (ft)} = [\text{percent greater than}]*[\text{isopach (ft)}] / 100$$

Note that in order to convert porosity values to net pay (measured in ft), it was necessary to convert the isochron map to an isopach map (measured in depth). To this end, the well and the seismic data were kriged to produce an isopach map. The technique used was collocated cokriging, assuming a linear relationship between the seismic and well data variograms.

5.2 Seismic Attribute Analysis Results

The results consist of 1) the pseudo-sonic log results, 2) the inversion result, and 3) the multiattribute analysis results. Because the first two are somewhat intermediate and peripheral to the actual multiattribute analysis, these will only be presented briefly in Sections 5.2.1 and 5.2.2 before moving on to the multiattribute analysis results in Section 5.2.3.

5.2.1 Pseudo-sonic log results

The deep resistivity and gamma ray logs were found to be the best predictor of the sonic log response of the Second Sand. The weights determined in the linear regression are shown below in Table 5.1.

Attribute	Transform	Weight
Deep resistivity	$1/x$	88917.43
Porosity	x^2	4121.63
Constant	n/a	2924.78

Table 5.1: Weights and transforms used in the pseudo-sonic log linear regression.

This relationship has a correlation coefficient of 0.82056 and an average prediction error of 3.04488 µs/ft (Figure 5.2). In a more qualitative approach, plots of the predicted and actual logs (Figure 5.3), show a strong similarity between the two with the exception of a few spikes within the sonic logs. The linear regression equation was used to create one pseudo-

93

sonic log which was used to tie another well to the seismic data (Figure 5.4), expanding the well data set to include a total of six wells (three dry holes and three producers). The locations of the wells used in the seismic attribute analysis is shown in Figure 5.5. Although the number of wells has been substantially reduced from the 34 used in the horizon-based approach, the total number of data points to be included in the volume-based analysis has increased from 34 (one data point at each well location) to 136 (four fold increase) because we now have a data point every 2 ms on the time-converted well logs. As a result, the vertical heterogeneity of the reservoir is captured.

5.2.2 Seismic inversion results

The initial velocity model used to constrain the inversion is shown in Figure 5.6, and the wavelet used in the inversion is the average wavelet shown in Figure 4.1. In the velocity model, the Second Sand can clearly be seen as a zone of lower velocity between the Second
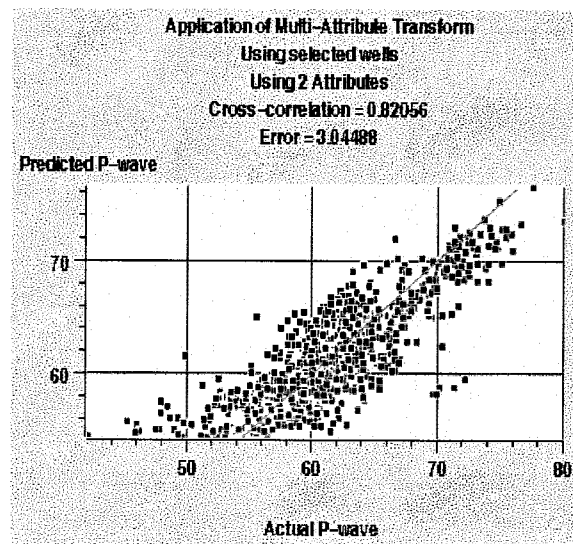
Figure 5.2: Predicted versus actual sonic log response (μs/ft). The red line is the y = x line, and similarly colored data points belong to the same well. All data points are not visible due to the density of points around the regression line.

94

and Third Carbonates. Similarly, the seismic acoustic impedance volume created in the inversion also shows the Second Sand as a zone of low acoustic impedance. Within the Second Sand, the lowest acoustic impedance values occur in the "C" sand. Beneath the "C" sand faint, dipping layers that correspond to the lobes of the early period can be seen (Figure 5.7 and 5.8). The overall blocky appearance and the minor vertical striping in the acoustic impedance volume are byproducts of the inversion method used and were minimized as much as possible.
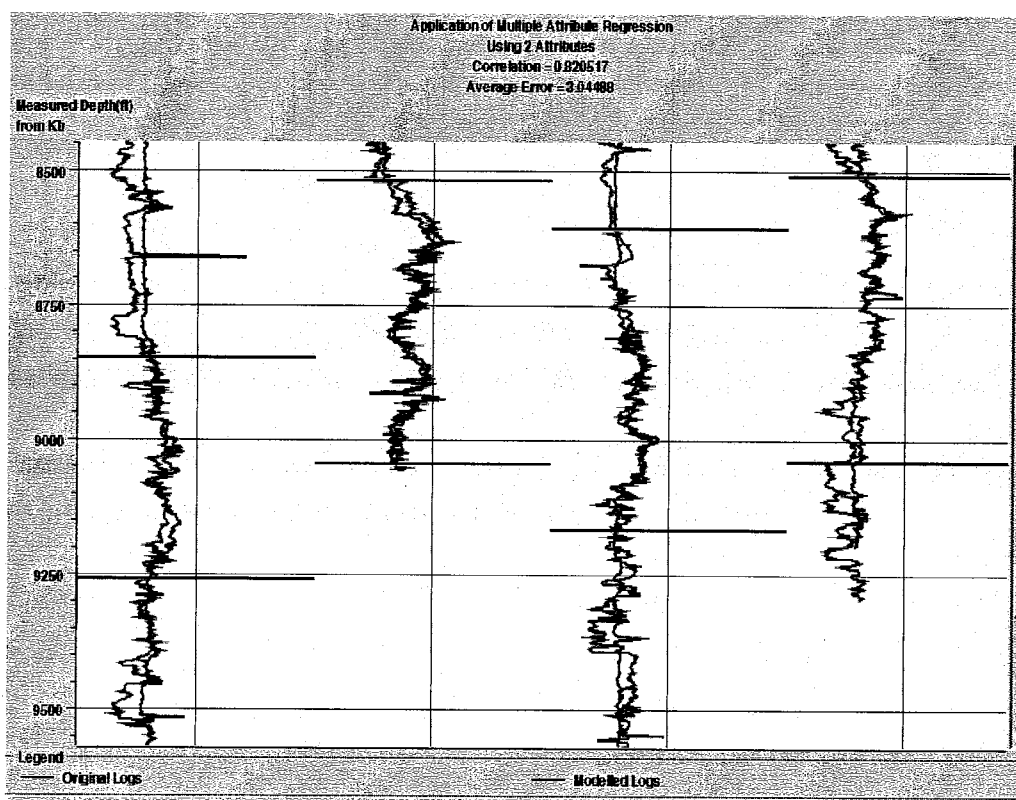
Figure 5.3: Sonic logs (red) predicted from deep resistivity and porosity logs. The original sonic logs are shown in blue. The heavy black lines mark the top and base of the analysis window (corresponds to the top and base of the Second Sand).
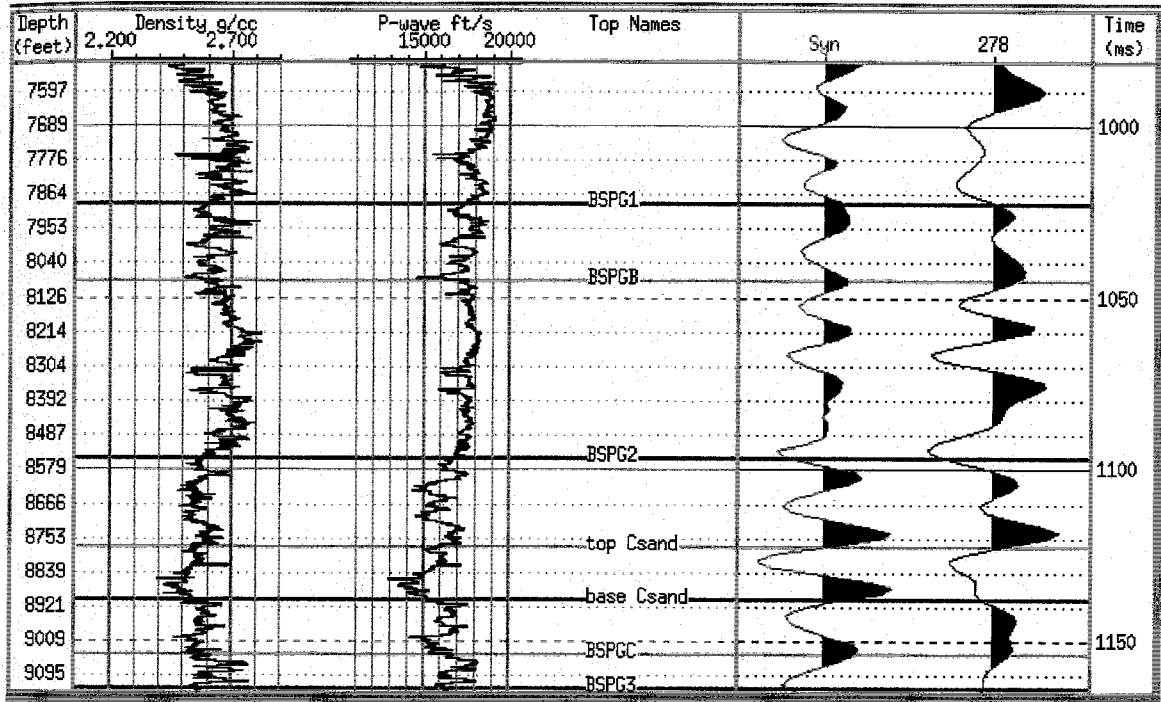
Figure 5.4: The synthetic seismogram generated from the pseudo-sonic log. From left to right the curves are: the density log, the pseudo-sonic log, the synthetic trace, and the actual seismic trace.
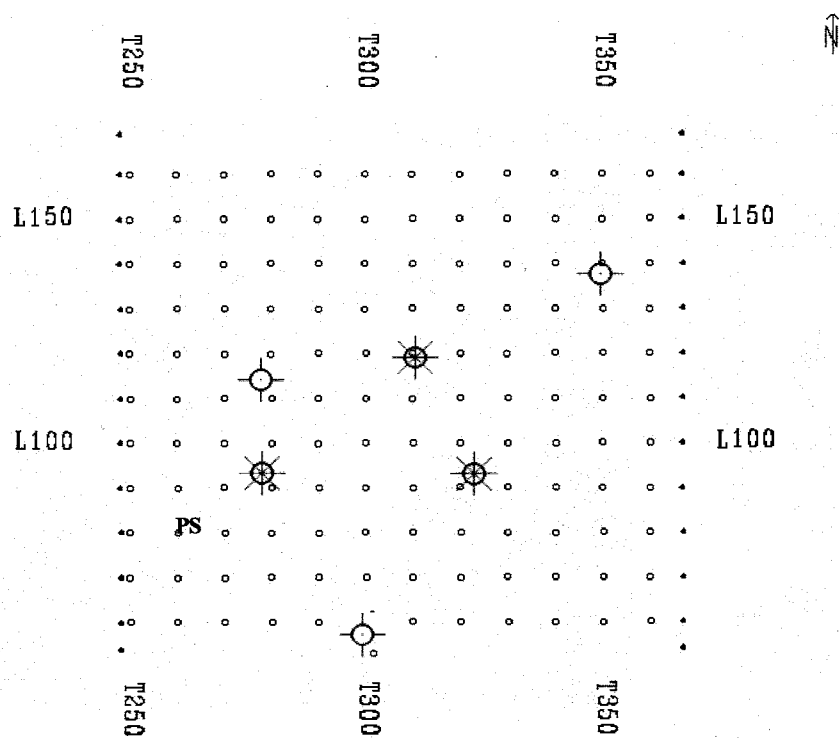
Figure 5.5: Location of wells used in the multiattribute analysis. Circles with two spokes indicate dry holes while circles with three spokes indicate oil and gas wells. "PS" marks the well with the pseudo sonic log
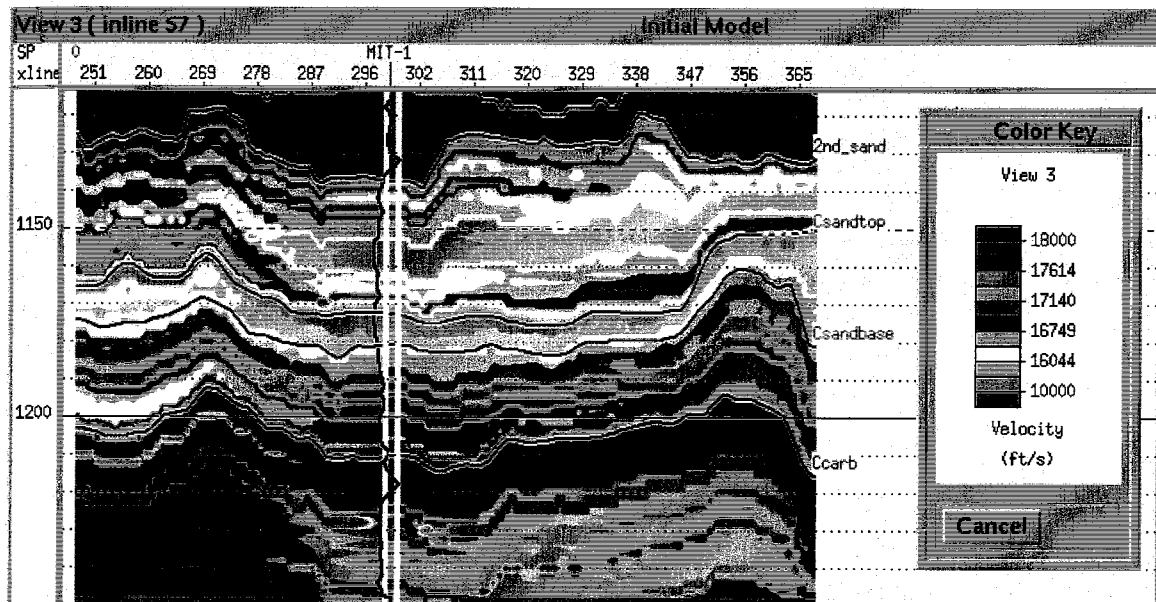
Figure 5.6: An E-W cross-section (inline 57) through the initial velocity model used in the seismic inversion. The heavy black line is a sonic log from a well intersected by the cross-section. The blue lines are the seismic horizons used in created the velocity model.
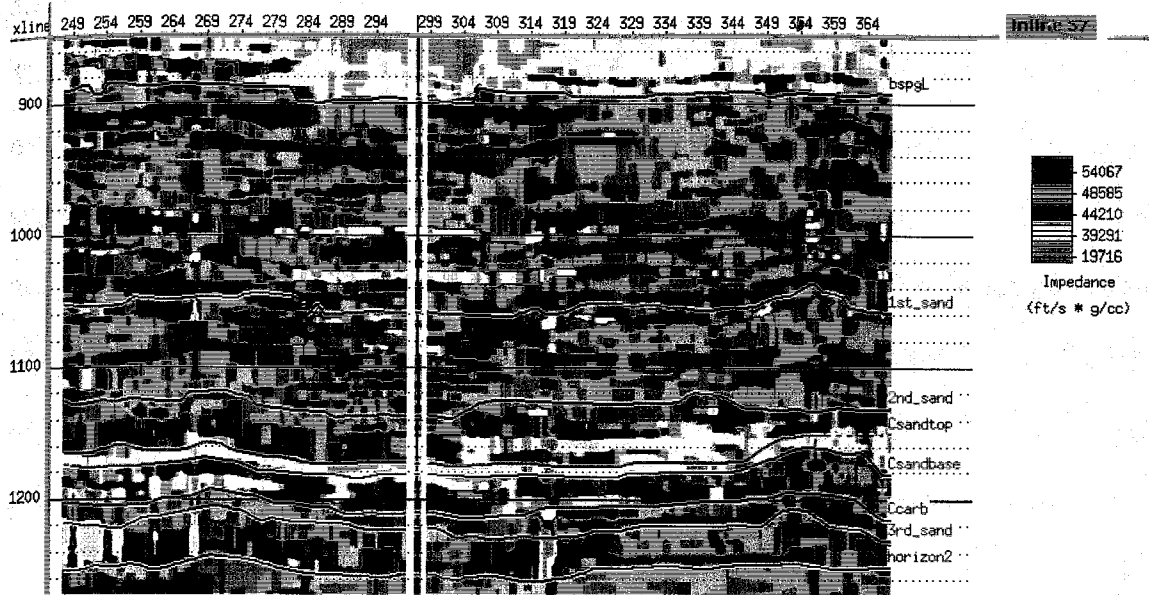
Figure 5.7: An E-W cross-section through the acoustic impedance volume along inline 57 (see reference map in Chapter 4 for location). Cold colors indicate regions of low acoustic impedance, and warm colors correspond to low acoustic impedance. The blue lines are the horizons used in the velocity model.
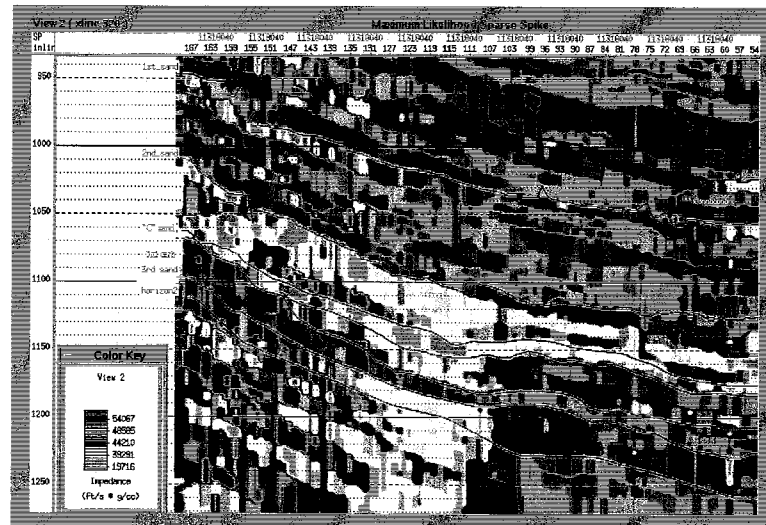
Figure 5.8: A N-S cross-section through the seismic acoustic impedance volume. The blue lines are seismic horizons used in the velocity model. Note the shingling of high and low acoustic impedance layers at the top and base of the Second Sand.

5.2.3 Volume-based attribute analysis results

The results of the attribute analysis consist of a ranking of single and multiattribute porosity predictors. The attributes considered, the nonlinear transforms applied, and the single attribute correlation coefficients are tabulated in Table A5-1 in Appendix 5. Individually, none of the attribute curves correlate strongly with porosity curve. This is apparent from either a qualitative comparison of the attribute and porosity curves (Figures 5.9 and 5.10) or by examining the correlation coefficients (Table A5-1) which are all below 0.33. However, as additional attributes are included in the equation, the correlation strengthens (Table 5.2).
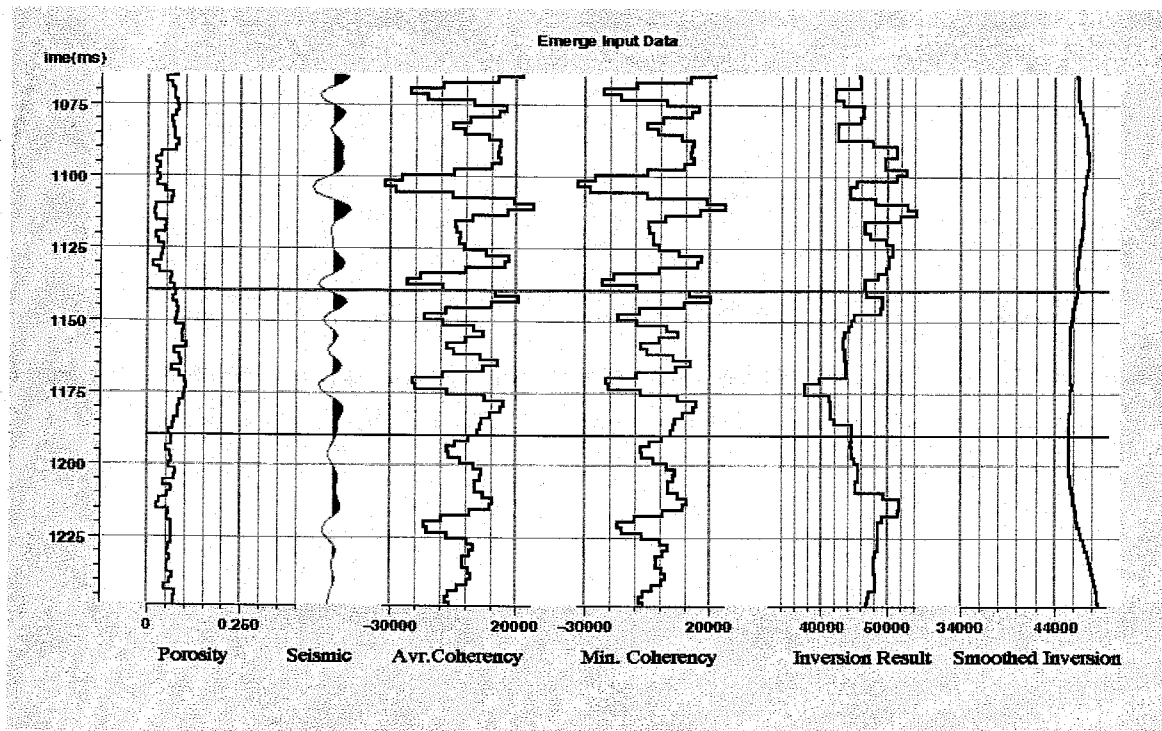
Figure 5.9: An example of the attribute curves extracted at one of the well locations and the target porosity log (red). The vertical axis is two-way travel (ms), and the magenta bars indicate the analysis window.
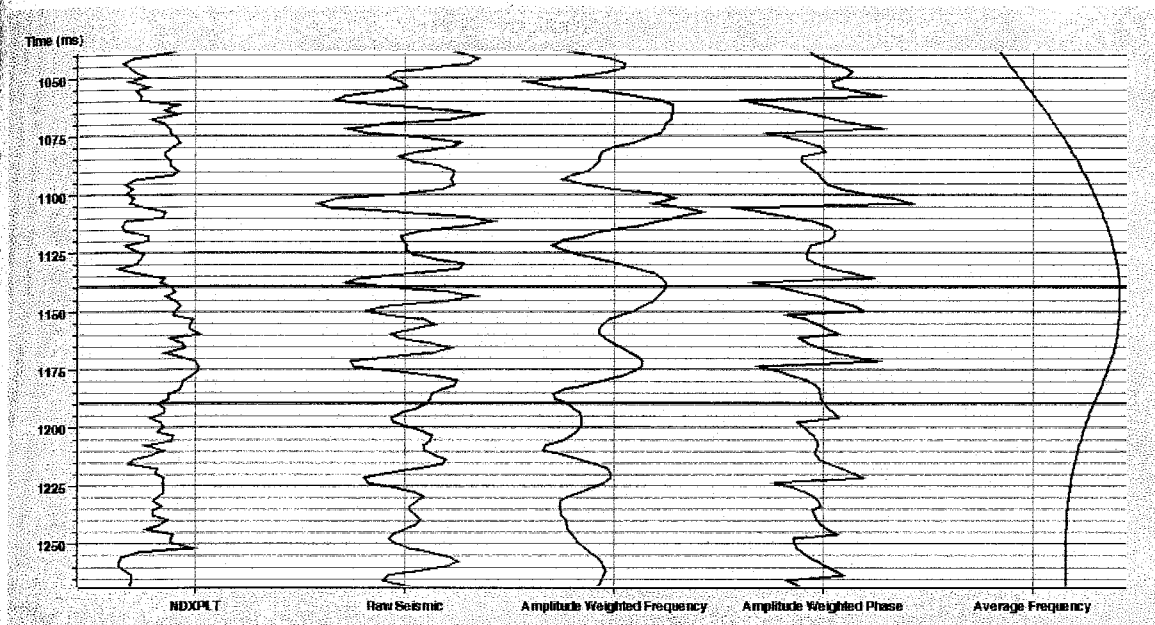
Figure 5.10: Additional attribute curves extracted from the same well location as in Figure 5.9. The magenta bars indicate the analysis window, and NDXPLT is the target porosity log. All curves increase to the right.

Table 5.2: Results of the multiattribute analysis: the best single predictor, the best pair, etc. and the associated RMS error of the prediction.

Number of Attributes	Attributes Used in Porosity Prediction	RMS Error
1	Amplitude-weighted frequency	0.0215
2	Amplitude-weighted frequency Average frequency	0.0181
3	Amplitude-weighted frequency Average frequency 1/smoothed impedance	0.0172
4	Amplitude-weighted frequency Average frequency 1/smoothed impedance minimum coherency^2	0.0160
5	Amplitude-weighted frequency Average frequency 1/smoothed impedance minimum coherency^2 Amplitude-weighted phase	0.0147
6	Amplitude-weighted frequency Average frequency 1/smoothed impedance minimum coherency^2 Amplitude-weighted phase Dominant frequency	0.0136
7	Amplitude-weighted frequency Average frequency 1/smoothed impedance minimum coherency^2 Amplitude-weighted phase Dominant frequency Integrated absolute amplitude	0.0127

The cross validation plot (Figure 5.11) shows a decrease in the average prediction error as the number of attributes increases until the sixth attribute is added. At this point, there is a large increase in the average prediction error from 1.5% at five attributes to 9% with six attributes, indicating that five is the optimal number of attributes to use. These five attributes are smoothed acoustic impedance, amplitude-weighted phase and frequency, average frequency, and minimum coherency. Although the decrease in error between one and five attributes is small, the five-attribute combination results in a substantial improvement in the prediction. This is illustrated graphically in the series of crossplots of predicted versus actual porosity shown in Figures A6-1 (Appendix 6) and 5.12 where each additional attribute included decreases the scatter about the y = x line. The predicted logs (Figures A6-2 through A6-5

and Figure 5.13) go from matching only the gross features of the target logs to matching the majority of the high frequency porosity changes as the number of attributes increases to five.

The set of convolutional weights for the five attributes determined by the generalized linear regression procedure and the transforms applied to the attributes are given in Table 5.3. As both the crossplot (Figure 5.12) and predicted logs (Figure 5.13) show, this predictor does a very good job of modeling the porosity curves with the exception of a slight under prediction in high porosity (>10%) zones.

Before using the derived attribute-porosity relationship found to create a porosity volume, an error analysis was done to determine the contribution of each well to the prediction and to ensure that no one well was causing excessive error. To this end, each well was excluded one at a time and predicted using the five remaining wells. The improvement in the prediction error produced by including a particular well in the analysis is shown in Figure 5.14. Although the improvements in the prediction error vary, it is clear that each well adds to the analysis, and no one well is degrading the result.
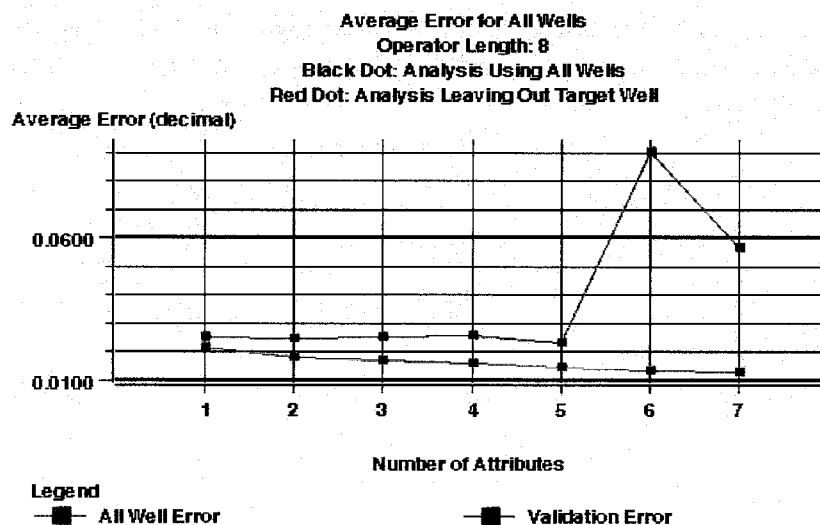
Figure 5.11: Average prediction error determined by exclusion testing versus the number of attributes. Note the jump from 1.5% error to 9% error between five and six attributes. This indicates that five is the maximum number of attributes that should be used.
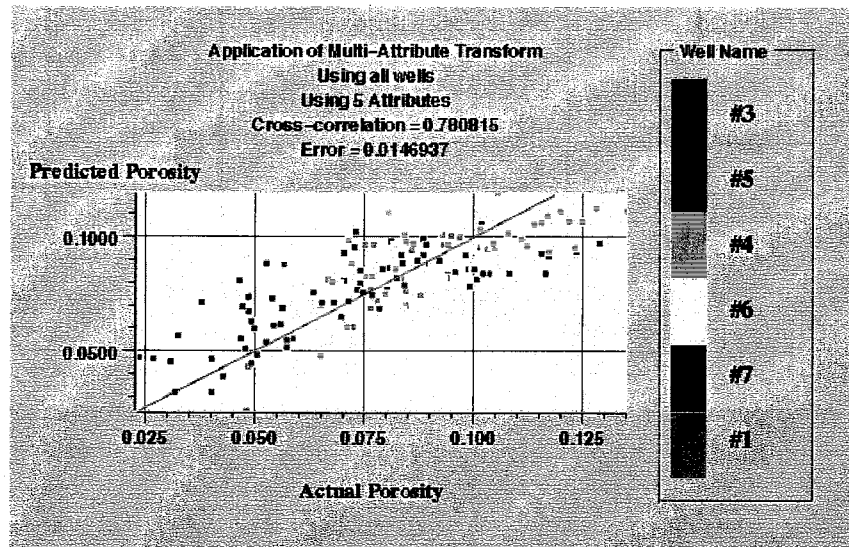
Figure 5.12: Porosity predicted using five seismic attributes versus actual porosity. The magenta line is the y =x line. The correlation coefficient and mean squared error for the prediction are 0.78 and 1.5%, respectively. Note that scatter about the y =x line is not the result of any one individual well, but a combination of data points from all wells.
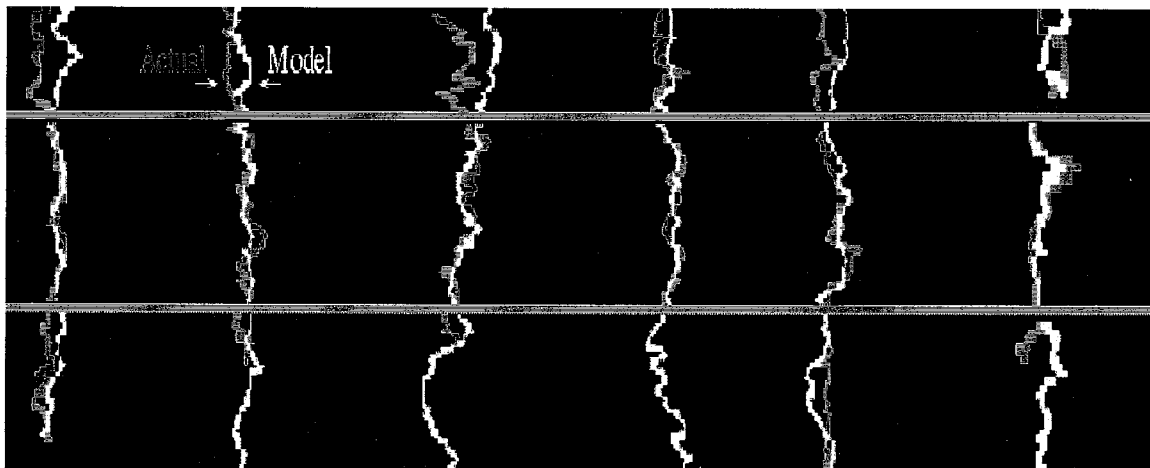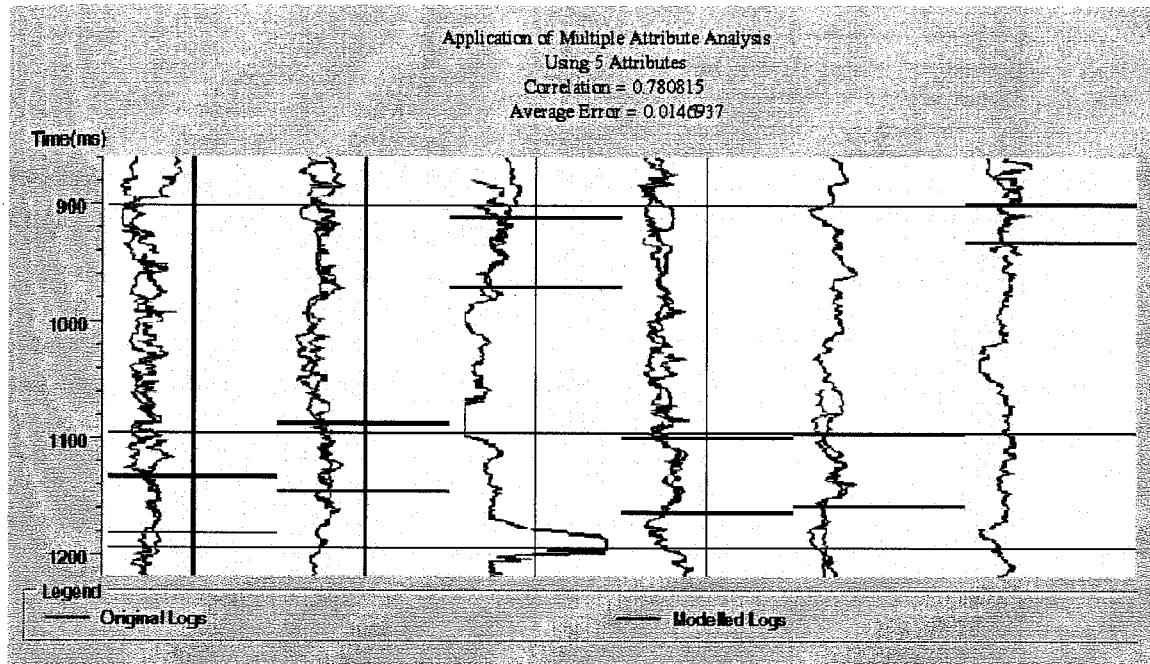
Figure 5.13: A qualitative comparison of the modeled porosity logs and the original porosity logs. The modeled logs were created using the five attribute porosity predictor. Upper: view showing the location and width of the analysis window in two-way travel time. The analysis window is indicated by heavy black lines, and porosity increases to the right. Lower: The analysis windows have been rescaled so that they are displayed at equal width (for display purposes only). Porosity again increases to the right, and the analysis window is indicated by the turquoise lines.

Attribute	Attribute Transform	Convolutional Weights
Amplitude-weighted frequency	None	1
Amplitude-weighted frequency	None	1
Amplitude-weighted frequency	None	1
Amplitude-weighted frequency	None	1
Amplitude-weighted frequency	None	1
Amplitude-weighted frequency	None	1
Amplitude-weighted frequency	None	1
Amplitude-weighted frequency	None	1
Average frequency	None	-0.7709
Average frequency	None	-0.6460
Average frequency	None	1.2701
Average frequency	None	2.2916
Average frequency	None	-1.7575
Average frequency	None	-1.1058
Average frequency	None	1.2651
Average frequency	None	-0.5453
Smoothed impedance	$1/x$	55377.8477
Smoothed impedance	$1/x$	-89423.1406
Smoothed impedance	$1/x$	136973.5156
Smoothed impedance	$1/x$	-136580.4375
Smoothed impedance	$1/x$	198193.2969
Smoothed impedance	$1/x$	-297458.3125
Smoothed impedance	$1/x$	274918.5312
Smoothed impedance	$1/x$	-140648.2188
Minimum coherence	x^2	1
Minimum coherence	x^2	1
Minimum coherence	x^2	1
Minimum coherence	x^2	1
Minimum coherence	x^2	1
Minimum coherence	x^2	1
Minimum coherence	x^2	1
Minimum coherence	x^2	1
Amplitude-weighted phase	None	1
Amplitude-weighted phase	None	1
Amplitude-weighted phase	None	1
Amplitude-weighted phase	None	1
Amplitude-weighted phase	None	1
Amplitude-weighted phase	None	1
Amplitude-weighted phase	None	1
Amplitude-weighted phase	None	1
Constant	-------	0.0116

Table 5.3: Transforms and convolutional weights determined for the five seismic attributes used in the best porosity predictor.

Although it is simple to apply the relationship and create the porosity volume, it is significantly more difficult to find meaningful ways in which to display the data. The volume-based attribute analysis is a very new technique, and a result, there are no standard type of displays for the resulting physical property volumes. Because the displays are unfamiliar, and in some cases nonintuitive, it is worthwhile to briefly explain the displays that will be used to present the results in the following section, the porosity distribution of the Second Sand. Three methods will be used to illustrate the results of the porosity volume analysis: (1) 2-D transects through the volume. These are essentially variable area seismic wiggle trace displays where the wiggles have been replaced by porosity logs, and the porosity logs are "filled" with a gradational color scheme proportional to the magnitude of the
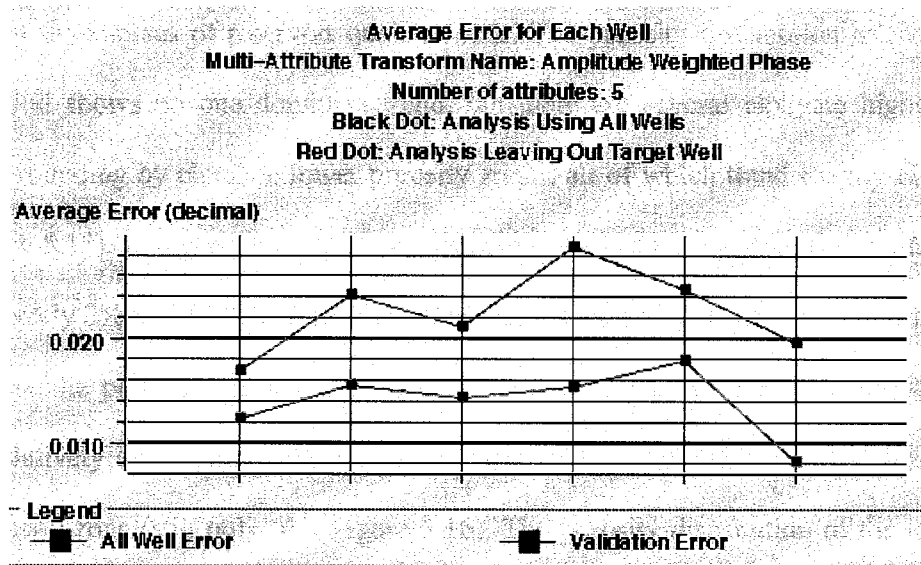
Figure 5.14: Average prediction error versus the well used. This shows the effect each well has on the prediction. The position on the x axis indicates the well being considered (the data points from left to right on the x axis are in the same order as the wells shown in Figure 5.13). The red data points indicate the prediction error for that well when it is excluded from the analysis, and the black data points give the prediction error at that well when all wells are used in the analysis. The vertical distance between the red and black points is, therefore, a measure of how much each well contributes to the analysis.

porosity. Although these plots are somewhat busy, the fill is necessary to emphasize small variations in the porosity logs that would otherwise be difficult to see from the logs alone; (2) map views of average attributes extracted along various horizons in the data. The attribute maps that will be considered are amplitude and amplitude thickness. The former are simply average porosity maps, and the latter are essentially net pay maps measured in time rather than feet; (3) maps of net pay, the number of vertical feet where the porosity is above a cutoff value. Using these techniques, the predicted porosity distribution of the early, middle, and late periods in the Second Sand depositional history will

5.2.4 Porosity distribution of the Second Sand

Early period porosity distribution: The average porosity determined for each of the lobes of the early period (Figures 5.15 to 5.17) confirms that the early period sediments do not contain significant thicknesses of reservoir quality sands. The porosity distribution of lobe 1 of the early period shows no one dominant trend, but there are several elongate higher porosity zones surrounding by elongate lower porosity zones, all of which trend roughy N-S to NW-SE (Figure 5.15). However, these porosity variations are quite small (porosity varies between approximately 2% to 7.5%), and the highest porosity zone occurs near the southern end of the lobe where the porosity reaches a maximum value of 11%. Lobe 2, in contrast, shows a single, relatively clear trend of decreasing porosity to the east and west away from an axial high-porosity zone (still only 9%; Figure 5.16). The porosity distribution of the largest lobe of the early period, lobe 3, is considerably more complicated. The porosity ranges from approximately 2% to 12%, and the high and low porosity zones are arrayed in a more radial pattern than seen in the other two lobes (Figure 5.17).
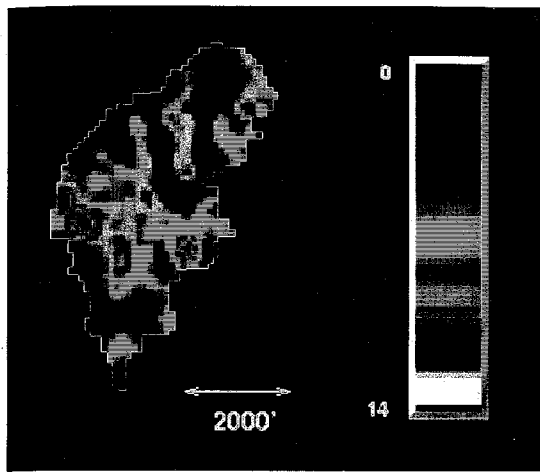
Figure 5.15: Map view of the average porosity of lobe 1 of the early period. The porosity is reported in percent (color key).
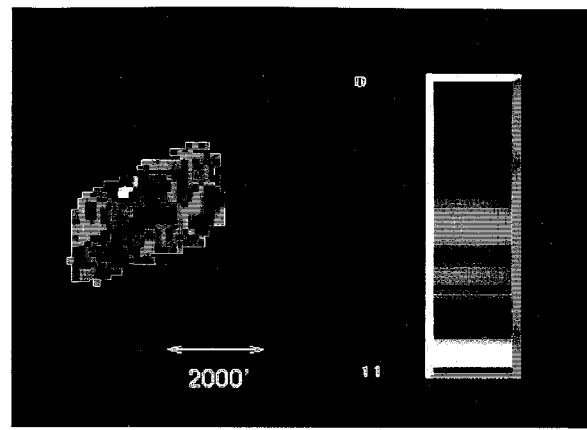
Figure 5.16: Map view of the average porosity of lobe 2 of the early period. The porosity decreases from a high of approximately 9% in the axial zone to less than 5% east and west of this zone.

Middle period porosity distribution: The average porosity of the middle period, the "C" sand, is shown in Figure 5.18. While, the porosity distribution appears somewhat random in the southern portion of the study area, the central region shows a NE-SW trending zone of higher porosity ranging from 12 to 13%. Also of note is the roughly linear, N-S trending zone of low porosity (0-1%) near the eastern boundary of the study area.

The amplitude thickness map of the "C" sand (Figure 5.19) shows that while the highest porosities occur in a NE-SW zone, the thickest (in ms) regions of porosity greater than 10% occur in three main zones or "porosity thicks": (1) a central zone, (2) an elongate, isolated porosity thick in the SW quarter of the study area, and (3) a porosity thick in the SE quadrant of the study area. In order to quantify the magnitude of these porosity thicks and to ensure that their prominence is not due to velocity variations, a map of net pay (ft) was created (Figure 5.20 and 5.21). These three zones are still the dominant features on the net pay map. The central zone is more clearly defined than in the amplitude thickness map, and it appears to be composed of two adjacent thick porosity zones. The southernmost portion of the central

porosity thick occurs at approximately the same location as the high porosity zone seen on

the average porosity map (Figure 5.18). The SE and SW porosity thicks, in contrast, are not

associated with such marked high porosity zones and instead have average porosity values of

approximately 11%.

Late period porosity distribution: As a whole, the "A" and "B" sands of the late period show

lower average porosities than the "C" sand. Due to the thickness of the unit, the average

porosity map of the late period show only a gross trend of increasing porosity to the SW with

some N-S trending porosity thicks in the SW and NE regions of the study area. Overall, the

porosity ranges from 0% to 13%. In the NE corner, the predicted porosity values were

negative and have been set to zero (black regions in Figure 5.22).
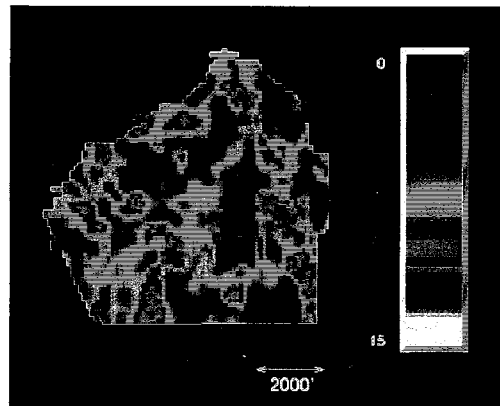
Figure 5.17: Average porosity of lobe 3 of the early period.

110
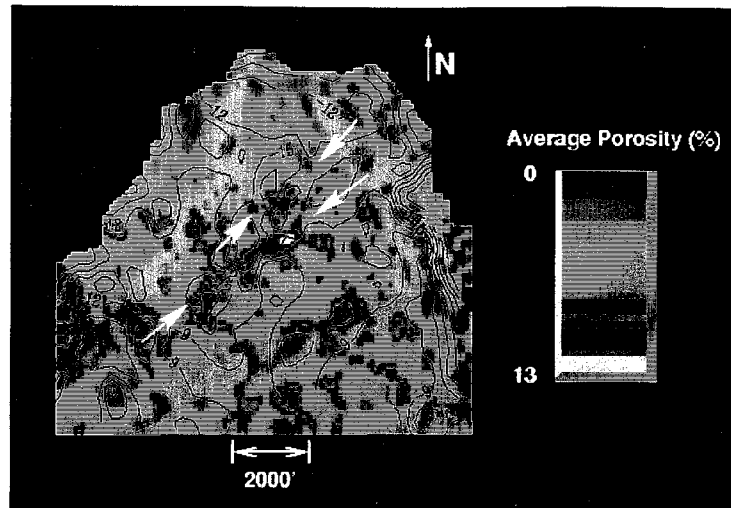
Figure 5.18: Map view of the average porosity of the "C" sand. The largest zone of high porosity (12-13%) trends NE-SW. The yellow arrows indicate the trend of the trough along the junction of lobes 1 and 2, and the white arrows show the trend of the trough created by the overlap of lobes 2 and 3 and continuing southwest along the margin of lobe 3 (beyond the termination of lobe 2). The overlain contours are the "C" sand isochron (ms).
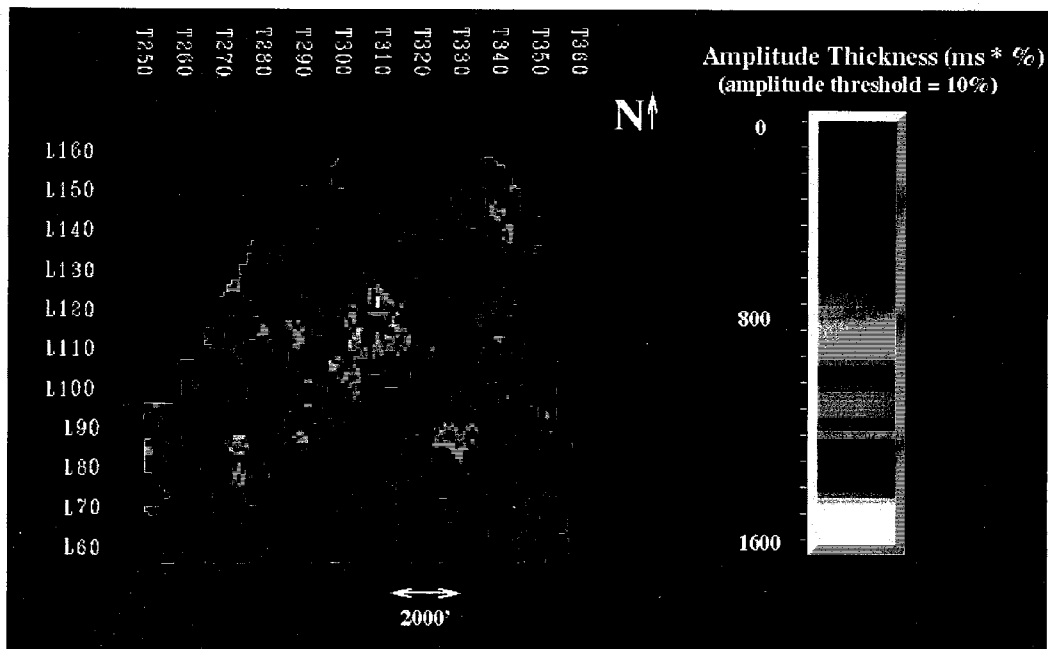
Figure 5.19: Map of the thickness (ms) of porosity greater than 10% within the "C" sand. The map is the result of extracting the percentage of amplitudes (porosities) greater than 10% within the "C" sand and multiplying the result by the isopach map of the "C" sand (hence the units of 100 times the travel time).

111
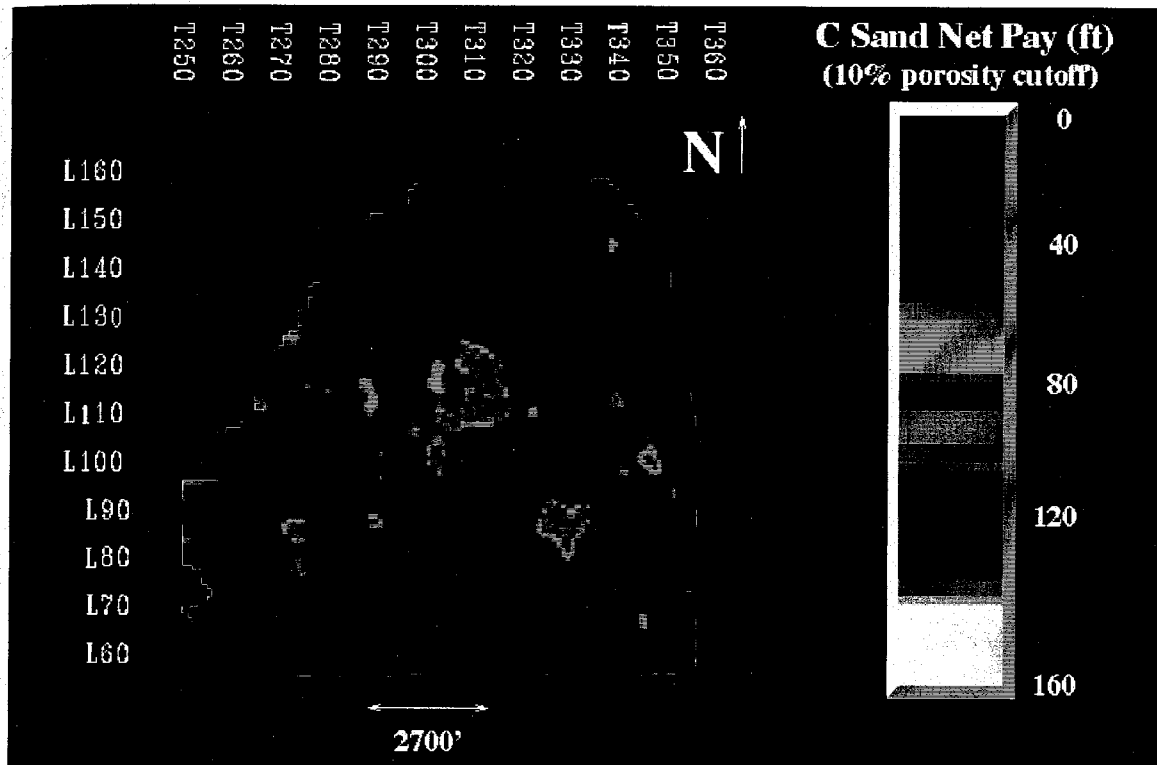
Figure 5.20: Net pay map of the "C" sand using a 10% porosity cutoff. The thickest regions of net pay occur in three zones: (1) a large, elongate central zone with net pay values up to 120', (2) a smaller, more equant porosity thick in the SE with net pay thicknesses slightly below 120', and (3) a small, elongate, N-S trending porosity thick in the SW quadrant of the study area. The cutoff porosity was set at 10% because this is the minimum porosity necessary for a well to be considered economical in this field.
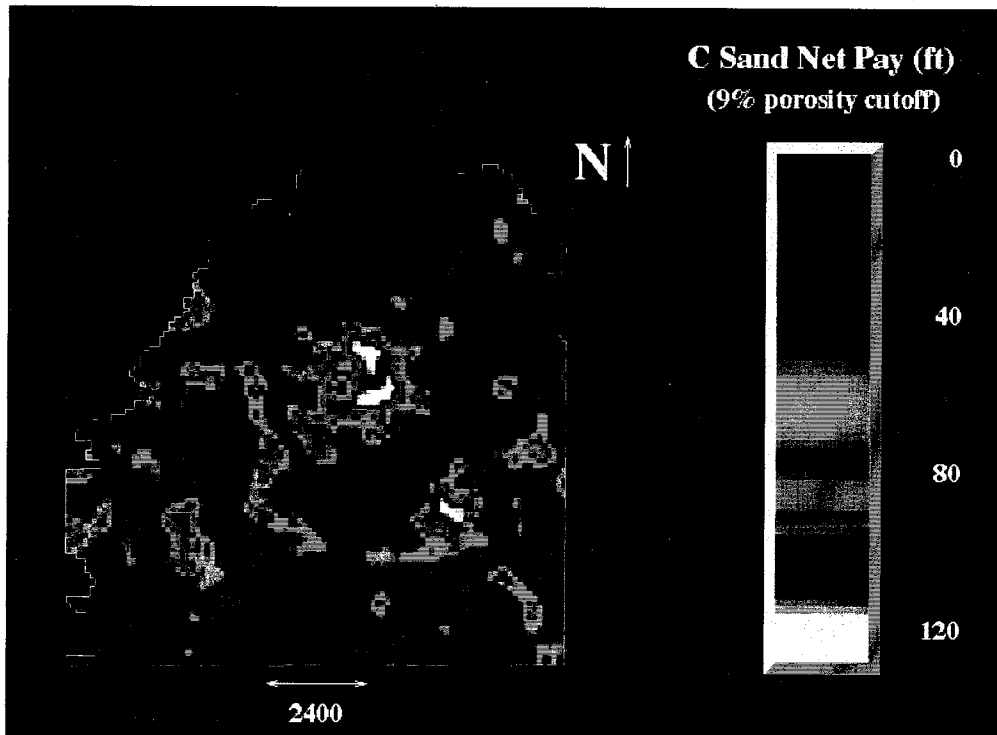
Figure 5.21: Net pay within the "C" sand calculated using a 9% porosity cutoff to compensate for the slight under-prediction of porosities greater than 10% seen in the crossplot (Figure 5.12).
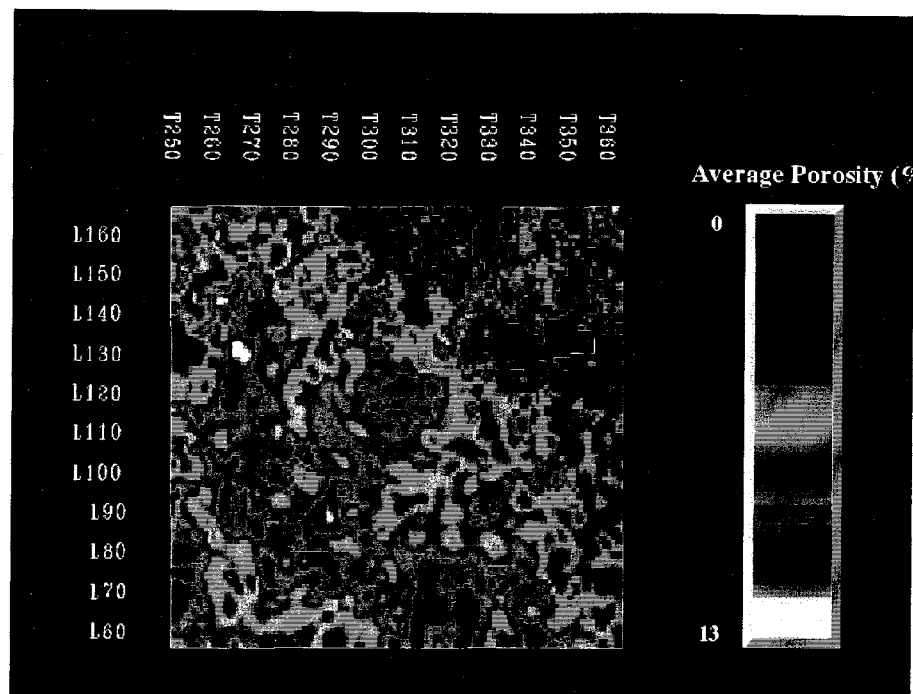
Figure 5.22: Average porosity the late period ("A" and "B" sands). Note the overall increase in porosity to the southwest and the elongate porosity thicks in the northwest and south central portions of the study area.

5.3 Discussion

Because the "C" sand is the only productive reservoir, the majority of the discussion will be focused on possible drilling targets within the "C" sand, and the early and late periods will only be briefly addressed.

5.3.1 Early period

The predicted porosities of the early period are low overall, conforming well to what is known of these rocks from well logs. Each of the three lobes has a markedly different porosity distribution. If porosity is assumed be a function of lithology (i.e., if it is related to the primary depositional facies and higher porosities are indicative of sandier sediments) the N-S trends in lobe 1 would appear to support a N-S sediment transport direction where sandier sediments are concentrated along the axes of flows. The highest porosity zones near

the end of lobe 1 could be the result of sand transport to the outer regions of the lobe by efficient (muddy) turbidity currents, but given the available data, and the ambiguity of the trends, this is highly speculative and subject to interpretation. The pattern seen in the porosity distribution of lobe 2, which was interpretted as being sandier than lobe 1, could be the result of higher porosity sands being deposited along the axis of the lobe in a channel system that is below the resolution of the seismic data. Lobe 3 does not have an easily explained porosity distribution. While it could be said that the high and low porosity zones are arrayed somewhat radially and could reflect distributary channels, there is insufficient data to support or refute this hypothesis.

5.3.2 Middle period

The results of the porosity analysis indicate that three potential drilling targets exist within the "C" sand (the central, SE, and SW porosity thicks). Each of these has been assigned a risk level based on the strengths of the geostatistical results, the geology of area, and the production history. The estimated risk and the potential net pay for each of the targets are summarized in Table 5.4 below.

Drilling Target	Associated Risk	Potential Net Pay 9% porosity cutoff / 10% porosity cutoff
Central porosity thick	low-moderate	134 / 118
SE porosity thick	moderate-high	123 / 108
SW porosity thick	very high	110 / 93

Table 5.4: Estimate of drilling risk and potential net pay for identified drilling targets within the "C" sand.

Central porosity thick: As a drilling target, the central porosity thick has the least associated risk and greatest potential net pay, in terms of both area and total thickness. In terms of the

geostatical results, this area is considered low risk because of its proximity to the control wells used in the geostatistical analysis which increases the probability of the well data set being representative of the area. Furthermore, the size of the porosity thick and the good quality of the seismic data in this region argue against it being the result of spurious noise in the porosity volume. This low risk assessment is also validated by the geology. The locations of the highest porosity zones within the central porosity thick occur within the small troughs formed at the junctions of the underlying lobes of the early period (indicated by the arrows in Figure 5.18 and seen in cross-section in Figure 5.23). This same region appears on the net pay map as a broad, porosity thick with a more N-S orientation. This makes sense in light of the geologic history interpreted for the "C" sand. In the earliest period of "C" sand deposition, channels may have formed in the troughs, concentrating the highest porosity sands within these depressions. After the filling of these depressions, channels would have been likely to migrate more rapidly (as would be expected in a shale-poor fan), become broader, and take on a more north-south orientation in keeping with the primary sediment transport direction. The vertical and lateral facies variations associated with this migration could explain the slightly lower average porosity over the rest of the central porosity thick as compared to the regions within the earlier confined channels (Figures 5.18 and 5.23).

Although the average porosity map does not show clear elongate trends that might be expected if channels formed in the depressions above lobe junctions, this does not necessary invalidate the interpretation because there are additional complicating factors, for example: (1) the porosity variations are small, and some thin, high porosity zones may not be apparent on a map of average porosity; (2) varying degrees of cementation and dissolution may have altered the primary porosity distribution, (3) relatively high porosities can occur in other facies as well, and (4) there is inevitably some error in the porosity prediction. However, an alternative interpretation is that the troughs may simply have been topographic lows that

filled with sand as turbidity currents travelling in other directions (i.e. not NE-SW along the trough axes) encountered the change in gradient and deposited part of their sediment load. Regardless of whether or not confined channels formed in these features, the majority of the thickness of the net pay occurs in the zone above and around these features. Thus, while the troughs contain the highest porosity rocks, it was the continued deposition in this broad channel fairway (constrained by core data) below the central re-entrant that resulted in the greatest accumulation of sediments with porosities above 9-10%.
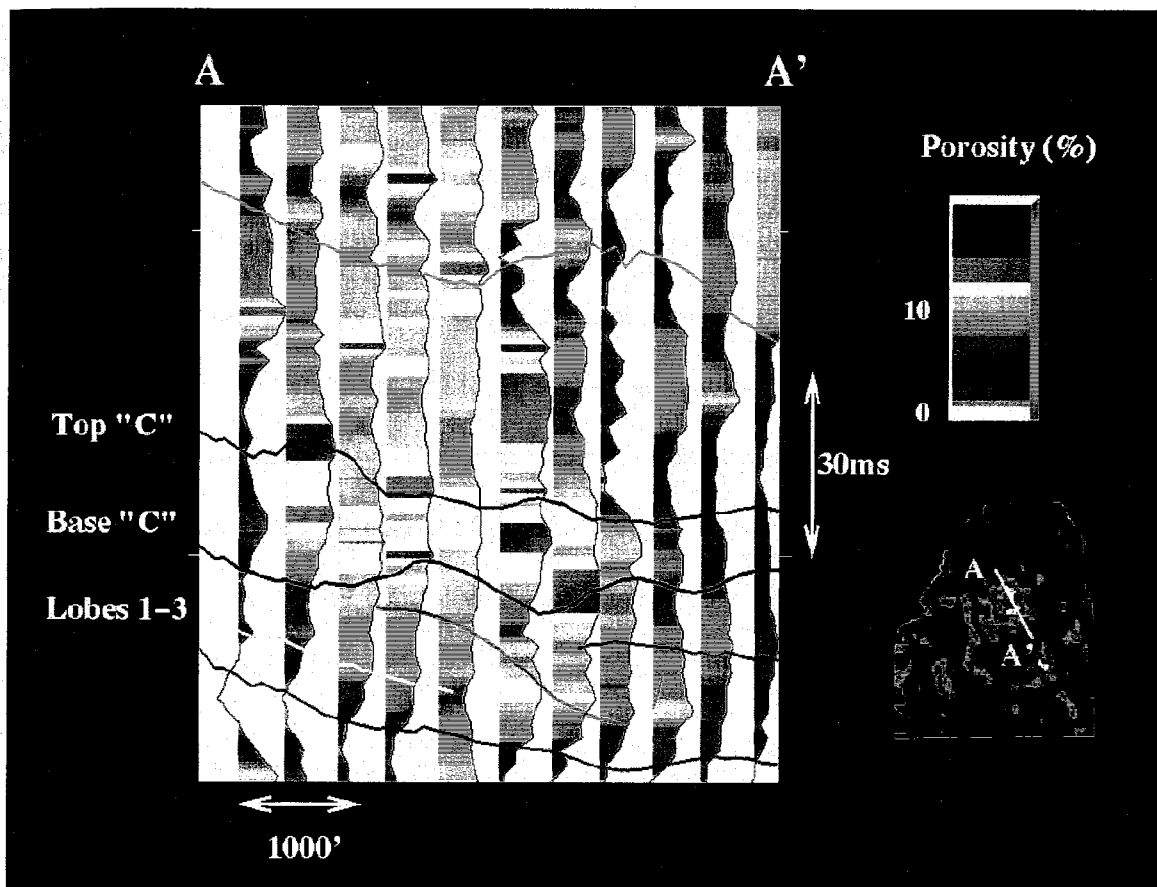
Figure 5.23: Cross-section through the porosity volume showing the central porosity thick. The cross-section location is given on the small net pay reference map in the lower right corner. The black curves are the predicted porosity logs, and the curves have been color filled according the magnitude of the porosity (from 0 to 20%). The highest porosity zone (~14-15%) occurs within the trough between lobe 2 (gray) and lobe 3 (magenta).

The low to moderate risk factor is also based the central porosity thick's location within the established productive trend of the "C" sand in this field. Although the comingled nature of the production data makes it difficult to assess the productivity of the "C" sand alone, the central porosity thick is within the most productive area of the field (Figure 2.4).

Southeast porosity thick: The southeast porosity thick is assigned a moderate to high drilling risk. Like the central porosity thick, the SE porosity thick is adjacent to one of the control wells used in the multiattribute analysis (Figure 5.5), and the porosity data in this region is of good quality (i.e. there are no spikes or unrealistic or negative porosity values). The result also appears to be geologically reasonable. Cross-sectional views through the porosity volume (Figure 5.24) show that the SE porosity thick has an average porosity of approximately 11% with a narrow, central zone of higher porosities (a maximum of 14%). The location of this porosity thick within a slight depression along the top of lobe 3 of the early period, and the axial zone of higher porosities may indicate an origin similar to that of the central porosity thick. The risk associated with this porosity thick is primarily due to its location in the undrilled SE corner of the study away from the main productive trend. With the exception of the nearby control well used in the attribute analysis, the potential of this region is largely untested.

Southwest porosity thick: The smallest of targets, the SW porosity thick, has the greatest associated risk. In E-W cross-sections through the porosity thick (Figure 5.25), it is clear that the high porosities seen here are due chiefly to a few porosity logs with consistently high values within and above the "C" sand. Adjacent porosity logs have substantially lower porosities, making the change to high porosity in the neighboring logs extremely abrupt in both the N-S and E-W directions. Also of note is the fact that high-porosity zone is situated

on a topographic high. Given the abruptness of the change to high porosities, the large

vertical extent of the high porosity zone, the relatively high S/N ratio in this area, and the

position on a topographic high, these data are believed to be spurious. Although this porosity

thick has not been drilled, it is surrounded by dry holes (in terms of the Second Sand).

Consequently, the SW porosity thick has been assigned a very high risk factor despite

predicted values of net pay greater than 100'.

Based on the above discussion, it appears that the main control on the porosity

distribution of the Second Sand is primary depositional facies. However, an examination of

the low porosity trends within the "C" sand indicates that this may not be the only controlling

factor. The zones of low porosity within the "C" sand tend to be more common in faulted
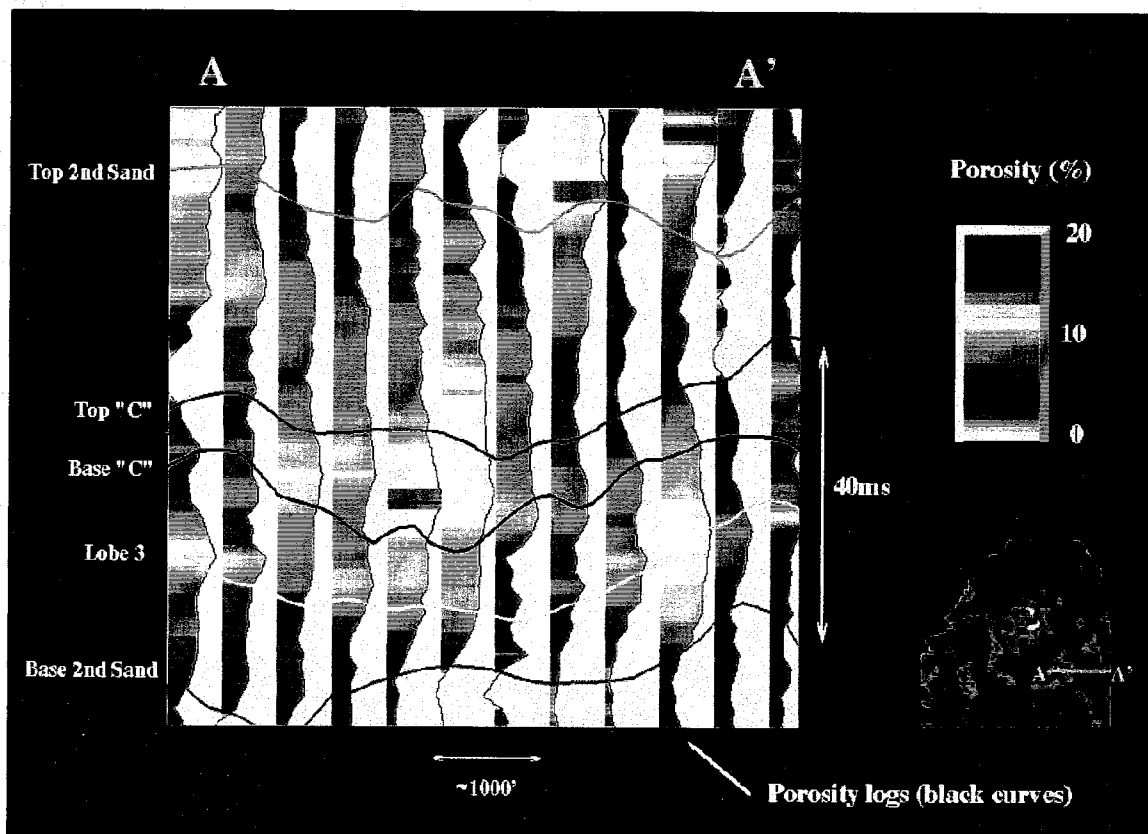
Figure 5.24: Porosity cross-section through the SE porosity thick. The curves and color scale are the same as in Figure 5.23. The high porosity zone (12-14.5%) associated with this porosity thick is confined to a narrow region within a depression in the upper surface of lobe 3.

areas (the inverted "U" of underlying faults described in Chapter 4). This tendency is most pronounced along the boundary of the eastern ridge where the most extreme low-porosity zone within the "C" sand follows the trace of the N-S trending reverse fault that cuts the Second Sand (Figure 5.26). Porosity rapidly returns to more "normal" values away from the fault zone.

The faults seen at the Second Sand level do not intersect the wellbores, so their effect on the porosity distribution could not be explicitly modeled by the well data set. It is possible, however, that this effect was indirectly represented by the easternmost well used in the attribute analysis which is in close proximity to the N-S trending reverse fault. In light of
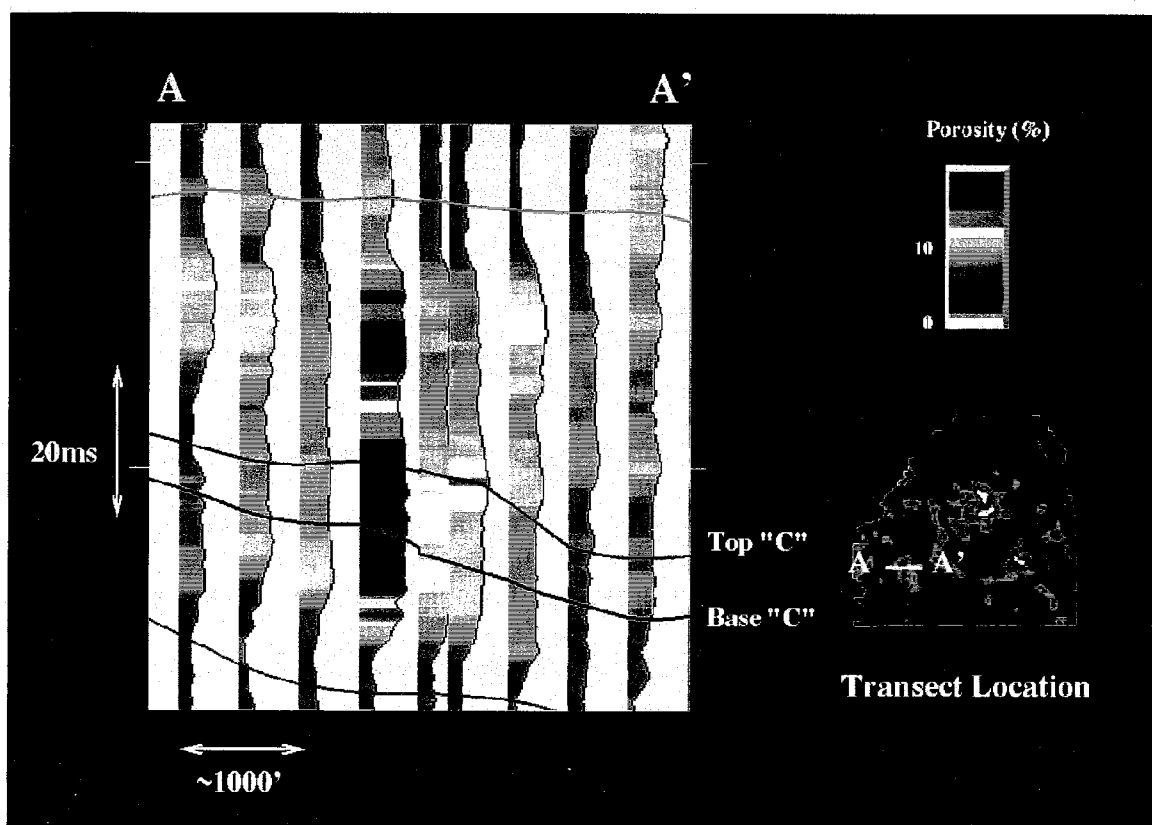
Figure 5.25: An E-W cross-section through the SW porosity thick. A description of the curves and color used is given in Figure 5.23. The SW porosity is caused in large part by a few predicted porosity logs with anomalous high values. These data are believed to be spurious due, perhaps, to the poorer quality seismic data in this area.
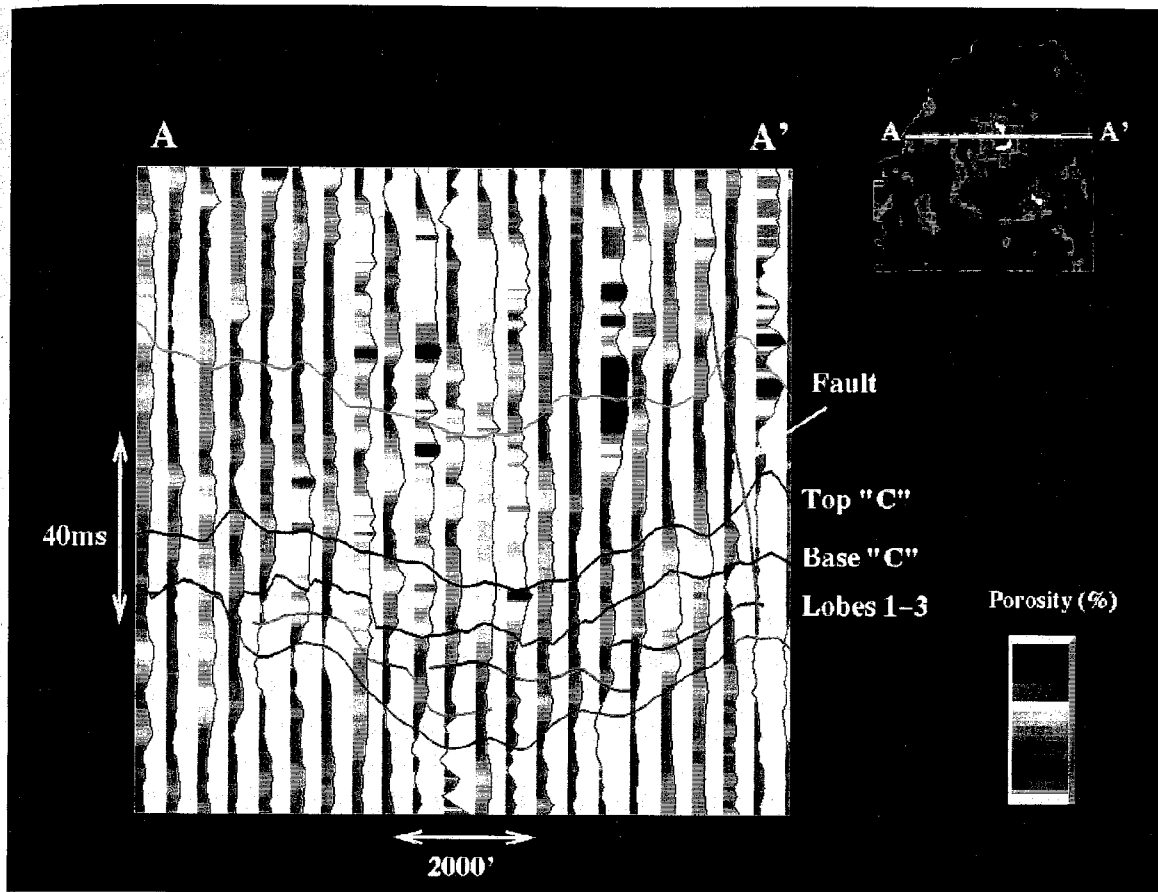
Figure 5.26: A W-E cross section through the porosity volume illustrating the porosity prediction near a reverse fault at the Second Sand level. A sharp drop in the predicted porosity can been seen in logs adjacent to and crossing the fault. Porosity is colored as in Figure 5.23.

these observations, it is possible that sealing faults and fractures may play a previously unrecognized role in the porosity distribution in this region. Although secondary porosity has not observed in cores in this field, it dominates at other locations along the slope (Saller et al., 1989; Gawloski, 1987), suggesting that secondary porosity may exist here as well. Further study is needed to determine the full extent of the effect of faults and fractures on fluid flow in the study area.

5.3.3 Late period

Due to the combined thickness of the "A" and "B" sands, it is difficult to draw many conclusions about the porosity distribution from the average porosity map. Cross-sectional views through the porosity volume indicate that in general, the porosity is lower on average than in the "C" sand, and the high porosity zones that do occur tend to be relatively thin and sporadic (Figures 5.23-5.26).

5.4 Conclusions

The volume-based attribute analysis has produced a porosity model that is both statistically robust and geologically reasonable. Within the Second Sand, the porosity distribution appears to be controlled by a combination of primary depostional facies and the distribution of faults and possibly associated fractures. High porosity zones tend to be elongate features associated with paleotopographic depressions. Such features would favor the formation of confined channels with a greater porportion of relatively clean, high porosity sands. In contrast, low porosity zones are more abundant in faulted areas, possibly indicating that fault-related fluid flow caused localized cementation.

Three potential drilling targets within the "C" sand have been identified, two of which are considered viable. Of these, the centrally located porosity zone has the greatest potential and least risk. At present, two wells have been drilled on the margins of this zone, but none have penetrated the center of the porosity thick where the highest values of net pay are predicted. The second drilling target is located in the southeastern quadrant of the study area. While the net pay estimated for this porosity thick is substantial, its location in an untested region of the field, away from the main productive trend, gives this target a moderate to high risk factor.

6. Conclusions and Broader Implications

Based on an integrated analysis of well logs, core data, production information, and seismic data, the Second Sand Member of the Bone Spring Formation forms a lowstand systems tract that consists of a basin-floor fan, a slope fan, and a modified prograding wedge. The elements of the lowstand systems tract differ from standard sequence stratigraphic models in that they have an overall "channel-shape" rather than mounded cross-sectional geometry; the best quality reservoir rocks occur within the slope fan; and the stratigraphically highest element is a modified prograding wedge. These differences are attributed to 1) the structure of the underlying units which give this intraslope basin an in an inverted "U" shaped with the greatest accumulations of sediment occurring between the fault-bounded ridges that make up the arms of the "U", 2) variations in the availability of siliciclastic sediment supply, most notably the lack of a siliciclastic sediment source during the deposition of the basin-floor fan, and 3) a late stage relative sea level fall that caused the depocenter to shift downslope resulting in progressive bypassing of the slope and deposition of a series of "shingles" that prograde out into the basin and possibly contain a greater proportion of debris flow deposits.

Using a volume-based approach and a rigorous technique to tie the well data to the seismic data, it was possible to successfully predict the porosity distribution of the Second Sand using a combination of five seismic attributes. The relationships between each of these attributes and porosity has a physical basis, and the resulting porosity prediction has a complex, but geologically plausible, relationship to the results of the geologic analysis. The porosity distribution is controlled by a combination of primary depositional facies and the distribution and faults and possibly associated fractures which

tend to be associated with zones of extreme low porosity. Within the slope fan, the highest porosities occur within small, trough-shaped paleobathymetric low that mark the junctions between adjacent lobes of the underlying basin-floor fan, and the greatest accumulations of net pay occur in a broad zone within and above these features. This region is directly downslope from a prominent re-entrant in the upper slope which appears to have acted as a conduit for sediment gravity flows during the deposition of the Second Sand. Based on the seismic, well, and core data, this region of high net pay is believed to have been a channel fairway and is the best target for infill drilling within the field.

These results have application beyond the current study area. In particular this study shows that (1) an integrated analysis of the geologic and geophysical data can be used as a means to validate and test attribute-based predictions of reservoir properties, (2) a volume-based approach can be used to successfully predict small variations in reservoir properties even if the reservoir is a thick and stratigraphically complex unit or if traditional horizon- or interval-based approaches have failed, and (3) if a rigorous approach is used in the well-tying procedure, volume-based attribute analyses need not be limited to areas where checkshot data or vertical seismic profiles are available. Finally, the sequence stratigraphic model presented in this study can be used to guide exploration in the Bone Spring Formation and other submarine fan deposits in analogous areas, and the departures of this model from the well known "slug" model illustrate the need to consider the interplay of all factors affecting deposition in the slope environment, particularly sediment availability and paleobathymetry or basin configuration, in addition to changes in relative sea level.

References

Adcock, S., 1993, In search of the well tie: what if I don't have a sonic log?: The Leading Edge, v. 12, p. 1161-1164.

Ausburn, B. E., and J. R. Butler, 1977, Well log editing in support of detailed seismic studies: Transactions of the Society of Professional Well Log Analysists Annual Logging Symposium, p. F.1-F.38.

Bahorich, M., and S. Farmer, 1995, The coherence cube: The Leading Edge, v. 10, p. 1053-1058.

Barnes, A. E., 1998, The complex trace made simple: The Leading Edge, v. 17, p. 473-476.

Brenner, R. L., and T. R. McHargue, 1988, Integrative Stratigraphy: Concepts and Applications: London, Prentiss-Hall, 419 p.

Brown, A. R., 1996a, Interpretation of Three-Dimensional Seismic Data, 4th ed.: American Association of Petroleum Geologists Memoir 42, 424 p.

Brown, A. R., 1996b, Seismic attributes and their classification: The Leading Edge, v. 15, p. 1090.

Corbett, C., Plato, J. S., and G. F. Chalupsky, 1995, Improved reservoir characterization by the application of multi-well petrophysical interpretation to seismic-guided log property distribution: Paper presented at the Field Study Petrophysics Forum sponsored by the Houston Chapter of the SPWLA on 7 June, 1995, p. 1-4.

Dalley, R. M., Gevers, E. C. A., Stampfli, G. M., Davies, D. J., Gastaldi, C. N., Ruijtenberg, P. A., and G. J. O. Vermeer, 1989, Dip and azimuth displays for 3D seismic interpretation: First Break, v. 7, p. 86-95.

Davies, G. R., 1997a, Aeolian sedimentation and bypass, Triassic of western Canada: Bulletin of Canadian Petroleum Geology, v. 45, p. 624-642.

--------, 1997b, The Triassic of the Western Canada Sedimentary Basin: tectonic and stratigraphic framework, paleogeography, paleoclimate, and biota: Bulletin of Canadian Petroleum Geology, v. 45, p. 434-460.

Doveton, J. H., 1994, Geologic Log Interpretation: Society of Economic Paleontologists and Mineralogists Short Course No. 29, 169 p.

Dubiel, R. F., 1994, Triassic deposystems, paleogeography and paleoclimate of the western interior *in* Caputo *et al.*, eds., Mesozoic Systems of the Rocky Mountain Region, U.S.A.: Denver, Rocky Mountain Section, Society for Sedimentary Geology.

Frenzel, H. N., Bloomer, R. R., Cline, R. B., Cys, J. M, Galley, J. E., Hills, J. M., King, W. E., Seager, W. R., Kottlowski, F. E., Thompson III, S., Luff, G. C., Pearson, B. T., and D. C. Van Siclen, 1988, The Permian Basin region *in* Sloss, L. L., ed., Sedimentary Cover—North American Craton: The Geology of North America, v. D-2: Boulder, Geological Society of America, p. 261-306.

Galloway, W. E., 1998a, Siliciclastic slope and base-of-slope depositional systems: component facies, stratigraphic architecture, and classification: American Association of Petroleum Geologists Bulletin, v. 82, p. 569-595.

-----------, 1998b, Clastic depositional systems and sequences: Applications to reservoir prediction, delineation, and characterization: The Leading Edge, v. 17, p. 173-180.

Gastaldi, C., Biguenet, J., and L. de Pazzis, 1997, Reservoir characterization from seismic attributes: an example from the Peciko Field (Indonesia): The Leading Edge, v. 16, p. 263-266.

Gawloski, T. F., 1987, Nature, distribution, and petroleum potential of Bone Spring detrital sediments along the Northwest Shelf of the Delaware Basin *in* Cromwell, D., and Mazullo, L. J., eds., The Leonardian Facies in W. Texas and S.E. New Mexico and

Guidebook to the Glass Mountains: Society of Economic Paleontologists and Mineralogists, Permian Basin Section Publication No. 87-27, p. 85-105.

Hampson, D., and M. Galbraith, 1994, Wavelet extraction by sonic log correlation *in* STRATA Users Guide: Hampson-Russell Software Services Limited, p. 24-42.

Hampson, D., and Russell, B., 1994, STRATA Theory *in* STRATA Users Guide: Hampson-Russell Software Services Limited, p. 1-44.

Hardage, R. A., Pendleton, V. M., Major, R. P., Asquith, G. B., Schultz-Ela, D., and D. E. Lancaster, 1998, Using petrophysics and cross-section balancing to interpret complex structure in a limited-quality 3-D seismic image *in* DeMis, W. D., and Nelis, M. K. eds., The Search Continues into the 21st Century: West Texas Geological Society Publication 98-105, p. 205-206.

Hart, B. S., 1997, New targets in the Bone Spring Formation, Permian Basin: Oil and Gas Journal, v. 95, p. 85-88.

Hirsche, W. K., Boerner, S., Kalkomey, C., and C. Gastaldi, 1998, Avoiding pitfalls in geostatistical reservoir characterization: a survival guide: The Leading Edge, v. 17, p. 493-504.

Howell, D. G., and W. R Normark, 1982, Sedimentology of submarine fans *in* Scholle, P.A., and Spearing, D., eds., Sandstone Depositional Environments: Tulsa, American Association of Petroleum Geologists, p. 365-404.

Kalkomey, C. T., 1997, Potential risks when using seismic attributes as predictors of reservoir properties: The Leading Edge, v. 16, p. 247-251.

Kocurek, G., and B. L. Kirkland, 1998, Getting to the source: aeolian influx to the Permian Delaware basin region: Sedimentary Geology, v. 117, p. 143-149.

MacPherson, B. A., 1978, Sedimentation and trapping mechanism in Upper Miocene Stevens and older turbidite fans of southeastern San Joaquin Valley, California: American Association of Petroleum Geologists Bulletin, v. 62, p. 2243-2274.

Marfurt, K. J., Kirlin, R. L., Farmer, S. L., and M. S. Bahorich, 1998, 3-D seismic attributes using a semblance-based coherency algorithm: Geophysics, v. 63, p. 1150-1165.

Marion, D., and D. Jizba, 1997, Acoustic properties of carbonate rocks: use in quantitative seismic measurements *in* Palaz, I., and Marfurt, K. J. eds., Carbonate Seismology, Geophysical Development Series, v. 6: Tulsa, Society of Exploration Geophysicists, p. 75-93.

Mazzullo, S. J., 1995, Permian stratigraphy and facies, Permian Basin (Texas-New Mexico) and adjoining areas in the midcontinent United States *in* Scholle, P. A., Peryt, T. M., and Ulmer-Scholle, D. S., eds., The Permian of Northern Pangea, v. 2: Berlin, Springer-Verlag, p. 41-60.

Messa, J. F., Brooks, L. L., Yates, S. M., and J. D. Underwood, 1996, Second Bone Spring Sand Study: Internal report, Harvey E. Yates Company, 55 p.

Mitchum, R. M., Jr., 1985, Seismic stratigraphic expression of submarine fans *in* Berg, O. R., and Wolvertons, D. G., eds., Seismic Stratigraphy II: American Association of Petroleum Geologists Memoir 39, p. 117-138.

Mitchum, R. M., Vail, P. R., and S. Thompson, 1977, The depositional sequence as a basic unit for stratigraphic analysis *in* Payton, C. E., ed., Seismic Stratigraphy—Applications in Hydrocarbon Analysis: American Association of Petroleum Geologists Memoir 26, p. 53-62.

Montgomery, S. L, 1997, Permian Bone Spring Formation: sandstone play in the Delaware Basin part I-slope: American Association of Petroleum Geologists Bulletin, v. 81, p. 1239-1258.

Peacock, K. L., and S. Treitel, 1969, Predictive deconvolution: theory and practice: Geophysics, v. 34, p. 155-169.

Pearson, R. A., and B. S. Hart, 1998, Stratigraphy and seismic-guided estimation of log properties of the Second Sand Member of the Bone Spring Formation, Delaware Basin, New Mexico *in* DeMis, W. D., and Nelis, M. K., eds., The Search Continues into the 21st Century: West Texas Geological Society Publication 98-105, p. 213-219.

Posamentier, H. W., and R. D. Erskine, 1991, Seismic expression and recognition criteria of ancient submarine fans *in* Weimer, P., and Link, M. H., eds., Seismic Facies and Sedimentary Processes of Submarine Fans and Turbidite Systems: New York, Springer-Verlag, p. 197-222.

Posamentier, H. W., Jervey, M. T., and P. R. Vail, 1988, Eustatic controls on clastic deposition I—conceptual framework *in* Wilgus, C. K., Hastings, B. S., Kendall, C. G. St. C., Posamentier, H. W., Ross, C. A., and Van Wagoner, J. C., eds., Sea-level Changes: An Integrated Approach: Society of Economic Paleontologists and Mineralogists Special Publication No. 42, p. 109-124.

Posamentier, H. W., and P. R. Vail, 1988, Eustatic controls on clastic deposition II—sequence and systems tracts tract models *in* Wilgus, C. K., Hastings, B. S., Kendall, C. G. St. C., Posamentier, H. W, Ross, C. A., and Van Wagoner, J. C., eds., Sea-level Changes: An Integrated Approach: Society of Economic Paleontologists and Mineralogists Special Publication No. 42, p. 125-154.

Raeuchle, S. K., Hamilton, D. S., and M. Uzcategui, 1997, Integrating 3-D seismic imaging and seismic attribute analysis with genetic stratigraphy; implications for infield reserve growth and field extension, Budare Field, Venezuela: Geophysics, v. 62, p. 1510-1523.

Rafipour, B. J., 1989, Seismic attributes give clue to reservoir saturation: World Oil, v. 208, p. 39-41.

Reading, H. G., ed., 1996, Sedimentary Environments: Processes, Facies, and Stratigraphy, 3rd ed.: Cambridge, Blackwell Science Ltd., 687 p.

Reading, H. G., and M. Richards, 1994, Turbidite systems in deep-water basin margins classified by grain size and feeder system: American Association of Petroleum Geologists Bulletin, v. 78, p. 792-822.

Risch, D. L., Chowdhury, A. N., Hannan, A. E., and G. A. Jamieson, 1994, How modern techniques improve seismic interpretation: World Oil (October), p. 85-90.

Russell, B., Hampson, D., Schuelke, J., and J. Quirein, 1997, Multiattribute seismic analysis: The Leading Edge, v. 16, p 1439-1443.

Saller, A. H., Barton, J. W., and R. E. Barton, 1989, Slope sedimentation associated with a vertically building shelf, Bone Spring Formation, Mescalero Escarpe field, southeastern New Mexico *in* Cromwell, D., and Mazzullo, L. J., eds., The Leonardian Facies in W. Texas and S.E. New Mexico and Guidebook to the Glass Mountains: Society of Economic Paleontologists and Mineralogists, Permian Basin Section Publication No. 87-27, p. 275-288.

Schuelke, J. S., Quirein, J. A., and J. F. Sarg, 1998, Reservoir architecture and porosity distribution, Pegasus Field, west Texas—an integrated sequence stratigraphic-seismic attribute study using neural networks: Annual Meeting Expanded Abstracts, American Association of Petroleum Geologists, v. 1998, p. 142-145.

Schultz, P. S., Ronen, S., Hattori, M., and C. Corbett, 1994, Seismic guided estimation of log properties, part 1: The Leading Edge, v. 13, p. 305-315.

Sheriff, R. E., and L. P. Geldart, 1995, Exploration Seismology, 2nd ed.: New York, Cambridge University Press, 592 p.

Silver, B. A., and R. G. Todd, 1969, Permian cyclic strata, northern Midland and Delaware basins, west Texas and southeastern New Mexico: American Association of Petroleum Geologists Bulletin, v. 53, p. 2223-2251.

Sloss, L. L., 1963, Sequences in the cratonic interior of North America: American Association of Petroleum Geologists Bulletin, v. 74, p. 93-114.

Stow, D. A. V., Reading, H. G., and J. D. Collinson, 1996, Deep Seas *in* Reading, H. G., ed., Sedimentary Environments: Processes, Facies, and Stratigraphy, 3rd ed.: Cambridge, Blackwell Sciences Ltd., p. 395-453.

Taner, M. T., Koehler, F., and R. E. Sheriff, 1979, Complex seismic trace analysis: Geophysics, v. 44, p. 1041-1063.

Taner, M. T., O'Doherty, R. F., and F. Koehler, 1995, Long period multiple suppression by predictive deconvolution in the *x-t* domain: Geophysical Prospecting, v. 43, p. 433-468.

Van Wagoner, J. C., Mitchum R. M., Campion, K. M., and V. D. Rahmanian, 1990, Siliciclastic Sequence Stratigraphy in Well Logs, Cores, and Outcrops: Concepts for High-Resolution Correlation of Time and Facies: American Association of Petroleum Geologists Methods in Exploration Series, No. 7, 54 p.

Van Wagoner, J. C., Posamentier, H. W., Mitchum, R. M., Jr., Vail, P. R., Sarg, J. F., Loutit, T. S., and J. Gardenbol, 1988, An overview of the fundamentals of sequence stratigraphy and key definitions *in* Wilgus, C. K., Hastings, B. S., Kendall, C. G. St. C., Posamentier, H. W., Ross, C. A., and Van Wagoner, J. C., eds., Sea-level Changes: An Integrated Approach: Society of Economic Paleontologists and Mineralogists Special Publication No. 42, p. 39-45.

Waters, K. H., 1987, Reflection Seismology, 3rd ed.: New York, John Wiley.

Watts, G. P., Hinterlong, G. D., and A. R. Taylor, 1997, Seismic description of a complex carbonate porosity system, Welch Field, Permian Basin, Texas: American Association of Petroleum Geologists Bulletin, v. 81, p. 870.

Weimer, P., and M. H. Link, 1991, Introduction: seismic facies and sedimentary processes of ancient submarine fans and turbidite systems *in* Weimer, P., and Link, M. H., eds., Seismic Facies and Sedimentary Processes of Submarine Fans and Turbidite Systems: New York, Springer-Verlag, p. 193-196.

Weimer, P., and H. W Posamentier, 1993, Recent developments and applications in siliciclastic sequence stratigraphy *in* Weimer, P., and Posamentier, H. W., eds., Siliciclastic Sequence Stratigraphy: Recent Developments and Applications: American Association of Petroleum Geologists Memoir 58, p. 3-12.

Wiggins, W. D., and P. M. Harris, 1983, Burial diagenetic sequence in deep-water allochthonous dolomites, Permian Bone Spring Formation, southeast New Mexico *in* Crevello, P. D. and Harris, P. M., eds., Deep-water Carbonates: buildups, turbidites, debris flows and chalks – a core workshop: Society of Economic Paleontologists and Mineralogists Core Workshop No. 6., p. 140-173.

Yilmaz, O., 1987, Seismic Data Processing: Tulsa, Society of Exploration Geophysicists, 526 p.

Ziolkowski, A., Underhill, J. R., and G. K. Johnston, 1998, Wavelets, well-ties, and the search for subtle stratigraphic traps: Geophysics, v. 63, p. 297-313.

Appendix 1: Geologic Interpretation of Seismic Data—Theory

Fundamentals of Reflection Seismology

In order to fully understand how reflection seismic data is exploited to determine the subsurface structure and stratigraphy, it is first necessary to understand the basic theory behind reflection seismology. The following summary is based on the works of Waters (1987), Yilmaz (1987), and Sheriff and Geldart (1995).

Reflection seismology deals with the use of artificially generated acoustic waves. As these compressional waves travel into the subsurface, they are reflected and refracted at acoustic impedance (the product of velocity and density) contrasts within the subsurface (Figure A1-1). Interfaces that could produce reflections include boundaries between different lithologies, fault surfaces (with acoustic impedance contrasts due to changes in rock physical properties within the fault zone or due to the juxtaposition of different rock types across the fault), changes in properties within a single rock type (for example, porous vs. nonporous), or unconformities. Receivers at the surface measure reflected energy producing a seismic trace at each location (records of the displacement versus two-way travel time at each receiver). By using a grid of sources and receivers, we can obtain a 3-D image (where z is measured in two-way travel time) of the interfaces causing the reflections. Because the earth does not consist of a simple stack of horizontal layers each with constant but different acoustic impedance, imaging the subsurface is considerably more difficult. Complicating factors include such things as (1) the unknown velocity structure of the subsurface, (2) other arrivals such as multiples, diffracted arrivals, ground roll, etc., (3) structures (folds, dipping beds, faults), and (4) coherent and random noise that can obscure primary arrivals.
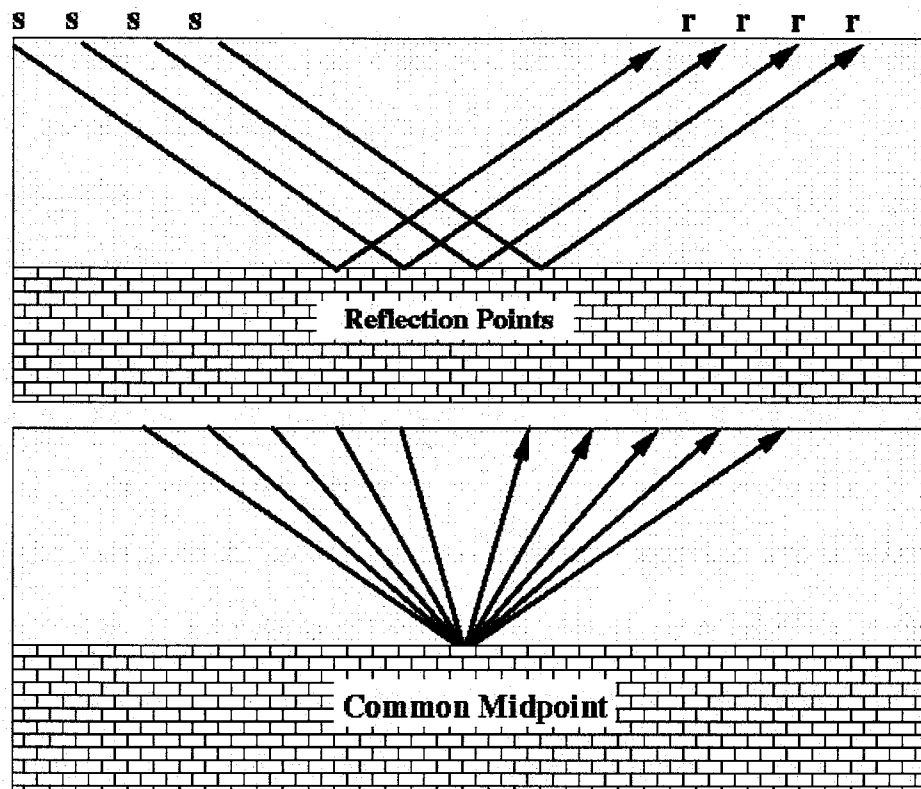
Figure A1-1: (Top)Downgoing source pulses (represented by rays) are reflected at an acoustic impedance contrast in the subsurface. The subsurface is imaged by a series of evenly spaced reflection points midway between the source (s) and receiver (r) pairs. (Bottom) Each subsurface point (common depth point) is imaged multiple times using different source-receiver offsets. Seismic traces are sorted into common midpoint gathers and stacked to improve data quality.

Convolutional model

In the simplest sense, the earth's response can be thought of in terms of a convolutional model. If we model the earth as a series of layers with different acoustic impedances, we can quantify the magnitude and polarity of the reflection events produced by these layers using reflection coefficients:

$$RC = (AI_1 - AI_2) / (AI_1 + AI_2)$$

where RC is the reflection coefficient between layers 1 and 2 with acoustic impedances AI_1 and AI_2, respectively. Thus, if we represent the earth by a series of reflection coefficients, e(t), then the seismic response of the earth, s(t), can be thought of as the convolution (*) of the source signature, w(t), onto the reflectivity series (Figure A1-2):

$$S(t) = w(t) * e(t)$$

From this we see that each interface, represented by a spike in the reflectivity series, is replaced by a scaled version of the source wavelet with polarity determined by the sign of the reflection coefficient. While positive reflection coefficients correspond to increasing acoustic impedance with depth, the polarity of the data (i.e., whether a positive RC is represented by a peak or trough) varies. The most common type, shown in Figure A1-2, is SEG normal polarity where a peak represents increasing acoustic impedance with depth (Sheriff and Geldart, 1995). The seismic trace consists of the sum of all of these reflected wavelets (Figure A1-2). It is apparent even from the simple model shown above that (1) identifying reflections associated with particular interfaces can be difficult due to constructive and destructive interference between reflection events, (2) all peaks and troughs in the wiggle trace may not correspond to acoustic impedance interfaces, (3) high signal-to-noise ratio is necessary if events are stand out above background noise (amplitude standout), (4) not all beds/layers produce detectable reflections, and (5) large acoustic impedance contrasts produce large amplitude (easier to identify) reflection events.
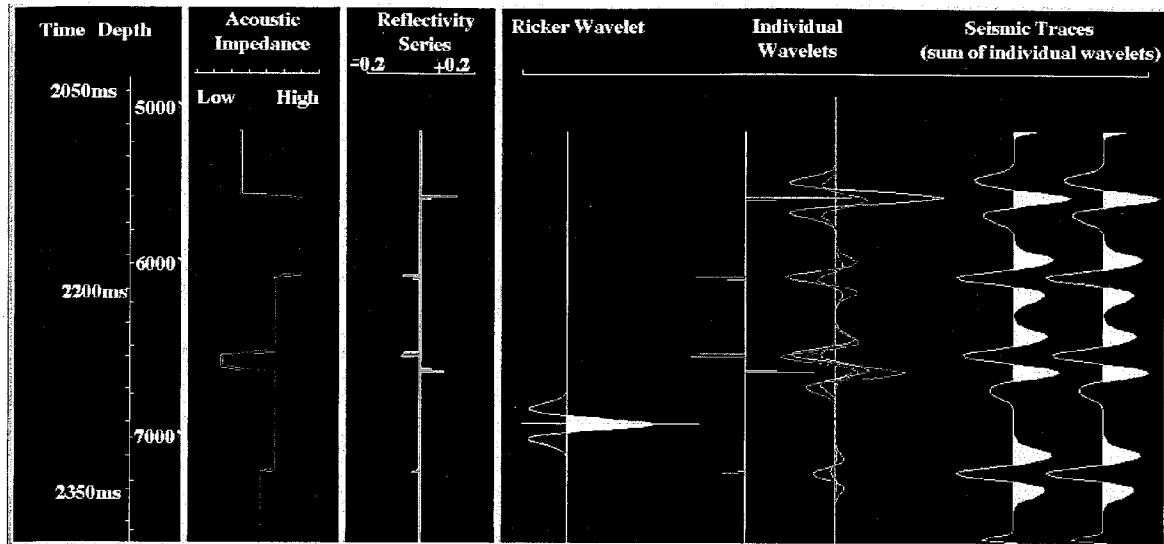
Figure A1-2: Convolutional model of the earth's seismic response. From left to right: the time-depth scale, the acoustic impedance; the reflectivity series; a zero-phase seismic wavelet (Ricker wavelet); the individual wavelets produced by convolving the seismic wavelet onto the reflectivity series (color-coded to the reflectivity spikes); and the seismic trace obtained by summing the individual wavelets.

Vertical resolution

The thinnest bed/layer that produces distinct reflections from its top and base is referred to as the vertical resolution of the data. Based on the above discussion, it is clear that there is not one single factor that controls the vertical resolution but, instead, a host of factors including bed thickness, the magnitude of the acoustic impedance contrast with surrounding layers, the signal-to-noise ratio (S/N), and the duration/frequency of the source wavelet (Figure A1-3). In general, with greater acoustic impedance contrasts thinner beds can be imaged. However, the final resolution is strongly controlled by the source wavelet and the S/N as well. Although an impulse source (a perfect spike) would provide the best resolution, practical limitations make this an unobtainable goal for land surveys. For example, dynamite produces a sharp initial spike of energy, but reverberations after the explosion give the data a somewhat "ringy" appearance. The minimum bed thickness necessary for the reflections from the top

and base of the bed to be separable is ¼ of the length of the incident wave (Figure A1-4). With good quality 3-D seismic data beds as thin as 1/12 to 1/30 of the wavelength can often be identified by a reflection event that is the result of interference between reflections from the top and bottom of the bed. It should be kept in mind that the actual length of the incident wavelet is not the same as the length of the source wavelet because wavelength is dependent on velocity and frequency, and the high frequency (short wavelength) components of the signal attenuate rapidly with depth (Sheriff and Geldart, 1995). Lastly, we must also consider the effect of the sampling rate; Although the earth's response is continuous, we must sample at some finite interval, generally 2 or 4 ms.
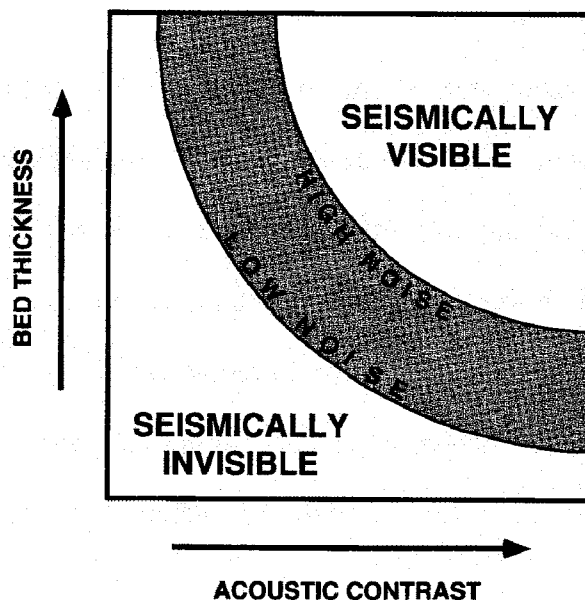
Figure A1-3: A qualitative comparison of the effects of bed thickness, acoustic contrast, and noise level on seismic visibility. In general, with greater acoustic impedance contrasts thinner beds can be resolved (Brown, 1996a).
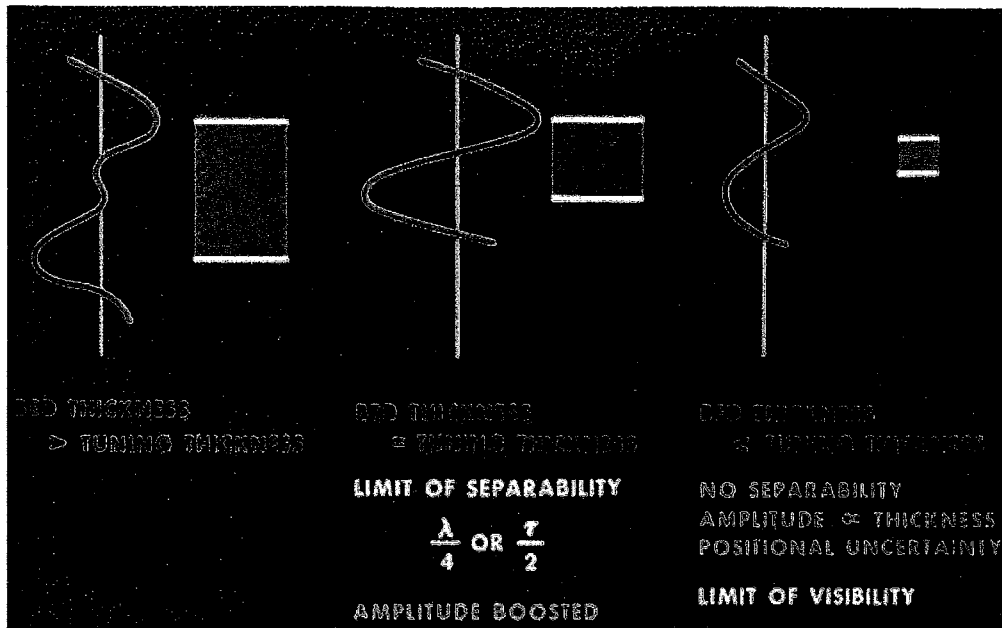
Figure A1-4: The ability to resolve separate reflections from the top and base of a bed is dependent on the length of the seismic wavelet (among other things). When beds are thicker than the tuning thickness (λ/4), individual reflections from the top and base of the bed can be resolved, and the separation is proportional to the bed thickness (Brown, 1996a).

Horizontal resolution

Horizontal resolution refers to "how far apart two separate features involving a single interface must be separated to show as separate features" (Sheriff and Geldart, 1995). As with the vertical resolution, S/N is an important factor affecting the horizontal resolution. The primary control on horizontal resolution of unprocessed seismic data is the Fresnel zone. Although we often represent reflected waves as rays, in reality the reflection is a made up of energy reflected from a zone. The Fresnel zone is the region of the reflector over which returning energy constructively interferes to produce a reflection event. This is expressed mathematically as:

$$R = (\lambda h / 2)^{1/2} = (v / 2)(t / f)^{1/2}$$

where R is the radius of the Fresnel zone, h is the depth, λ is the wavelength of the incident wave, v is the average velocity, t is the arrival time, and f is the frequency. In most data, the horizontal resolution is typically much poorer than the vertical resolution, often by a factor of two or more (Sheriff and Geldart, 1995). Migration (to be discussed later) acts to compress the Fresnel zone in one or two dimensions for 2-D and 3-D migration, respectively. As a result, the resolution of migrated data is substantially improved.

One additional observation to make about the simple convolutional model shown in Figure A1-2 is that reflection coefficients are generally on the order of 0.1 or less. Clearly, reflection events with such low amplitude could easily be lost in the background noise and other arrivals. It should also be noted that the amount of seismic energy returned decreases with depth due to spherical divergence and attenuation. Much of data acquisition and processing focuses on increasing the signal-to-noise ratio, compensating for energy loss with depth, attenuating other arrivals, and enhancing the primary arrivals.

Data Acquisition

Historically, reflection seismology has been subdivided into three fields: acquisition, processing, and interpretation. In order for a survey to be successful, workers in each field must collaborate to design a survey and process the data in such a way as to image the targets of interest. Today, advances in visualization technology and the increasing emphasis on multidiciplinary teams is helping to break down these artificial barriers resulting in more accurate reservoir characterizations that fully integrate all the petrophysical, engineering, and geologic data (Risch *et al.*, 1994).

The way in which 3-D seismic data are acquired on land depends upon the depth to the targets of interest, the resolution required, the purpose of the study (for example, are we

trying to image structural traps, subtle stratigraphic traps, or determine rock and fluid properties?), the project budget, as well as practical considerations such as the terrain and the ambient background noise. Considerations such as these determine the number and spacing of the sources and receivers used and the type of source. The most common survey technique used today is the common midpoint method.

Common midpoint method

The goal of the common midpoint (CMP) method is to sample each subsurface point numerous times using different source-receiver offsets so that during subsequent processing the traces that sample the same subsurface points can be summed to increase the S/N, a process known as stacking. In practice this is usually achieved by using a single source array, which is moved for each shot, and multiple, stationary receivers. When possible, the receivers are laid out in a regular grid in order to sample the subsurface with consistent spacing. Consider first the 2-D case: a source is set up on the ground or in a shallow borehole with a line of equally spaced receivers stretching away from it. A shot is fired, and the acoustic energy travels into the subsurface, spreads spherically, and is reflected at a boundary in the subsurface. The reflection event recorded at each receiver was initiated at the midpoint between the receiver and the source. Thus, the receivers sample the subsurface at a series of evenly spaced points separated by half the source-receiver distance (Figure A1-1). The source is then moved laterally, and the process is repeated. By moving the source by a multiple of the source-receiver distance, we image the same points again (as well as new points) but with different source-receiver offsets. The process is repeated until the desired fold, the number of traces that sample the same common midpoint, is achieved (Figure A1-1). Typically, fold ranges from 48-128. The same process is used for 3-D data except that the receivers are usually laid out in a stationary grid oriented at right angles to the source lines,

and the final result is a 3-D grid of evenly spaced common midpoints. The spacing between the subsurface points in the x and y directions is referred to as the bin size. In areas of rough terrain or where surface obstructions interfere with the survey design, modifications in the survey pattern must be made in order to obtain complete subsurface coverage.

Source and receiver arrays

Over the years, the sources used in reflection seismic surveys have included everything from shotguns to dynamite. The standard source used for most land surveys today is the Vibroseis truck. As their name implies, Vibroseis trucks vibrate. Unlike most impulsive energy sources which are designed to have a source signature as close to a spike as possible, Vibroseis trucks have a very long source pulse; Each truck sweeps through a range of frequencies (anywhere from 10 to 120 Hz) over the course of 7 to 35 s (Figure A1-5). Individually, each truck does not put a significant amount of energy into the ground. To compensate for this, an array of trucks (commonly four), all vibrating in phase, is used. This serves to increase the energy input into the ground and, thus, the depth to which we can reliably image and helps to attenuate horizontally propagating energy during the stacking process.

A similar strategy is used for receivers. Receivers are distributed around a central point and the records for the group are summed and plotted as if the trace was recorded by a single geophone at the center of the array. The spacing of geophones within the group can be manipulated to attenuate coherent noise and other arrivals and to prevent aliasing.

Data Processing

Once the data have been collected, a great deal of signal processing must be done before the data can be interpreted. The primary goals of data processing are to increase the S/N, enhance primary arrivals, attenuate other arrivals, and reposition reflectors to their true subsurface

locations. An example of a data processing workflow is shown in Table A1-1. Because seismic data processing is such a large field, it is not possible to provide a comprehensive summary of this topic. Instead, the remaining discussion will focus on the major steps in the processing flow that are pertinent to this study, namely, stacking, migration, and wavelet processing.

Stacking

Once the data have been sorted into traces (demultiplexing, see below), edited to removed bad traces, and the source signature decompressed (Figure A1-5), the data are then sorted into common midpoint "gathers", groups of traces that sample the same subsurface points. Before these traces can be summed, a velocity correction must be made to account the hyperbolic increase in two-way travel time with increasing offset (normal moveout). The velocity correction necessary is determined by examining a series of velocity panels which are a series panels that show the affects of applying different velocity corrections (normal moveout correction). The velocity correction used is the one that does the best job of flattening the primary arrivals. Because this velocity represents the average velocity down to the reflector being flattened, it is necessary to apply different corrections for different primary arrivals. These velocity estimates, known as NMO velocities, are generally within +/- 10 % of the actual average velocities. Multiples have lower apparent velocities due to their greater travel time, and, as a result, they are undercorrected by the primary velocity correction. When the corrections have been applied, the traces are summed. Primary arrivals are enhanced due to constructive interference while random noise and multiples are attenuated. The final result is a data set (a cube) that consists of CMP stacks, each stack being the equivalent of a normal incidence, zero offset trace plotted at the center of the column of bins.
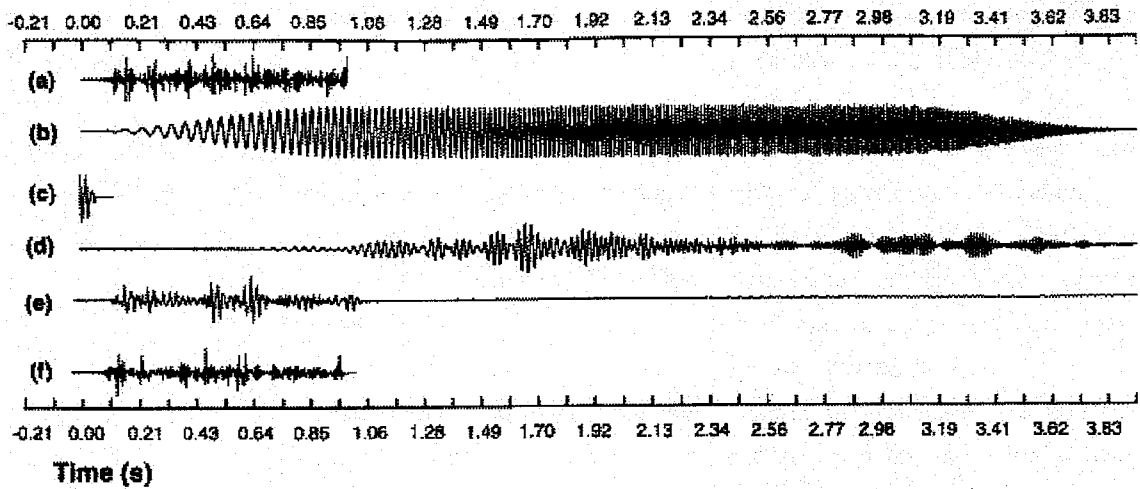
Figure A1-5: Deconvolution of the Vibroseis source signature (from Sheriff and Geldart, 1995). (a) The reflectivity series; b) 10-120 Hz Vibroseis sweep; c) minimum-phase near-surface filter, d) convolution of (a), (b), and (c); e) the result of cross correlation the Vibroseis sweep with (d); and f) the result of applying a zero-phase filter to (e).

Table A1-1: Typical processing workflow (modified from Sheriff and Geldart, 1995)

Process	Problem	Solution
Demultiplexing	Field data is sorted by two-way travel time rather than by traces (i.e. 2ms: trace 1, trace 2, trace3,...; 3ms: trace 1, trace 2, trace 3, ...).	Sort the digital data by traces.
Editing	Dead or malfunctioning receivers	Remove bad traces from the data.
Gain Recovery	Signal strength decreases with increasing travel time due to geometric spreading and inelastic attenuation.	A time-variant gain function is applied to the data. The most common gain function is t^n where n is approximately 2 (Yilmaz, 1987; Ziolkowski *et al.*, 1998)
Vibroseis Correlation	Vibroseis produces a long signal with a wide range of frequencies. The length of the signal is greater than the time between reflection events (Sheriff and Geldart, 1995).	The Vibroseis signal is cross correlated with the seismic trace. Assuming that the earth's response is white, this should compress the Vibroseis wave train into a short, near zero-phase wavelet (Yilmaz, 1987).
Statics	Variations in the thickness of the near surface weathering layer and topographic variations need to be corrected for.	Topographic variations are measured and corrected for, and a low velocity layer travel time correction is applied so that all data is measured relative to a seismic datum. Static corrections and NMO corrections (see below) are done iteratively (Sheriff and Geldart, 1995).
CMP Gathers	Low S/N. The same subsurface points are sampled multiple times using different source-receiver offsets.	The data are sorted into common midpoint gathers, groups of traces that sample the same subsurface points.
Filters	Signal aliasing may create false reflections, and noise at particular frequencies may obscure the signal.	The data are transformed into the frequency-apparent wavenumber (F-K) domain in order to separate noise from signal. A filter is designed to pass the narrow wedge of data that is centered on the frequency axis (Yilmaz, 1987).

Process	Problem	Solution
Velocity Analysis / Normal Moveout Correction	Before the traces can be stacked, the hyperbolic increase in two-way travel times with increasing offset (normal moveout) must be corrected. This requires information about the velocity structure.	A series of velocity panels is examined to determine which velocity does the best job of flattening the primary arrivals (Sheriff and Geldart, 1995).
Dip Moveout	Dipping beds still show moveout after the NMO correction has been applied.	A modified version of the NMO correction is applied.
Stacking	The S/N of each individual trace is low.	The traces in each CMP gather are summed to create a CMP stack with significantly greater S/N. Each CMP stack is equivalent to a normal-incidence, zero-offset trace.
Predictive Deconvolution	Multiples are present in the data.	Knowledge of the arrival times of primaries, assuming the earth's response is white, is used to create a deconvolution operator (a prediction-error filter) that removes multiples (Peacock and Treitel, 1969; Yilmaz, 1987; Sheriff and Geldart, 1995; Taner *et al.*, 1995; Ziolkowski *et al.*, 1998).
Migration	The normal incidence reflection does not lie directly below the source-receiver pair.	Data elements are repositioned to their true subsurface locations either in time or depth (Sheriff and Geldart, 1995).
Wavelet Processing	The embedded wavelet (source signature) is complex, and it may be difficult to pick out the onset of a reflection.	The embedded wavelet is replaced with a more standard wavelet that facilitates interpretation.
Optional Processing: attribute analyses, inversion, etc.	Reservoir properties are unknown.	Various geostatistical methods are used to determine reservoir properties from seismic data.

Table A1-1 (continued)
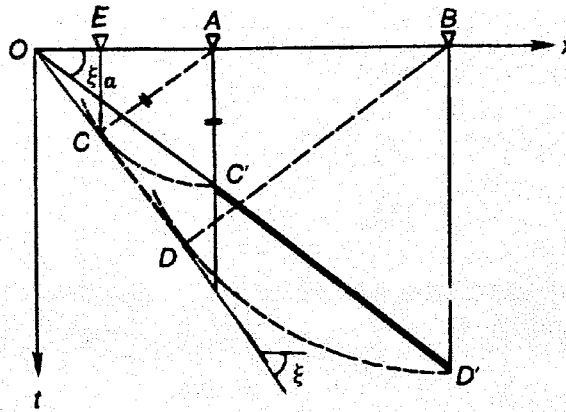
Figure A1-6: The effect of migration on dipping strata (from Sheriff and Geldart, 1995). A dipping bed (CD) appears to be more gently dipping in unmigrated data (C'D') due to the assumption that the normal incidence ray traveled vertically downward from the surface to the reflector. Migration attempts to reposition reflectors to their true subsurface locations (CD).

Migration

Although we now have a set of traces that are equivalent to zero offset traces, we still have the remaining problem of the orientation of those traces. For example, consider the case of dipping strata (Figure A1-6). While a seismic section of CMP stacked data shot over this strata will still consist of zero-offset, normal-incidence data, the normal incidence ray will not sample a point vertically below the source and receiver. Instead, the normal incidence ray will reflect from a point further updip. Because seismic sections consist of traces plotted vertically below the source-receiver location, the dip seen in seismic sections will appear shallower than reality. Similar problems are encountered when strata are folded, faulted, etc. Migration is the process of repositioning reflectors to their true subsurface positions. This can be done in either time or depth, although the former is more common. In addition to presenting a more accurate picture of the subsurface geometry, migration also improves the
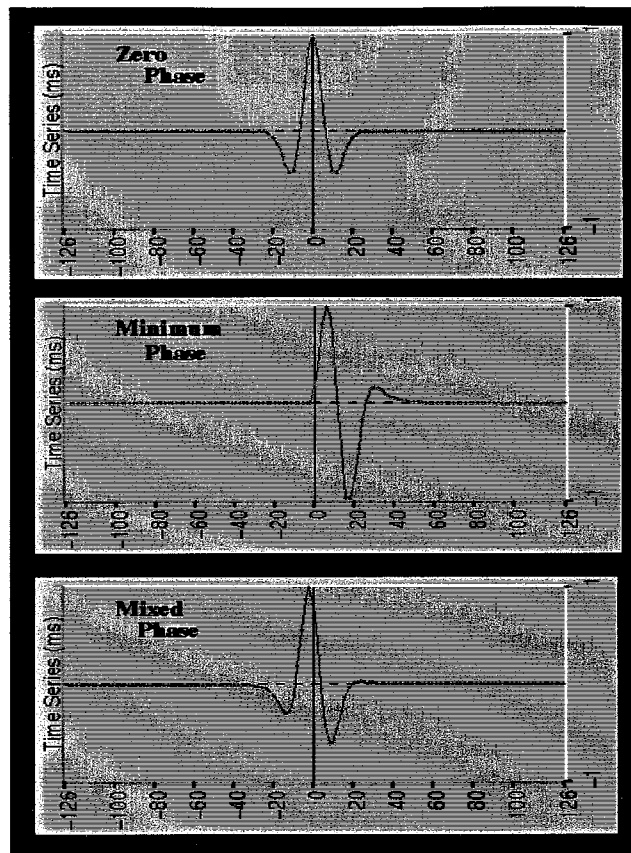
Figure A1-7: Three types of seismic wavelets, zero phase, minimum phase, and mixed phase. Most seismic data is originally mixed phase and is processed to be zero or minimum phase (in theory).

resolution of the data by collapsing the Fresnel zone, thus, removing the out-of-plane reflections (Sheriff and Geldart, 1995).

Wavelet processing

One of the final (optional) steps in data processing is choosing the shape and polarity of the embedded wavelet (the wavelet that in theory was convolved onto the reflectivity series to produce the seismic trace). The wavelet embedded in the data is of primary importance in the interpretation process. If we want to pick the onset of a reflection event that represents the two-way travel time to some zone of interest in the subsurface, we need to know if this onset is marked by a peak, a trough, a zero crossing, or something in between (Figure A1-7). In

order to change this wavelet to something easier to interpret, such as a zero phase wavelet which maximizes the vertical resolution and consists of a high amplitude peak centered on t=0 (the onset time) with two low amplitude side lobes, it is necessary to first remove the actual wavelet from the data. Once this has been removed, the more desirable wavelet can be convolved onto the data. This process is usually completed in a single step by designing a filter that converts the actual into the desired wavelet (Yilmaz, 1987). There is considerable controversy over how well this process works in practice. As pointed out by Ziolkowski *et al.* (1998) common practices such as applying a time-varying gain function of the form t^n and gapped predictive deconvolution (used to remove multiples) virtually ensure that the original wavelet embedded in the data will vary both laterally and with depth. Consequently, unless the source signature is measured in the field and considerable care is taken to preserve this wavelet during processing, no data can ever be truly zero phase because the original wavelet will always be unknown. Despite these arguments, many major oil companies appear to have overcome these difficulties and have developed in-house processing techniques which make their data truly zero phase (Corbett *et al.*, 1995; Raeuchle *et al.*, 1997; Schuelke *et al.*, 1998).

Geologic Interpretation of Seismic Data

To define the subsurface geology from seismic data, reflection events that correspond to units of interest and major boundaries such as formation tops and sequence boundaries need to be identified and tracked throughout the volume. The patterns of internal reflectors can then be mapped and classified using sequence stratigraphic concepts (downlapping, onlapping, truncated, etc.) to shed light on the geologic history (Mitchum *et al.*, 1977).

Well-seismic tie

Before any of this can be done, however, we must first establish a good tie between the wells (measured in depth below the surface) and the seismic data (measured in two-way travel time from the seismic datum). In order to determine which reflection events correspond to which acoustic impedance contrasts seen on the logs, we need information about the velocity structure of the subsurface.

Sonic logs are the most common source of velocity information. During logging, a tool equipped with an acoustic source and several receivers is lowered into the borehole. The source emits a high frequency "ping" (10's of kHz range) which travels into the formation and is picked up at the receivers. Multiple receivers are used in order to compensate for bore hole effects (e.g. hole rugosity and shape, mud cake, etc.; Doveton, 1994). The quantity measured is interval transit time, Δt, in $\mu s/ft$ (the inverse of velocity). Interval transit times are typically logged using 0.5' to 2.0' intervals. Interval transit times and the corresponding sonic velocities for common reservoir minerals are shown in Table A1-2 below.

Matix Mineral	Transit Time ($\mu s/ft$)	Velocity (ft/s)
Quartz	55.5	18,018
Calcite	47.5	21,053
Dolomite	43.5	22,989

Table A1-2: Transit times and sonic velocities for common reservoir matrix minerals (Doveton, 1994).

While logging does provide us with detailed velocity information, sonic logs need to edited and then calibrated with checkshot surveys or vertical seismic profiles (VSP; Figure

A1-8). If these data sources are not available, NMO or stacking velocities can also be used for a rough calibration (Adcock, 1993). This calibration is necessary for several reasons:

◆ Wells are often only logged over one or more intervals of interest rather than from the surface downward, resulting in gaps in the time-depth relationship.

◆ Velocity is slightly frequency dependent. At typical sonic frequencies (kHz range) porous rocks do not behave as perfectly elastic materials; The pore fluids behave viscoelastically (i.e. after the removal of the external stress, there is a brief lag time before they return to their unstressed state). The end result is that the rock behaves as if it were more rigid, resulting in sonic velocities that are slightly higher (only a few percent) than seismic velocities (Sheriff and Geldart, 1995; Marion and Jizba, 1997).

◆ Sonic logs sample a very small radius around the bore hole, typically several feet or less (within the flushed zone). The exact radius depends on the spacing of the source and receivers on the tool. Longer tools with greater separation provide deeper penetration into the formation (Doveton, 1994). Seismic data, in contrast, sample a significantly larger volume of rock. The exact amount is a function of the maximum azimuth/offset used in the CMP stacking process. If there is significant lateral heterogeneity, the sonic velocity at the well bore may differ from the seismic velocity.

◆ Sonic velocities are affected by the bore hole environment. Although compensated sonic tools are usually run today, they cannot completely remove the effects of the bore hole environment (J. Ratjahr, pers. comm. 1997). In addition, we often have only older uncompensated sonic logs to work with. Factors affecting the bore hole environment include hole rugosity, invasion, mud cake, washouts, hole shape, erosion, weathering, and drilling-induced fracturing (Ausburn and Butler, 1977; Doveton, 1994). Many of these effects can be corrected with careful editing of the sonic logs before calibration (Ausburn and Butler, 1977).
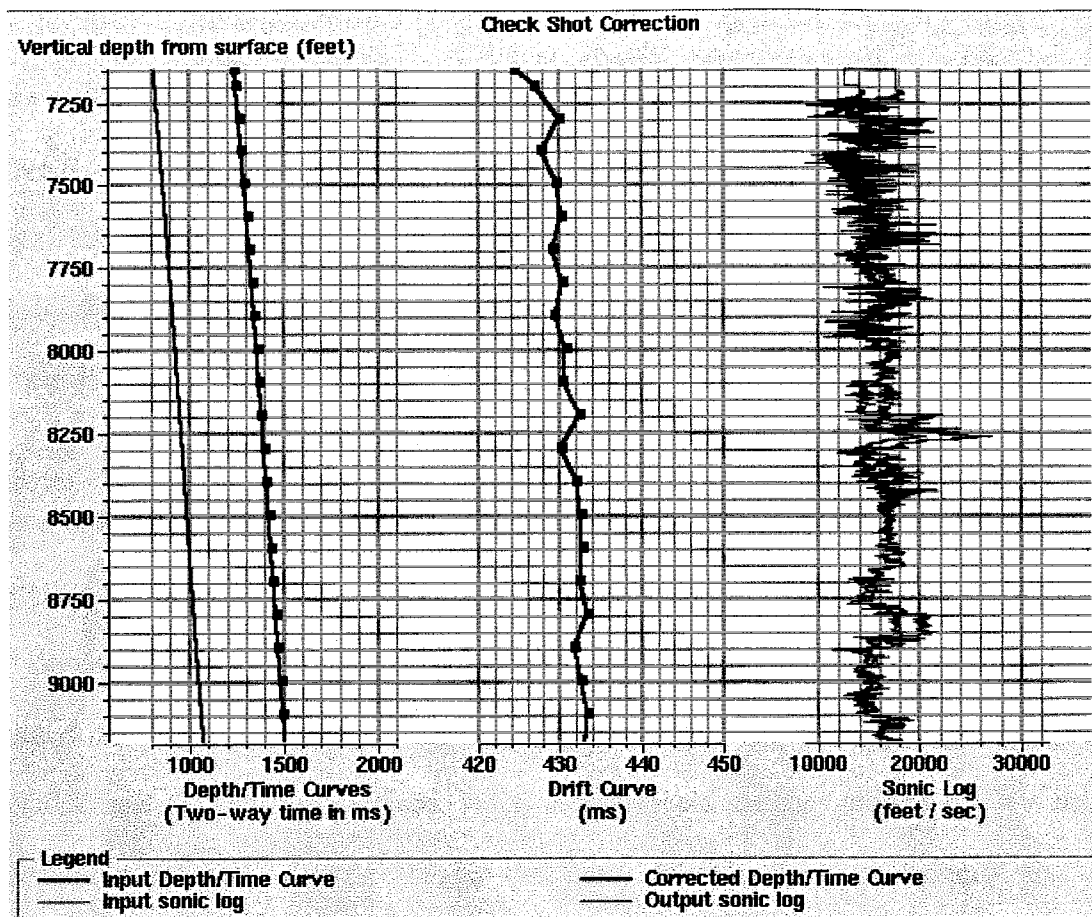
Figure A1-8: Calibration of a sonic log with checkshot data. The checkshot data consist of a series of time-depth pairs obtained using a seismic source and a receiver in the wellbore. Based on the checkshot data, a correction is made to the sonic log. The final time-depth curve calculated from the calibrated sonic log honors the checkshot data.

The sonic can be calibrated to honor the checkshot or VSP data exactly or to use a best fit smooth curve to avoid large jumps in sonic velocities.

Once the sonic log has been calibrated, it is integrated (with respect to depth) to give two-way travel time. The validity of this time-depth relationship is then checked by creating a synthetic seismogram ("synthetic") and comparing it with the actual seismic data at the well location. Three things are needed to create a synthetic: (1) a calibrated sonic log, (2) a density log, and (3) an estimation of the seismic wavelet. The density log is multiplied by the inverse of the sonic log to create an acoustic impedance log from which the reflectivity series

can be derived. If a density log is not available, a constant value can be used without introducing too much error because densities of sedimentary rocks vary over a fairly small range (~ 2-3 g/cc) while velocities range over a much larger interval (Sheriff and Geldart, 1995). Alternatively, the density log can be approximated using Gardner's rule (an empirical relationship stating that density (g/cc) is equal to 0.23 $v^{1/4}$ where v is velocity in ft/s) or estimated from porosity logs. The reflectivity series is then convolved with the seismic wavelet to produce a synthetic seismogram. Because the seismic wavelet is rarely measured in the field (Ziolkowski *et al.*, 1998), it usually has to be approximated using seismic and/or well data.

As pointed out by Hampson and Russell (1994), wavelet extraction techniques can be divided into three main categories: (1) purely deterministic methods, (2) purely statistical methods, and (3) well log methods. Purely deterministic methods require that the source signature is measured directly (by far the most desirable, but least common method). Statistical wavelet extraction methods, in contrast, are based entirely on the seismic data, They are generally less reliable in terms of always providing an accurate estimate of the phase spectrum of the wavelet (simply due to the lack of data, i.e., the problem is underdetermined). Statistical wavelet extraction methods are based on the assumption that the earth's reflectivity series is white (Yilmaz, 1987). With this assumption, the autocorrelation of the seismic trace should essentially be that of the wavelet. Autocorrelation in the time domain is equivalent to multiplication in the frequency domain. Thus, if the seismic trace is s(t) and the wavelet is w(t):

$$s(t)*s(t) \approx w(t)*w(t) = \{W(\omega)\}^2$$

where $W(\omega)$ is the fourier transform of w(t). Recall that the Fourier transform uniquely describes the waveform in terms of an amplitude spectrum and a phase spectrum:

$$W(\omega) = A(\omega)\exp(i\phi(\omega))$$

where $A(\omega)$ is the amplitude spectrum, and $\phi(\omega)$ is the phase spectrum. If it is assumed that

the phase spectrum is zero, this simplifies to :

$$W(\omega) = A(\omega)$$

Thus,

$$w(t)*w(t) = (A(\omega))^{1/2}$$

and we now have both the amplitude and phase spectra which uniquely define the wavelet.

By using the inverse fourier transform, the estimated wavelet can then be tranformed into the

time domain. This results in a good estimate of the amplitude spectrum of the wavelet, if the

phase spectrum is assumed to be zero; the extraction time window is restricted to a zone of

good data quality covering the interval of interest; and the length of the window is several

hundred ms greater than the expected length of the wavelet (to avoid edge effects).

The final group of methods, well log- based wavelet extractions, has the potential to

provide very accurate amplitude and phase data at the well location, but it requires that the

time-depth tie between the well and seismic data be fairly well established. As a result, this

method works best as a final step used to improve the tie in character between the synthetic

and the seismic after a fairly good time-depth relationship has been found using other

methods. The quality of this character match is highly dependent on the strength of the prior

correlation between the well and seismic data. Because each method has its own strengths

and weaknesses, a combination of methods often yields the best results (Hampson and

Galbraith, 1994). Ultimately, the methods employed depend on the data available, the quality

of the data, the time available, and the purpose of the study.

Once the wavelet has been convolved onto the reflectivity series, mismatches between

the actual seismic data and the synthetic can then be evaluated and corrected for if necessary

(and justified) by stretching and squeezing the sonic logs or by applying static time shifts. When a satisfactory match is obtained, reflection events corresponding to zones of interest can then be identified and tracked throughout the data volume. These events are called "horizons".

Horizon interpretation

Picking or interpreting a horizon throughout the data is commonly more complicated than simply tracking a continuous peak or trough. Geologic and geophysical complexities make interpretation something of an art form, and many factors need to be considered when deciding where to place the horizon. Of primary importance is the geological interpretation. For example, if the event being interpreted has been identified from well logs as corresponding to an acoustic impedance contrast between a lowstand siliciclastic fan above and a highstand carbonate below, we might expect to see reflections in the fan downlapping onto the top of the carbonate reflection. In this case, the event being picked would be identified in the seismic by its relationship with surrounding reflections (i.e. the carbonate top corresponds to the downlap surface in the seismic). Relationships such as this can be very helpful when trying to track a horizon across faults and through noisy regions in the data. However, geology alone is not sufficient to produce a good interpretation. The geophysics of the situation must also be considered. For example, we must address questions such as: (1) What are the phase and frequency content of the data? (2) What frequencies are predominantly noise? (3) What are the horizontal and vertical resolution of the data? (4) Is the event we want to identify seismically resolvable? (5) Does the reflection event we are interested in correspond to a peak, a trough, or a zero crossing, or is it somewhere in between? (6) Does the polarity of the event change across the survey? (7) Are there artifacts

in the data that could be mistaken for reflections or faults? (8) How accurate is the well-seismic tie? (9) Are thin bed tuning effects occurring?

The seismic character of the event can be also be used to help in the interpretation process. Seismic character includes the shape of the amplitude envelope, the number of cycles that show amplitude standout, the dominant frequency, and the continuity (Sheriff and Geldart, 1995).

Advances in interpretation software facilitate the interpretation process: the data cube can be sliced in virtually any direction; continuous loops can be used to determine how well a picked horizon ties throughout the data volume; a horizon that has been picked on a grid of seed lines (interpreted by hand on series of intersecting 2-D lines) can be autotracked or interpolated through the remainder of the data, and the resulting horizon can be smoothed; the seismic data can be "flattened" on a picked horizon to remove the effects of postdepositional deformation; and geologic modeling software can be used to test various geological interpretations.

Sequence stratigraphy

Depositional sequences, the building blocks of sequence stratigraphy, provide a chronstratigraphic framework which aids in the interpretation of stratigraphy from seismic sections. A depositional sequence is a chronstratigraphic unit originally defined by Sloss (1963) and modified slightly to be used at the scale available with seismic data by Mitchum et al. (1977) as "a relatively conformable succession of genetically related strata and bounded at its top and base by unconformities or their correlative conformities" (Mitchum et al., 1977 in Brenner and McHargue, 1988, p. 53). In using seismic data for sequence stratigraphic studies several assumptions must be made: 1) Seismic horizons are essentially isochronous, and 2) seismic horizons represent major bedding surfaces (Brenner and McHargue, 1988).

Although sequences and the original sequence stratigraphic method proposed by Mitchum *et al.* (1977) was tailored for seismic data, its use has been extended to outcrop and well log studies as well.

Sequences are classified as Type 1 or Type 2 depending on the nature of the lower bounding surface. A Type 1 sequence is bounded below by a type 1 sequence boundary (SB1). Type 1 sequence boundaries are believed to be correspond to falls in relative sea level and are characterized by subaerial erosion and generally accompanied by a basinward facies shift (Van Wagoner et al., 1988). In contrast, Type 2 sequence boundaries (SB2) are not associated with a lowering of relative sea level and, as a result, are not associated with a facies regression. Instead they are marked by "subaerial exposure and a downward shift in coastal onlap" (Van Wagoner *et al.*,1988; Figure A1-9).

Sequences can be subdivided into three systems tracts, the exact progression of which depends on the type of sequence. Systems tracts represent a suite of related depositional systems and are defined by their location within the sequence and the stacking patterns of the internal parasequence sets (Van Wagoner *et al.*,1988; Galloway, 1998a and 1998b). Type 1 sequences consist of a lowstand, a transgressive, and a highstand systems tracts. Type 2 sequences differ in that the lowstand systems tract is replaced by a shelf margin systems tract (Figure A1-9). The sequence stratigraphic concept of lowstand-highstand reciprocal sedimentation was developed largely from siliciclastic continental margins and is based on the idea that during highstands, the shelves will be flooded, trapping sediment and starving the basin. In time, sediment deposited on the shelf with build outward and may reach the shelf margin and be remobilized by gravity flow processes and transported to the slope and basin. Thus, if all else is constant, rising sea level should result in a transgression of facies across the shelf and coastal onlap. During lowstands, the subaerially exposed shelf is eroded, sediment bypasses much of the shelf and possibly a portion of the slope to be deposited along

the lower slope and basin, building up submarine fans (Mitchum *et al.*, 1977; Posamentier *et al.*, 1988; Posamentier and Vail, 1988; Van Wagoner *et al.*,1988; Posamentier and Erskine, 1991).

There is significant controversy regarding the sea level interpretations of the various elements of the lowstand, transgressive, and highstand systems tracts, and some workers prefer to think of these in more general non-genetic terms with lowstand and highstand systems tracts simply referring to the relative positions of these elements with a sequence (i.e. stratigraphically high or low; Galloway, 1998a and 1998b). Despite the controversy surrounding sequence stratigraphic models, they can still be useful tools in the interpretation process if it is kept in mind that the models were created to (1) advance our understanding of the changes in that occur in shelf margin deposition during changes in relative sea level and (2) to provide a chronostratigraphic framework to aid in the interpretation of seismic data. They were not meant to provide workers with a rigid classification scheme that would apply in all tectonic and depositional settings (Weimer and Posamentier, 1993).
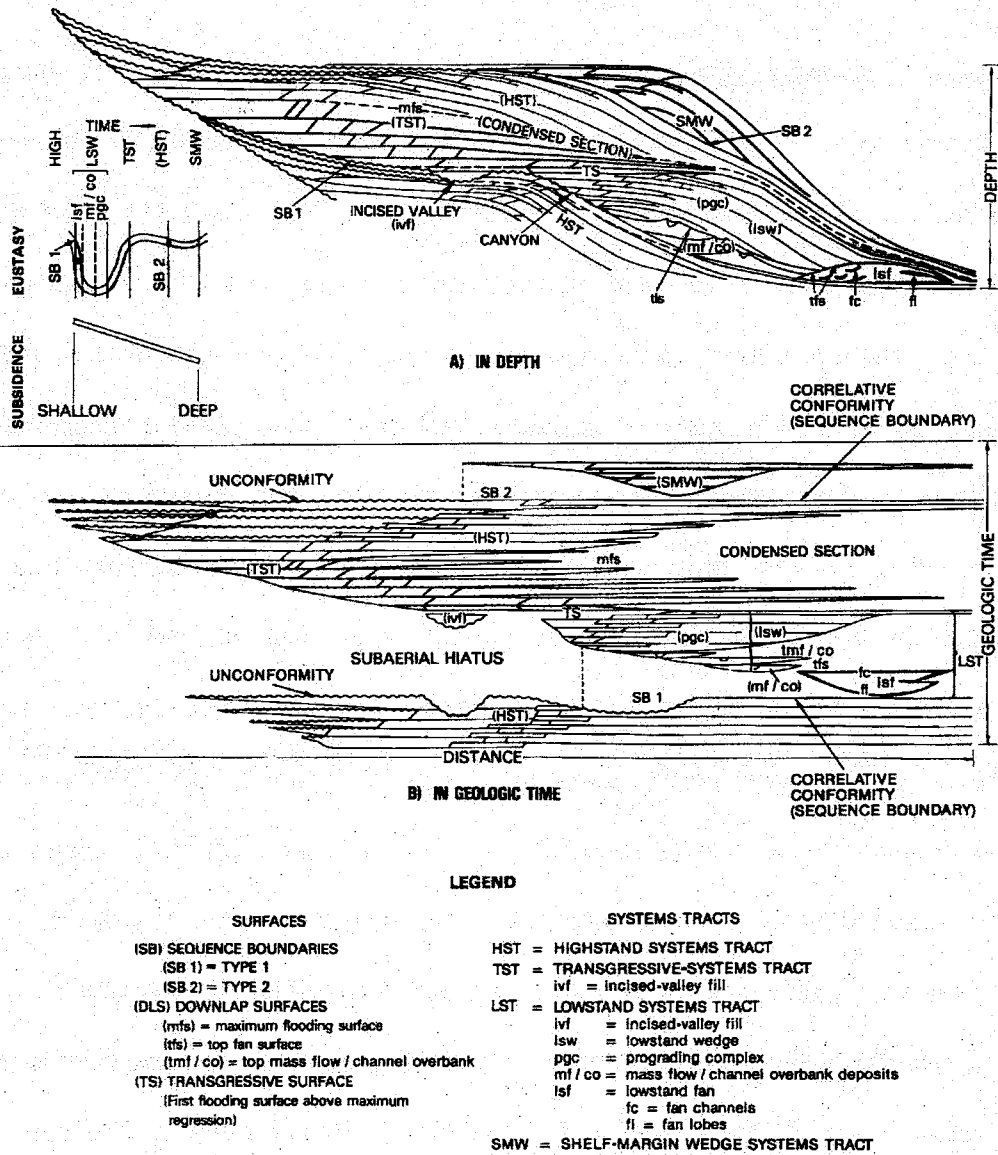
Figure A1-9: The systems tracts comprising Type 1 and Type 2 sequences (Weimer and Posamentier, 1993).

Appendix 2: Submarine Fan Models

Submarine fan depositional models

Most depositional or facies models subdivide submarine fans into an upper, middle, and lower fan, each of which has characteristic morphologic features and facies associations (though these vary considerably between models). In general, the upper fan is characterized by a leveed channel complex which joins upslope to a feeder channel or submarine canyon (Figure A2-1). The size of the levees is a function of the sand:mud ratio with muddy systems forming more extensive levees and stable channels, much as their fluvial counterparts do (Reading & Richards, 1994). Volumetrically, levee/overbank deposits dominate over coarse-grained channel deposits in the upper fan (Howell & Normark, 1982). On high resolution seismic profiles through modern fan systems, levees have characteristic "gull wing" shapes, and slides and slumps directed both into the channel and down the sides of the levees are common. Isopach maps of the upper fan region show elongate sediment thicks along the channel axes with decreasing relief downslope as the middle fan region is encountered (Galloway, 1998a and 1998b). The end of the levee system marks the beginning of the midfan region. Here flows exit the confines of the levee system, and sediment is deposited rapidly, resulting in a convex upward profile or "depositional bulge" (Howell & Normark, 1982). As a whole, the midfan is characterized by a series of overlapping suprafan lobes where active deposition is occurring. These lobes may or may not have distributary channels. Some models (e.g. Mutti and Ricci Lucchi, 1972 *in* Reading, 1996) place unchannelized (depositional) lobes in the outer/lower fan; However, few modern examples of such systems are known. More commonly, modern submarine fans have lower fan regions dominated by unchannelized muddy turbidites that are difficult to separate from basin plain deposits. (Howell & Normark, 1982).
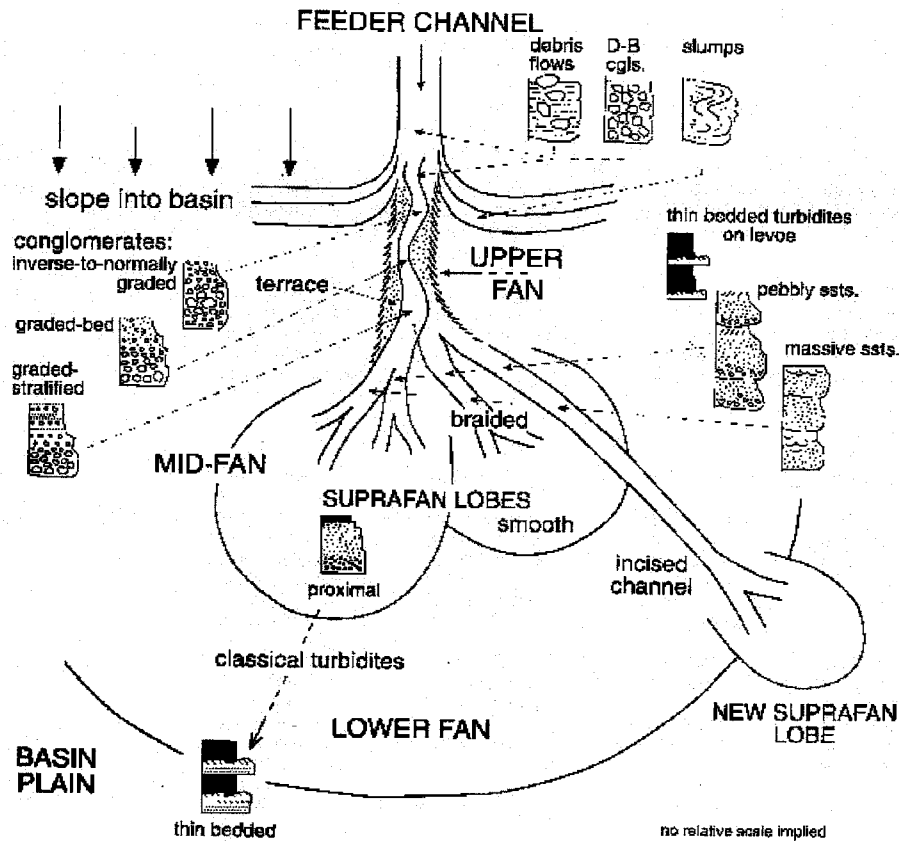
Figure A2-1: Submarine fan model proposed by Walker (1978). The fan is fed by a feeder channel cut into the upper slope, and the fan itself consists of an upper fan, mid-fan, and lower fan.

Given the large variety of modern and ancient submarine fans, one single model cannot adequately describe all fans. Of all the fan classification schemes available, the one proposed by Reading and Richards (1994) is the most applicable to ancient submarine fans. Their classification scheme subdivides submarine fans on the basis of grain size into mud-rich, mud/sand-rich, sand-rich, and gravel-rich point-source and multiple-source submarine fans and ramps. The characteristic features of each class are summarized in Table A2-1. Some generalizations can be made about the effect of grain size:

Feeder System Type Dominant Grain Size	Single Point-Source Submarine Fans			
	Mud	Mud/Sand	Sand	Gravel
Size	Large	Large-moderate	Moderate	Small
Slope Gradient	Low 0.20–18 m/km	Low-moderate 2.5–18.0 m/km	Moderate 2.5–36 m/km	High 20–250 m/km
Shape Radius/Length	Elongate 100–3000 km	Lobate 10–450 km	Radial/lobate 10–100 km	Radial 1–50 km
Source Area Size Gradient Distance	Large Low Distant	Moderate Moderate Moderate	Moderate-small Moderate Close	Small High Close
Feeding Systems	Large, mud-rich river delta	Large, mixed load, river delta and/or downdip canyon	Shelf failure or shelf canyon	Fan delta or alluvial cone
Supply Mechanism	Infrequent slumps and slump-initiated low-density turbidity currents; contour currents	Mainly high- and low-density turbidity currents	Reworking or direct access to shelf clastics; low-efficiency turbidity currents	Frequent mass flows, slumps; river-generated turbidity currents
Size of Flows	Very large	Moderate	Moderate-small	Very small
Channel System	Large, persistent; meandering to straight with well-developed stable levee system	Moderate scale; meandering to braided systems laterally migrating with levees	Braided to low-sinuosity impersistent channels and chutes; rapid lateral migration	Braided, small impersistent chutes
Distal Slope/ Lower Fan Sediments	Thin, sheet-like flows forming interbedded sands, silts, and muds; coarse intervals forming thin clastic sheets	Mixed-load turbidity current flows forming lobes of interbedded sands and muds	Sand-rich turbidity current flows forming low-relief lobes and sand sheets	Thin, dilute turbidity current flows forming thin distal turbidites
Principal Basin Plain Deposits	Turbidites> Hemipelagics	Hemipelagics> Turbidites	Hemipelagics	Hemipelagics

Table A2-1: Sedimentological characteristics of point source submarine fans based on grain size (adapted from Reading and Richards, 1994).

1. As grain size increases, the slope gradient tends to increase, and channel systems become less persistent due to rapid channel migration.

2. As grain size decreases, the size of the source area, the depositional system, and the downcurrent fan length all tend to increase. In addition, channels become more stable and sinuous, and the size of flows, fans, and channel-levee systems increases.

While grain size and feeder type exert a strong control the type and distribution of the architectural elements of the fan (channels, levees, lobes), basin topography/structure is a

primary factor influencing the geometry of the submarine fan. The current models are based on deposition onto a structureless basin plain. When such topography, or lack there of, is present, the classic elongate, lobate, or radial fan shape can be obtained. However, as pointed out by Reading and Richards (1994) this is the exception rather than the norm.

Sequence stratigraphic models of submarine fan deposits

In the classic "slug" model proposed by Mitchum et al. (1977), submarine fans occur in lowstand systems tracts which are believed to form during a cycle of relative sea level fall followed by the onset of a later slow rise in relative sea level. If there is a discrete shelf edge, the lowstand systems tract may contain a lowstand or basin-floor fan and an overlying lowstand wedge (Figure A2-2). The lowstand fan forms during the phase of relative sea level fall. During this time, the shelf and possibly part of the slope are subaerially exposed, and fluvial incision on the shelf and canyon formation on the slope provides a source of siliciclastic sediment. Canyons incised into the slope funnel density currents out into the basin, and point-sourced submarine fans form on the basin floor and possibly the lower slope (Posamentier et al., 1988; Posamentier and Vail, 1988; Van Wagoner et al., 1988). Lowstand fan deposition ends when the rate of eustatic sea level fall at the shoreline break falls below the rate of subsidence (assuming a constant sediment supply; Posamentier et al., 1988). In seismic sections, lowstand fans are often associated with the following features (Posamentier et al., 1988; Posamentier and Vail, 1988; Van Wagoner et al., 1988; Posamentier and Erskine, 1991):
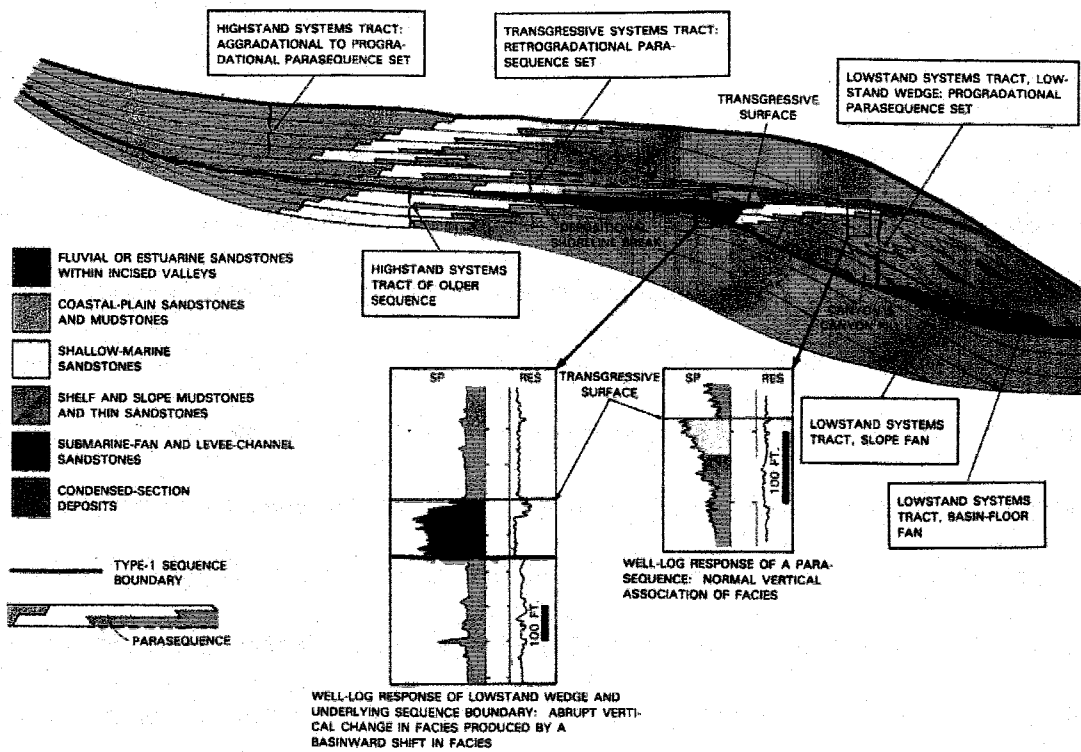
Figure A2-2: Sequence stratigraphic model showing the components of the lowstand systems tract: the basin-floor fan, the slope fan, and the lowstand wedge (adapted from Van Wagoner et al., 1990).

♦ Fan-shaped reflections in plan view

♦ Reflections pinchout against paleobathymetric highs

♦ Internal bidirectional downlap

♦ High amplitude continuous reflections that onlap the basin margin

♦ Lower boundary coincident with the type 1 sequence boundary

♦ Upper boundary is a downlap surface for the overlying lowstand wedge

♦ Occurrence at the base of the slope and basin floor

♦ Subtle external mounding

♦ Erosion of canyons in the slope

♦ Incised valleys on the shelf

♦ Bypass of the upper and middle slope

The lowstand wedge, in contrast, forms during a relative stillstand or early sea level rise and can be divided into a slope fan and an upper progradational lowstand wedge (Figure A2-2). This two-part lowstand wedge geometry is most commonly seen in areas with well developed canyon systems. Like the lowstand fan, the slope fan consists of point source submarine fan deposits. Active leveed channel deposition occurs on the slope and upper fan, and rhythmic turbidites and debris flow deposits occur down fan on the middle and base of the slope. Overall, the sediments are more proximal than those of the basin-floor fan, and sands are concentrated in the channel systems in sand/mud-rich systems and in sheet sands in sand-rich systems (Posamentier *et al.*, 1988; Galloway, 1998a and 1998b). Features associated with a slope fan in seismic sections include many of those listed for lowstand fans, in particular, the fan shape, the bidirectional downlap, the external mounding, and the pinchouts against paleobathymetric highs as well as the following additional features (Posamentier *et al.*, 1988; Posamentier and Vail, 1988; Van Wagoner *et al.*, 1988):

♦ The slope fan onlaps the sequence boundary on the slope (bypasses the shelf)

♦ The upper boundary of the slope fan may be a downlap surface for the upper and middle portions of the overlying progradational lowstand wedge

♦ Channel/levee systems may be well developed in mud-rich and sand/mud-rich fans ("gull wings" on seismic profiles)

The lowstand wedge marks the change to channel filling rather than incision as the rate of sea level fall either slows or reverses. As valleys on the shelf begin to fill, coarse sediment previously bypassing the shelf is trapped, and density flows become less frequent (Posamentier *et al.*, 1988). Sediment that does reach the slope and basin forms a wedge-

shaped unit with progradational to aggradational parasequence stacking patterns. As the supply of coarse sediment from the shelf decreases, the sand:mud ratio on the slope and in the basin decreases (Posamentier *et al.*, 1988). With continued sea level rise, fluvial/deltaic systems may prograde into the canyon and out over the earlier slope fan and lowstand fan deposits. The resulting sediments may consist of prograding delta front turbidites in proximal locations and debris flow deposits in more distal settings. Features associated with progradational lowstand wedges in seismic section include (Posamentier *et al.*, 1988; Posamentier and Vail, 1988; Van Wagoner *et al.*, 1988):

♦ Incised valley fill on the shelf

♦ Reflections onlap the sequence boundary on the shelf

♦ Overall wedge-shaped geometry

♦ Internal reflections downlap the slope fan or basin-floor fan

♦ Progradational to aggradational stacking patterns

♦ Top boundary is the upper boundary of the lowstand systems tract (a maximum flooding surface/transgressive surface)

It should be noted that the lowstand wedge seen in seismic sections and described by Mitchum (1985), Posamentier *et al.* (1988), Van Wagoner *et al.* (1988), and Posamentier and Erskine (1991) among others has not been observed in many modern fans and its origin and existence (or lack thereof) is still a subject of considerable debate (e.g. Galloway, 1998a and 1998b).

Appendix 3: Seismic-Guided Reservoir Characterization Fundamentals

The complex trace

"Complex trace analysis treats a seismic trace … as the real part of an analytical signal or complex trace" (Taner *et al.*, 1979). The complex trace is the sum of the real part (the seismic signal) and an imaginary part called the quadrature trace, the conjugate or imaginary component. The quadrature trace is essentially a -90° phase-shifted version of the seismic trace, and with a few assumptions it can be uniquely determined for any seismic trace that can be represented by Fourier series (Taner *et al.*, 1979). In complex space, the complex trace is a helix defined by the real and imaginary traces (Figure A3-1). The projection of the helix onto the real plane is the seismic trace, and the projection onto the imaginary plane is the quadrature trace. The perpendicular distance from the helix to the time axis is the amplitude envelope, also called the instantaneous amplitude or reflection strength. The angle between the line along which the instantaneous amplitude is measured and the horizontal is the instantaneous phase (Figure A3-1). Mathematically, the complex trace is defined in Cartesian coordinates as:

$$C(t) = s(t) + ih(t) \qquad \text{eq. (1)}$$

Where:

s(t), the real part, is the seismic trace

h(t), the imaginary part, is the Hilbert transform trace

If we transform the complex trace from Cartesian to polar coordinates, we have:

$$s(t) = A(t) \cos \phi (t) \qquad \text{eq. (2)}$$
$$h(t) = A(t) \sin \phi (t) \qquad \text{eq. (3)}$$

Figure A3-1: The complex trace seen complex space is helix defined by the real and imaginary traces. The instantaneous amplitude, A(t) is the shortest distance between the helix and the time axis at time t, and the instantaneous phase, φ(t), is the angle between A(t) and the real plane (Taner *et al.*, 1979)

where φ (t) is the instantaneous phase and A(t) is the amplitude envelope. From these we can define the three most fundamental complex trace attributes, instantaneous amplitude, phase, and frequency, in terms of known quantities, namely the seismic and quadrature traces (Taner *et al.*, 1979):

amplitude envelope	$A(t) = [s^2(t) + h^2(t)]^{1/2}$	eq. (4)
instantaneous phase	$\phi(t) = \arctan[h(t)/s(t)]$	eq. (5)
instantaneous frequency	$\omega(t) = d\omega(t)/dt$	eq. (6)

Several things should be noted about these attributes. First, they are *instantaneous* attributes; i.e. they are defined at each seismic time sample, and they answer the question, "what cosine waveform would be a best fit at that particular time sample?" (Barnes, 1998). They differ substantially from the familiar amplitude and phase spectra produced by the Fourier transform of the seismic trace. The amplitude and phase spectra tell us which is the best cosine waveform for each particular *frequency* that would best "fit" the seismic trace as a

whole, not at a particular time sample. Second, amplitude envelope is independent of phase on the real seismic trace. Thus, the maximum value of the reflection strength calculated from the complex trace need not occur on a peak or trough on the seismic trace (Taner *et al.*, 1979). Conversely, instantaneous phase is independent of reflection strength and, therefore, can be quite useful in tracking weak (low amplitude) reflections (Taner *et al.*, 1979; Brown, 1996a).

As pointed out by Barnes (1998), with a Hilbert transform and an imaginary component, the complex trace seems complicated and non-intuitive, and it is important not to lose sight of the fact that the purpose of complex trace analyses is to derive the instantaneous phase, amplitude and frequency of the seismic trace. The imaginary trace and its Hilbert transformation into the Cartesian plane is simply the most efficient way to calculate these attributes. In a more intuitive approach, instantaneous amplitude can be thought of as the maximum value that the trace can have under a constant-phase rotation (Barnes, 1998). In other words, if we imagine rotating the phase of the seismic trace degree by degree from 0° to 360°, the maximum trace amplitude at time t observed during the set of rotations is the instantaneous amplitude (Figure A3-2), and the phase rotation at which this maximum occurs is the instantaneous phase (with the opposite sign). Plotting these maxima and associated phase angles for all time samples produces the amplitude envelope and instantaneous phase trace, respectively (Figure A3-3). While this intuitive approach gives us a better understanding of what the attributes represent, it would be cumbersome in practice. Fortunately, it is mathematically possible to calculate these two instantaneous attributes at any time (t) from only two rotations of the seismic trace if the two considered differ by exactly 90° in phase. The two rotations used are 1) the seismic trace itself and 2) a −90° phase rotated version of it. Thus, in reality the imaginary trace is simply the −90° phase-

rotated version of the seismic trace needed to simplify the calculation of instantaneous amplitude and phase, rather than some abstract, theoretical construct, and the −90° phase rotation in Cartesian coordinates is accomplished by way of a Hilbert transformation.
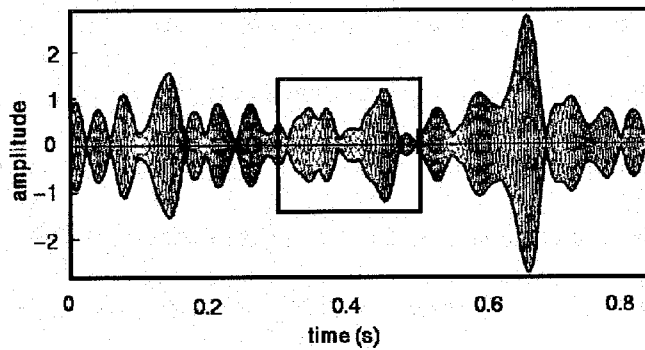
Figure A3-2: The seismic trace and phase-rotated versions of the seismic trace. The amplitude envelope, the maximum amplitude seen in the set of phase-rotated traces at each time sample, is defined by the solid heavy line (adapted from Barnes, 1998).
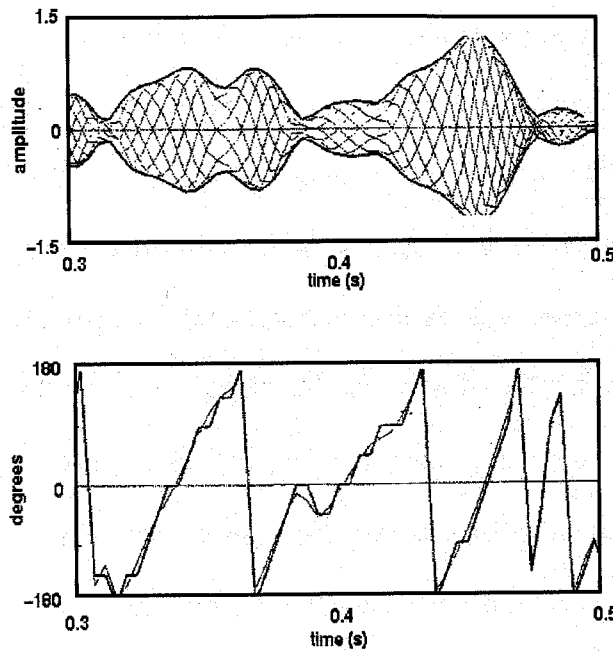
Figure A3-3: Enlarged view (area within the box shown in Figure 5.2) of the amplitude envelope and instantaneous phase trace determined by applying a series of constant-phase rotations to the seismic trace and finding the maximum amplitude and associated phase at each time t (Barnes, 1998).

Although seismic data contain limited information about travel time, amplitude, frequency, and attenuation of seismic energy, a huge number of attributes, upwards of 350, have been created and used to aid seismic interpretation and reservoir characterization (Brown, 1996a and b). All of these attributes are derived in some way from the primary information contained in the seismic trace or complex trace, but each attribute "looks" at the data in a slightly different way, emphasizing some aspects and, perhaps, downplaying others. The goal, or hope, is of course that different presentations of the data will allow us to better understand the variations in the geology and reservoir properties.

Attribute classification scheme

As pointed out by Brown (1996a and b), with so many attributes available, it is helpful to have some way in which to classify them. He proposed subdividing attributes by the primary type of seismic information they are derived from. Thus, attributes can be classified as pre- or post-stack: (1) time, (2) amplitude, (3) frequency, and (4) attenuation attributes (Figure A3-4).

In the most general sense, time attributes can be thought of as reflecting structure while amplitude, frequency, and attenuation attributes may reflect reservoir properties (Brown, 1996a and b). The relationship between amplitude attributes and reservoir properties is fairly straightforward. The amplitude of a reflection event is directly related to the acoustic impedance contrast which is itself a function of the physical properties of the reservoir. Alternatively, amplitude may also be related to bed thickness if beds are near the tuning thickness, $\lambda/4$. The relationship between frequency attributes and physical properties is more complicated. From basic physics, we know that velocity is the product of frequency and wavelength, and empirical velocity variations can be due to changes in reservoir properties, such as porosity, which affect seismic velocities. However, frequency is also affected by variations in lithology, stratigraphy, gas saturation, and fracture density, not to mention spatial and temporal variations in the seismic wavelet (Taner *et al.*, 1979; Rafipour, 1989; Brown, 1996a; Ziolkowski *et al.*, 1998). As a result, the relationship between instantaneous
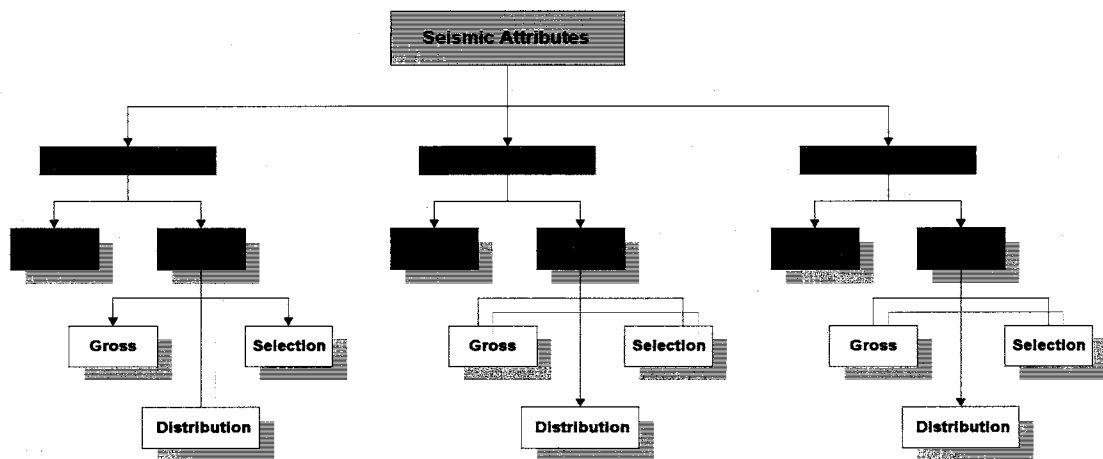

Figure A3-4: Seismic attribute classification scheme (adapted from Brown, 1996a and b).

frequency and reservoir properties is not well understood at present.

Since the discovery of "bright spots" in the Gulf of Mexico early 1970's, amplitude attributes have become the most commonly used in seismic-guided reservoir characterization. Amplitude attributes have been used to estimate a variety of reservoir properties including porosity, gas saturation, and P-wave velocity. The two primary instantaneous amplitude attributes are reflection amplitude and reflection strength. From these two, a large variety of formation attributes can be derived, such as average amplitude, ratio of positive to negative samples (within a window), percent greater than (user specified threshold), and energy half-time. Instantaneous frequency as defined in equation 6 and the frequency spectrum (derived from Fourier transforms) are the basis for numerous frequency attributes which have been shown to be useful in reservoir characterization and are often used in combination with amplitude attributes. These include average frequency, 1st, 2nd, and 3rd dominant spectral frequency, slope of instantaneous frequency, and the number of zero crossings. Examples of time attributes include dip of a horizon, travel time, phase, and numerous coherency/continuity attributes. Pre-stack and attenuation attributes, such as the instantaneous Q factor, are less commonly used and will not be discussed here.

Each of these attribute classes can be further subdivided into horizon and formation attributes depending on the way in which they were extracted. Attributes can be extracted either along an interpreted horizon (structural horizon) or over a window defined by 1) two structural horizons, 2) a structural horizon and a constant time interval above or below it, or 3) a constant time window, termed a "statistical slice" (Brown, 1996a, 1996b). The former are horizon attributes. These are usually instantaneous attributes, and the horizon used is one that has been autotracked with high precision. The latter are formation attributes which can be further subdivided into selection, gross, and distribution attributes (Brown, 1996a and b). Selection attributes include such things as an average value of the attribute over the window

or the maximum or minimum value within the window. Gross attributes are simply the sum of the attribute over the vertical extent of the window. Distribution attributes, in contrast, characterize how the seismic energy is distributed within the window. For example, energy half-time, the percentage of the total length of the time window in which the first 50% of the seismic energy occurs, measures how seismic energy is distributed over the window. Clearly each of these types of attributes provide us with different information about the reservoir, and the attributes used and the extraction technique employed would depend on the characteristics of the reservoir being studied, the data quality, and the goals of the study.

Seismic-guided reservoir characterization workflow

A generalized seismic-guided reservoir characterization workflow is shown in Figure A3-5. Seismic-guided reservoir characterization requires two data sets, the well log data (measured in depth) and the seismic data (measured in time), and the first step is relating these two through synthetic seismograms to determine which zone in the seismic corresponds to the zone of interest in the well logs. This is the most crucial step in the procedure as the well-seismic tie is one of the main controlling factors for the accuracy of all the resulting predictions.

Once the tie is made, the next step is deciding what type of attribute analysis is appropriate. For example, should we extract instantaneous attributes along the top horizon of the seismically defined window that encompasses the reservoir? Should we instead use formation attributes extracted over the entire reservoir? Alternatively, should we bypass any averaging all together and try to predict spatial (x, y, and z) variations in the reservoir? The choice made in this step determines everything that follows, from how we will look for a correlation to the form of the result (e.g. a map showing the average value of the property for the interval or a volume of physical properties), and in part, the accuracy of the resulting

prediction. The method chosen depends on factors such as the reservoir geometry, the physical property of interest, the amount of variation in the property and its distribution, the strength of the well-seismic tie, the data quality (particularly the amount and type of noise in the data), and the accuracy required for the study. If, for example, the reservoir is relatively thin (one or two reflections) and the lateral variation in the property is substantial enough to be seismically resolvable after the interval averaging process, a horizon-based attribute analysis or a formation average might be effective for predicting average reservoir properties from well logs. The advantage of these approaches are that they are relatively fast and easy to perform and the requirements for the well-seismic tie accuracy are the least stringent in that only the top and base of the reservoir need to be correctly identified in the seismic data. Simple geophysical modeling can be done to test whether or not the variation in the reservoir property will produce measurable changes in the seismic attributes. Given the ease of this approach, it is often worthwhile to try this first before investing time in a more rigorous approach involving attribute and physical property volumes.

The volume-based approach is a relatively new technique (Russell *et al.*, 1997; Schuelke *et al.*, 1998). In this approach, attribute curves are extracted at each well location and a relationship is looked for to transform the curves into an approximation of the physical property curve (either an actual well log or a curve calculated from a well log such as water saturation or core-corrected porosity). The mechanics of this technique will be described more fully in the methods section. This approach places considerably greater restrictions on the well-seismic tie. Each well must be tied accurately in depth throughout the interval of interest (rather than just at major acoustic impedance contrasts), and wells that cannot be tied must be excluded. The obvious advantage of this technique is that the result is a physical property volume which provides considerably more detail and flexibility than a simple map of average properties that can be obtained from a horizon- or window-based approach. This

method can be also used when other techniques fail to give the desired accuracy or necessary detail. For example, small variations in the physical property of interest may be lost in the averaging process if a horizon- or window-based approach is used. By employing a volume-based approach, we circumvent the averaging of properties and attributes and are able to model small physical property variations with depth.

Whatever method is chosen, the next step is deciding which attributes to include in the search for a correlation. Given the huge number of attributes available, this can be a daunting task. The choice of attributes can be guided by theory, seismic modeling, experience, knowledge of the geology, fuzzy logic (an approach which ranks attributes by their predictive value), or simply a brute force technique using all available attributes. However, increasing the number of attributes included in the search also rapidly increases the chances of observing a spurious correlation, particularly if the well data set is small (Figure A3-6). One way to reduce the chance of a spurious correlation is to rely on theory-based relationships between attributes and physical properties. However, there are many variable that can potentially affect these relationships, such as:

- ♦ Averaging of the properties/attributes during the stacking process
- ♦ Unknown effect of processing on the attributes
- ♦ Complexity of factors controlling the distribution of the physical property of interest
- ♦ Structural complexity
- ♦ Spatial variations in the seismic wavelet
- ♦ Noise in the data (particularly coherent noise)

All of these factors combine to make it difficult to make quantitative theoretical predictions of the way in which attributes change in response to variations in reservoir properties. One exception to this is the well known "bright spot" phenomenon seen in seismic data from the Gulf of Mexico. Here oil and gas sands produce abrupt, strong acoustic impedance contrasts creating high amplitude regions known as bright spots. Another well understood exception is

thin bed tuning. In this case, predictable variations in reflection amplitude occur when bed thicknesses are near the tuning thickness.

When the relationship between attributes and properties is not so obvious or easy to predict, we must turn to the data-driven approach first described by Schultz *et al.* (1994). In this method we look for empirical relationships between one or more attributes and the physical properties measured at the wellbore and assess their significance by statistical means rather than theory. In essence, we are looking for a function, f, such that at each well location
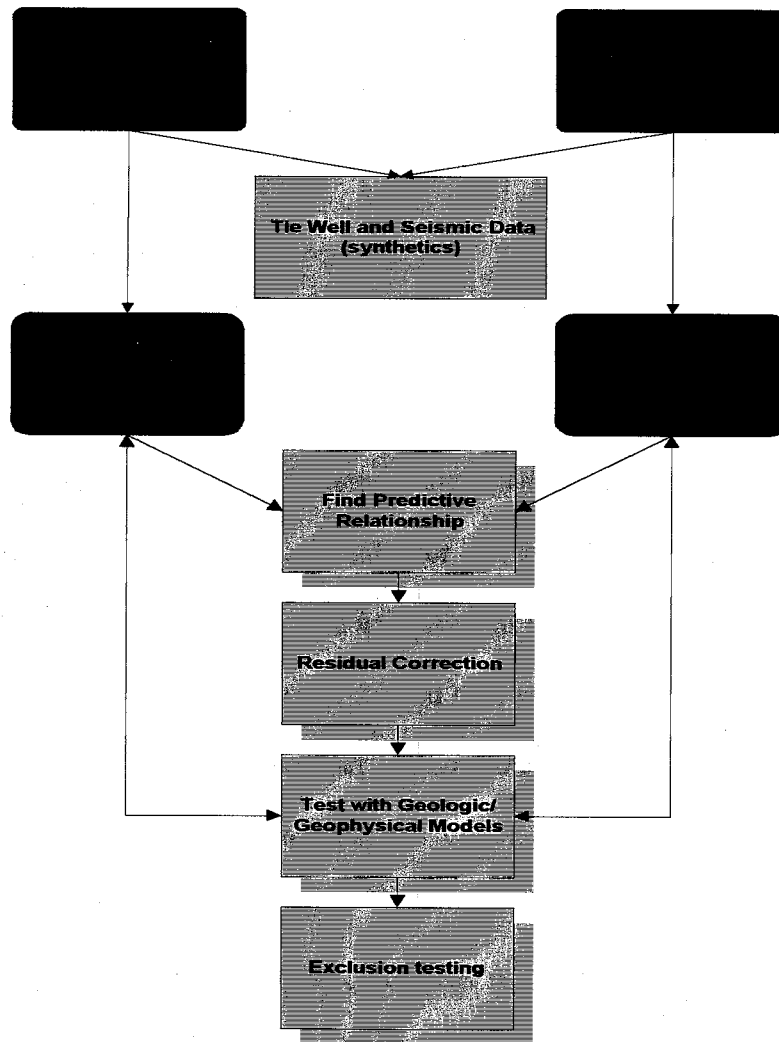

Figure A3-5: Typical seismic attribute workflow (modified from Schultz *et al.*, 1994).

where we have a measure of the property of interest we have a function of the form:

Horizon/Formation-based approach:

$$\text{Predicted physical property} = f(x, y, a_1, a_2, ..., a_n)$$

Volume-based approach:

$$\text{Predicted physical property} = f(x, y, t, a_1(t), ..., a_n(t))$$

The advantage of using multiple attributes is that individually single attributes may not be strongly correlated with the property of interest. By using more than one attribute we hope to combine weakly correlated attributes in such a way as to strengthen the overall correlation, making the prediction more robust. The methods commonly used to find the function f include:

♦ Multivariate linear regression techniques (nonlinear transforms can be applied prior to regression if desired)

♦ Geostatistical methods (kriging or cokriging)

♦ Neural nets

Once a relationship has been found that appears to be able to predict reservoir properties, we need to assess the statistical significance of the relationship. This is usually done with regression coefficients or Kendall's tau indicator. In the case of single attribute predictors, we can calculate the best fit line or curve and assess its fit with correlation coefficients (zero implies no correlation and one indicates that all data points lie on the fitted curve) and the root mean squared error. With more than one attribute, correlation coefficients can still be used, but they are calculated from predicted versus actual values, and the variation is measured relative to the $y = x$ line.

If or when a statistically significant correlation is found, the functional relationship can then applied to the seismic data to create a map or volume of the physical property, and the result can be evaluated terms of its geologic and geophysical reasonability (test the result

using geophysical/geologic models). This is one of the critical steps in the analysis because a statistically significant result is meaningless if it geologically unreasonable. Lastly, a residual correction can be done to force the prediction to exactly match the well data. The predictive power of the model can then be tested using wells that were excluded from the original analysis.
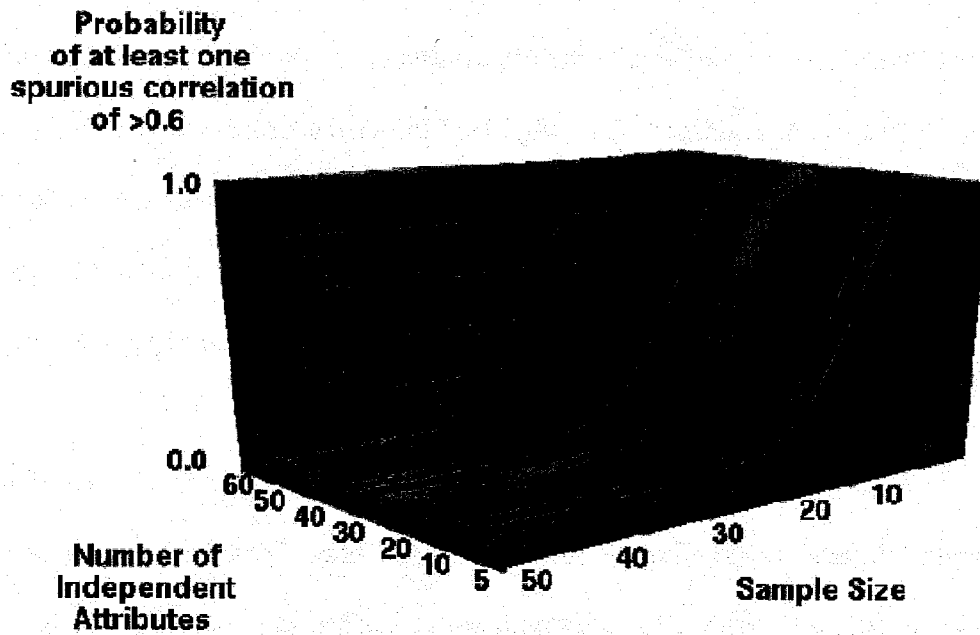

Figure A3-6: The probability of observing at least one spurious correlation with a correlation coefficient of greater than or equal to 0.6 between one attribute and a reservoir property as the number of attributes and wells included in the study vary. Note the rapid increase in the probability of a spurious correlation as the number of wells decreases (adapted from Kalkomey, 1997).

Appendix 4: Horizon-Based Attribute Analysis

In the early phase of this study, a horizon-based approach was taken to try to predict the net pay for the Second Sand. Numerous horizon and window attributes were extracted, and a weak correlation was found between a linear combination of five seismic attributes and net pay of the "C" sand. No predictive relationship could be found for the Second Sand as whole, presumably because this interval is too thick, and variations in porosity are lost in the averaging process. Although these result were somewhat disappointing (correlation coefficient of 0.48), they do emphasize the need for a volume-based attribute analysis. They are included here because they did shed light on the attributes that were the most effective at predicting porosity in the area and helped guide the choice of attributes in the volume-based approached described in Chapter 5. The methods employed and the results from this phase of the study are briefly summarized below.

Methods

The net pay for the "C" sand was calculated at 34 wells where crossplot porosity logs were available. Net pay was defined as the number of feet within the interval where a porosity cutoff of 10% (the minimum porosity necessary for a well in this field to be considered economical) was exceeded. Horizon and window attributes were extracted from the "C" sand interval in the seismic data. The window used for the attribute extraction was defined by smoothed, autotracked horizons corresponding to the top and base of the "C" sand. The attributes extracted are summarized below. Where the attribute listed is an instantaneous one, it was extracted along horizon for the top of the "C"sand.

- Average reflection amplitude
- Average peak amplitude
- Average trough amplitude
- Average absolute amplitude
- Average reflection strength
- Maximum peak amplitude
- Maximum trough amplitude
- Maximum reflection strength
- Maximum absolute amplitude
- Slope of reflection stength
- 1st peak spectral frequency
- 2nd peak spectral frequency
- 3rd peak spectral frequency
- average frequency
- Slope of spectral frequency
- Slope of instantaneous frequency
- Average instantaneous phase
- Isochron
- Energy half time
- Percent greater than
- Percent less than
- averaged coherency volume

- Percent less than
- Travel time to top of the window
- Travel time to base of the window
- Ratio of positive to negative samples
- RMS amplitude
- Dip of the upper horizon
- Average coherency from a maximum coherency volume ("C" sand only)
- Average coherency from a minimum coherency volume ("C" sand only)
- Average coherency from an spatially averaged coherency volume ("C" sand only)
- Instantaneous reflection strength
- Instantaneous reflection amplitude
- Instantaneous frequency
- Instantaneous phase
- Instantaneous coherency from a maximum coherency volume
- Instantaneous coherency from a minimum coherency volume
- Instantaneous coherency from a spatially

Possible correlations were evaluated using (1) Spearman rank coefficients, (2) 2-D crossplots, (3) 3-D crossplots, and (4) linear regression models (1st and 2nd degree) available in Landmark Graphics' Rave package. Spearman rank coefficients have an advantage over standard linear regression techniques in that they rank the strength of both linear and nonlinear correlations between two variables. The values theoretically range between zero and one, with zero indicating no correlation and one indicating a one-to-one correspondence. Crossplots were used to visually evaluate attribute-porosity trends for all pairs with comparatively high Spearman rank coefficients (which in some cases was quite low). These

were then visually evaluated in 2-D crossplots. Attributes that showed any trend whatsoever with reservoir properties in the 2-D crossplots were then paired in different combinations to produce 3-D crossplots (essentially a brute force approach to evaluate as many combinations as possible). Trends on these could be assessed by interactively rotating the crossplot in any direction desired. If any trend was observed for the set of data points as a whole or for a subset of the data points, a linear regression model was created to quantify the correlation using the Pearson correlation coefficient (R) and the mean squared error. When acceptable correlations were found, the constants in the linear regression equation could then be used to transform the attribute maps into a net pay map. The resulting map was then evaluated for geologic reasonability.

Results and Discussion

A combination of five attributes extracted from the "C" sand correlate weakly with net pay of the "C" sand. These attributes are a combination of window and instantaneous attributes:

- ◆ Dip of the top of the "C" sand
- ◆ "C" sand isochron
- ◆ minimum coherency
- ◆ instantaneous frequency
- ◆ reflection amplitude

A linear regression model using these five attributes is shown in Figure A4-1. The equation determined from the linear regression is:

$$\text{Net Pay (ft)} = 456 + 0.00192 \text{ (amplitude)} + 0.163 \text{ (frequency)} - 3.80 \text{ (coherency)} - 1.99 \text{ (dip)} + 3.47 \text{ (isochron)}$$

This equation was applied to the attribute maps to produce a map of net pay for the "C" sand (Figure A4-2). The relationship between predicted and actual net pay has a Spearman rank

coefficient of 0.677, a correlation coefficient of 0.480, and an associated RMS error of +/-23.6'.

As with the volume-based analysis, the number of attributes used in the model make it difficult to determine a causal relationship between physical rock properties and the seismic response from rock physics, although several qualitative observations can be made. Average reservoir porosity decreases in areas of high dip and low continuity, and zones with the greatest dip tend to follow the same trend as faults in the area. This would seem to imply that sealing faults and fractures exert some control on the porosity distribution. In addition, the highest values of net pay occur in an elongate zone just downslope from the large, central re-entrant in the upper slope where channel deposits would be expected. This indicates that primary depositional facies is still one of the main factors controlling reservoir quality.
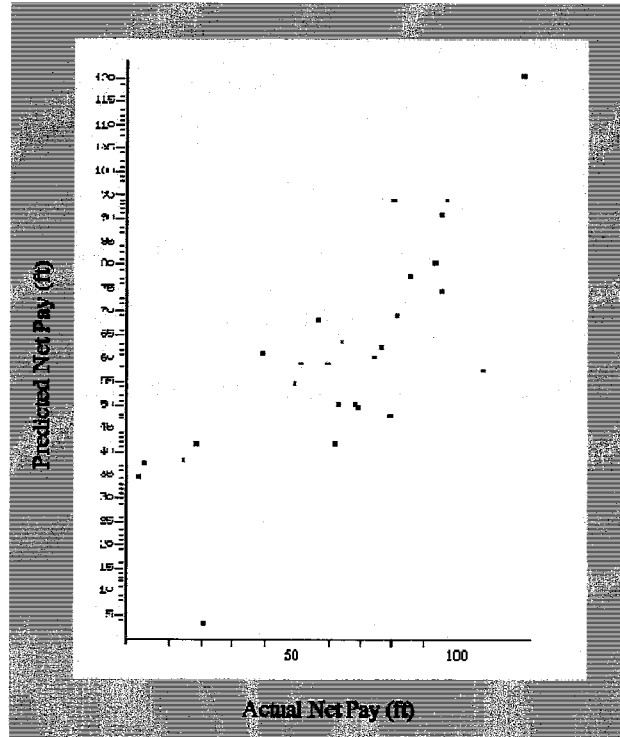
Figure A4-1: Predicted versus actual net pay for the "C" sand determined using five seismic attributes.
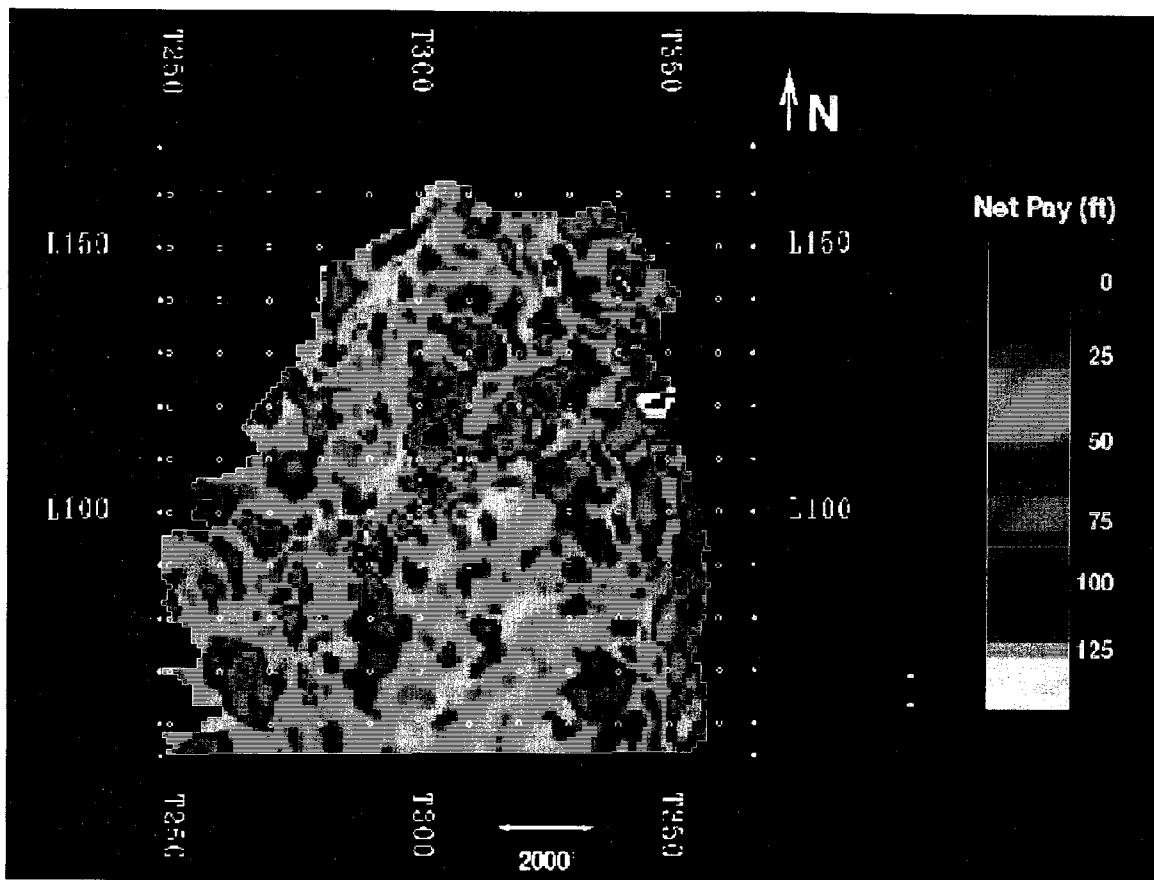
Figure A4-2: Map of net pay within the "C" sand estimated using a combination of five horizon and window attributes. The largest porosity thick, in the center of the study area, trends roughly N-S and occurs directly below the central re-entrant in the upper slope.

No relationship was found that could predict net pay for the Second Sand as a whole (all Spearman rank coefficients were below 0.5 and linear regression models created for numerous attribute combinations did not have statistically significant correlation coefficients).

Appendix 5: Seismic Attributes Used in the Multiattribute Analysis

The seismic attributes used in the multiattribute analysis are tabulated below (Table A5-1). Nonlinear transforms were applied to both the target logs and attribute curves (columns 1 and 3). The best attributes are ranked (best to worst) by their ability to predict the porosity logs (columns 4 and 5) determined by a standard linear regression where the weighting factors are scalars. For brevity, only the best seven attributes and their transforms are included below.

Table A5-1: Seismic attributes used in the volume-based multiattribute analysis.

None	Smoothed impedance	$1/x$	0.0222	0.3298
$\sqrt{x}$	Smoothed impedance	$1/x$	0.0222	0.3254
None	Smoothed impedance	$\log(x)$	0.0223	-0.3224
$\sqrt{x}$	Smoothed impedance	$\log(x)$	0.0223	-0.3180
None	Smoothed impedance	$\sqrt{x}$	0.0223	-0.3183
$\sqrt{x}$	Smoothed impedance	$\sqrt{x}$	0.0223	-0.3139
None	Smoothed impedance	None	0.0223	-0.3139
$\sqrt{x}$	Smoothed impedance	None	0.0224	-0.3096
None	Smoothed impedance	x^2	0.0224	-0.3046
$\log(x)$	Smoothed impedance	$1/x$	0.0224	0.3159
$\sqrt{x}$	Smoothed impedance	x^2	0.0224	-0.3002
None	Integrated absolute amplitude	None	0.0224	-0.2984
Log	Smoothed impedance	$\log(x)$	0.0225	-0.3085
x^2	Smoothed impedance	$1/x$	0.0225	0.3278
$\log(x)$	Smoothed impedance	$\sqrt{x}$	0.0225	-0.3044
$\log(x)$	Smoothed impedance	None	0.0225	-0.3001
$\sqrt{x}$	Integrated absolute amplitude	None	0.0225	-0.3069
x^2	Smoothed impedance	$\log(x)$	0.0225	-0.3205
x^2	Smoothed impedance	$\sqrt{x}$	0.0225	-0.3165
$\log(x)$	Smoothed impedance	x^2	0.0226	-02908
x^2	Smoothed impedance	None	0.0226	-0.3122
x^2	Integrated absolute amplitude	None	0.0227	-0.2685
none	Amplitude-weighted frequency	None	0.0227	-0.2667
none	Amplitude-weighted frequency	None	0.0227	-0.2667
none	Amplitude-weighted frequency	None	0.0227	-0.2667
x^2	Smoothed impedance	x^2	0.0227	-0.3030
$\sqrt{x}$	Amplitude-weighted frequency	None	0.0227	-0.2663
$\log(x)$	Integrated absolute amplitude	None	0.0228	-0.3086
x^2	Amplitude-weighted frequency	None	0.0229	-0.2665
$\log(x)$	Amplitude-weighted frequency	None	0.0230	-0.2652
$1/x$	Smoothed impedance	$1/x$	0.0233	-0.2784
$1/x$	Smoothed impedance	$\log(x)$	0.0234	0.2712
$1/x$	Smoothed impedance	$\sqrt{x}$	0.0234	0.2672
none	Average frequency	None	0.0234	0.1055
$1/x$	Smoothed impedance	None	0.0234	0.2630
$\sqrt{x}$	Average frequency	None	0.0235	0.1252
none	Dominant frequency	None	0.0235	-0.0515
$1/x$	Smoothed impedance	x^2	0.0235	0.2540
none	Minimum coherency	$1/x$	0.0235	0.0495
none	Minimum coherency	$\log(x)$	0.0235	0.0436
none	Minimum coherency	x^2	0.0235	0.0384

none	Minimum coherency	$\sqrt{x}$	0.0235	0.0361
none	Minimum coherency	None	0.0235	0.0301
none	Amplitude-weighted phase	None	0.0235	-0.0144
$\sqrt{x}$	Dominant frequency	None	0.0236	-0.0500
$\sqrt{x}$	Minimum coherency	$1/x$	0.0236	0.0409
$\sqrt{x}$	Minimum coherency	$\log(x)$	0.0236	0.0356
$\sqrt{x}$	Minimum coherency	x^2	0.0236	0.0327
$\sqrt{x}$	Minimum coherency	$\sqrt{x}$	0.0236	0.0292
$\sqrt{x}$	Minimum coherency	None	0.0236	0.0241
$\sqrt{x}$	Amplitude-weighted phase	None	0.0236	-0.0359
x^2	Average frequency	None	0.0236	0.0675
$\log(x)$	Average frequency	None	0.0236	0.1438
x^2	Dominant frequency	None	0.0237	-0.0599
x^2	Minimum coherency	$1/x$	0.0237	.0629
x^2	Minimum coherency	$\log(x)$	0.0237	0.0566
x^2	Minimum coherency	x^2	0.0237	0.0453
x^2	Minimum coherency	$\sqrt{x}$	0.0237	0.0472
x^2	Minimum coherency	None	0.0237	0.0391
$1/x$	Integrated absolute amplitude	None	0.0238	0.2852
x^2	Amplitude-weighted phase	None	0.0238	0.0221
$\log(x)$	Dominant frequency	None	0.0238	-0.0508
$\log(x)$	Minimum coherency	$1/x$	0.0238	0.0314
$\log(x)$	Minimum coherency	$\log(x)$	0.0238	0.0266
$\log(x)$	Minimum coherency	x^2	0.0238	0.0256
$\log(x)$	Minimum coherency	$\sqrt{x}$	0.0238	0.0214
$\log(x)$	Minimum coherency	None	0.0238	0.0172
$\log(x)$	Amplitude-weighted phase	None	0.0239	-0.0585
$1/x$	Amplitude-weighted frequency	None	0.0240	0.2582
$1/x$	Average frequency	None	0.0249	-0.1714
$1/x$	Dominant frequency	None	0.0249	0.0589
$1/x$	Dominant frequency	None	0.0249	0.0589
$1/x$	Minimum coherency	$1/x$	0.0249	-0.0115
$1/x$	Minimum coherency	x^2	0.0250	-0.0083
$1/x$	Minimum coherency	$\log(x)$	0.0250	-0.0065
$1/x$	Minimum coherency	$\sqrt{x}$	0.0250	-0.0044
$1/x$	Minimum coherency	None	0.0250	-0.0020
$1/x$	Amplitude-weighted phase	None	0.0251	0.1020

Table A5-1: Seismic attributes used in the volume-based multiattribute analysis

Appendix 6: Results of Multiattribute Analyses Using Less Than Five Attributes

For comparison with the five-attribute prediction of the porosity logs, the results of using

one, two, three, and four attributes are shown below in Figures A6-1 through A6-5.
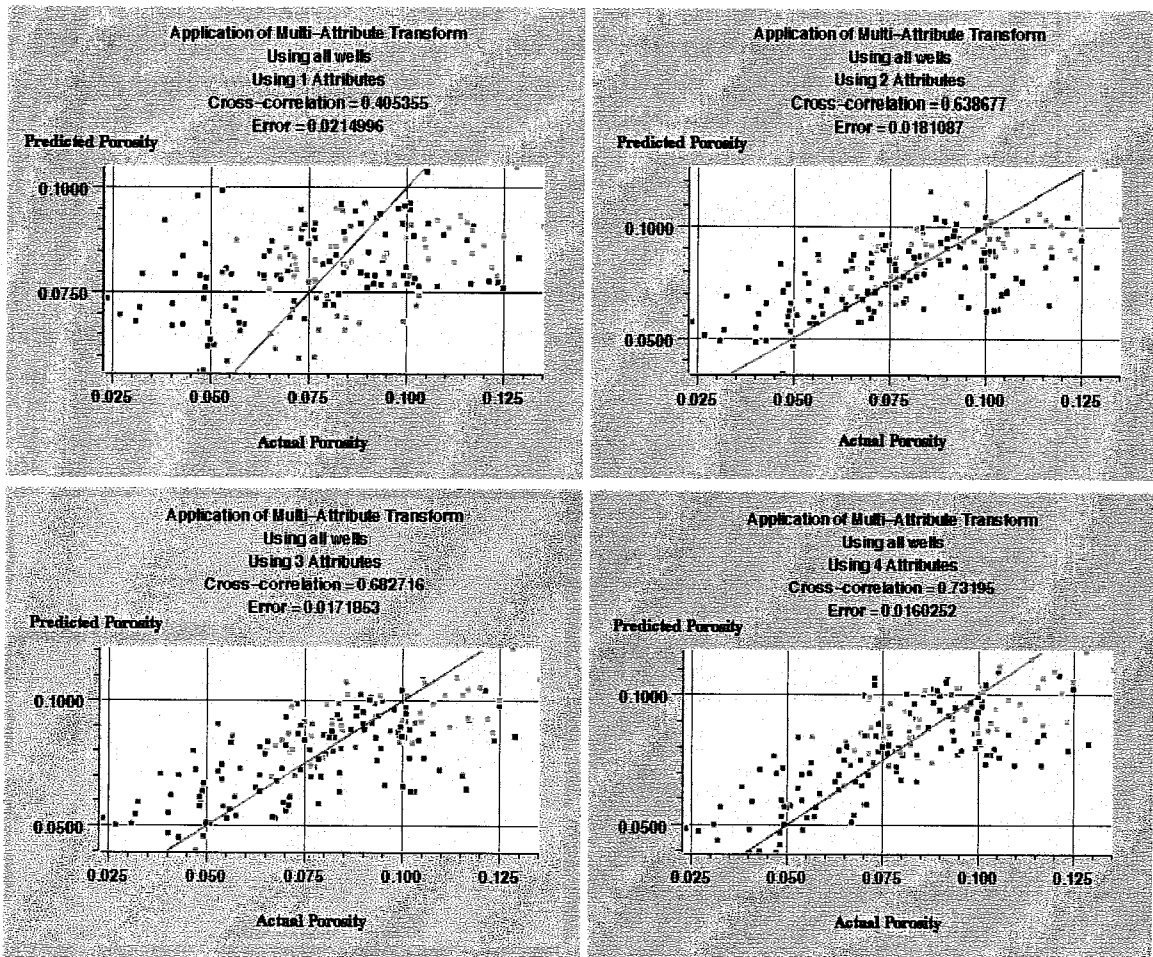

Figure A6-1: Predicted versus actual porosity using a) one attribute, b) two attributes, c) three attributes, and d) four attributes. The magenta line in each crossplot is the y = x line. Note the decrease in the scatter about y = x as additional attributes are added.
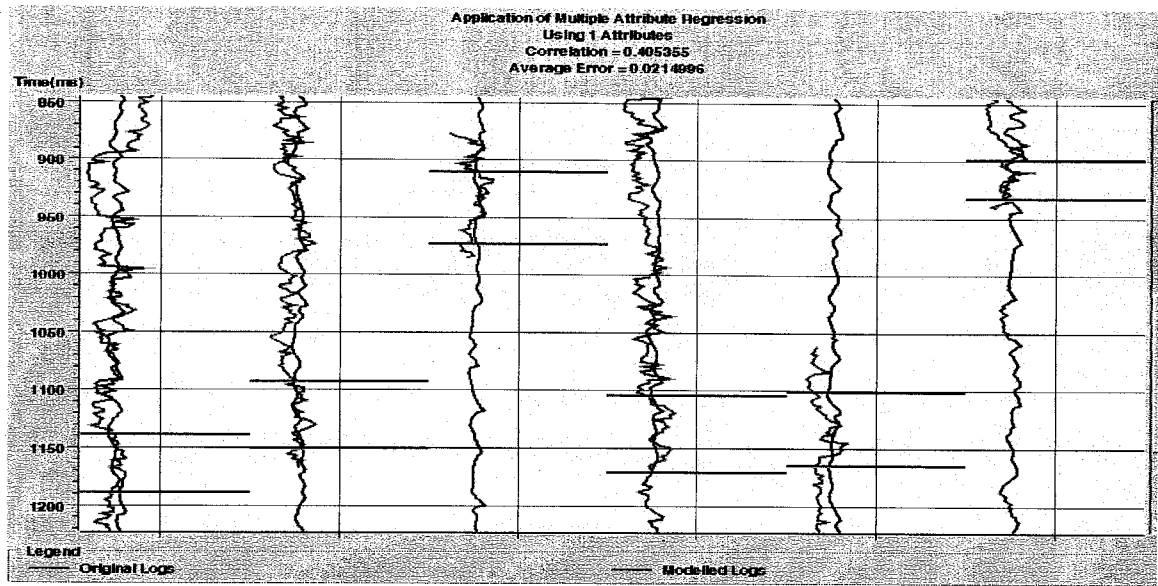
Figure A6-2: Target porosity logs and predicted porosity logs for the one attribute predictor. The solid black lines indicate the top and base of the Second Sand (analysis window). The vertical axis is two-way travel time in ms.
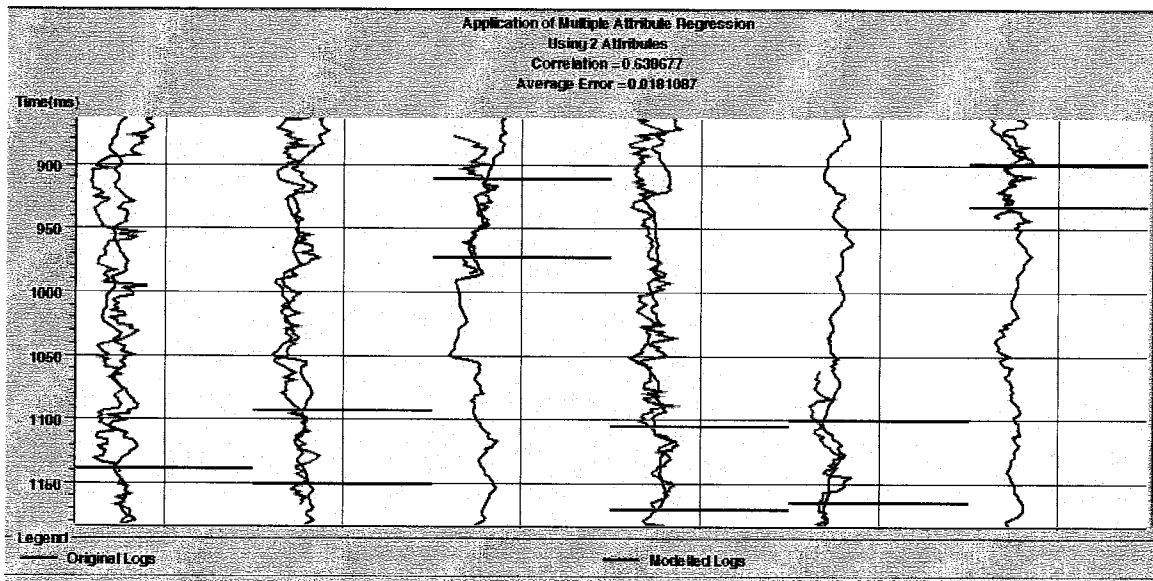

Figure A6-3: Target porosity logs and predicted porosity logs for the two attribute predictor. The solid black lines indicate the top and base of the Second Sand (analysis window). The vertical axis is two-way travel time in ms.
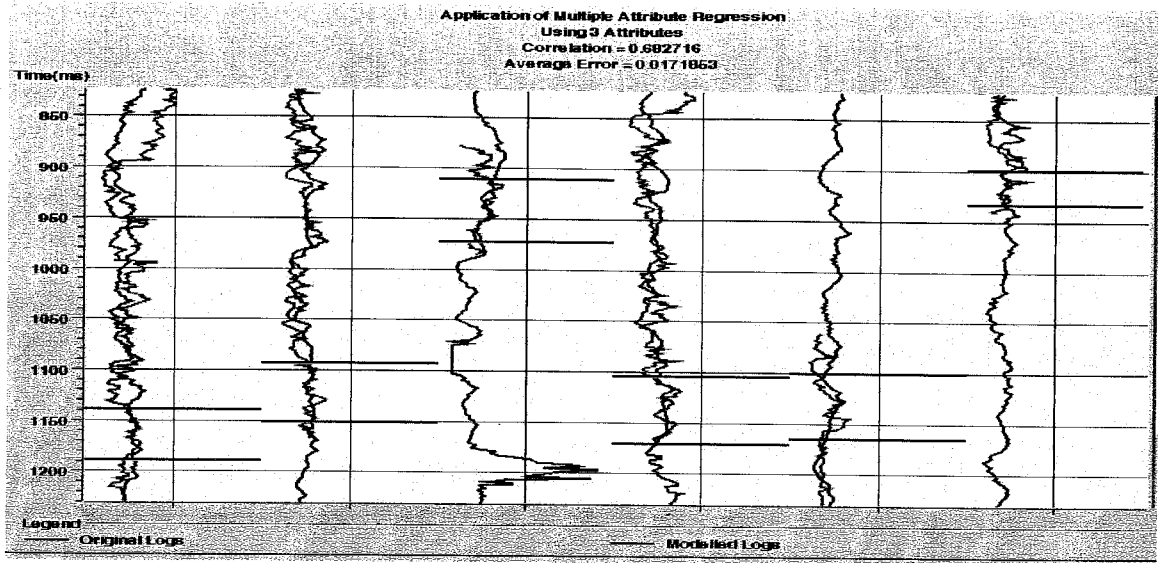
Figure A6-4: Target porosity logs and predicted porosity logs for the three attribute predictor. The solid black lines indicate the top and base of the Second Sand (analysis window). The vertical axis is two-way travel time in ms.
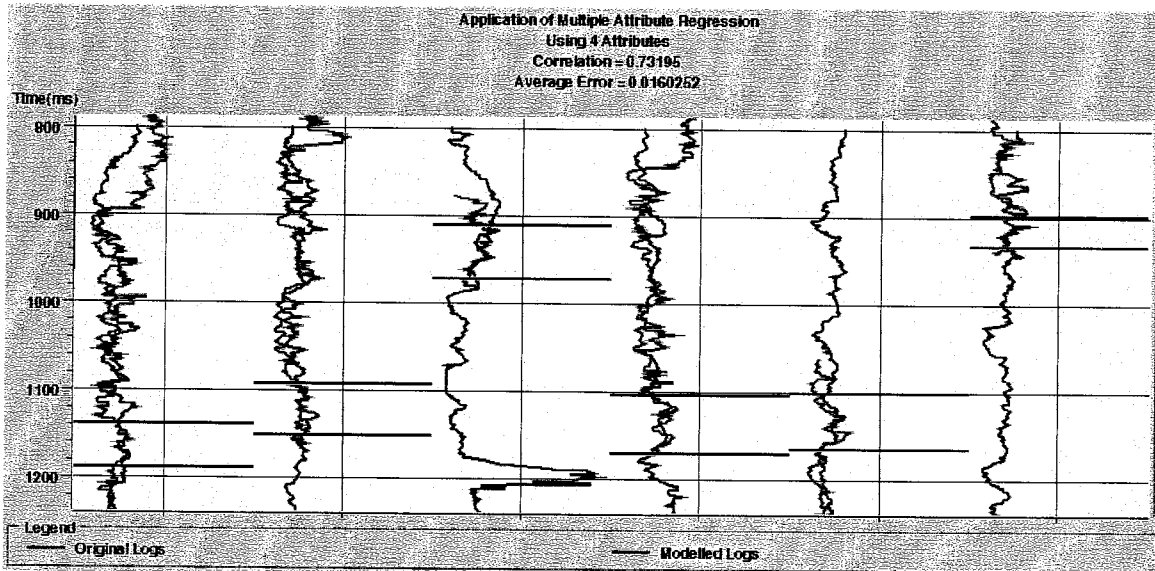

Figure A6-5: Target porosity logs and predicted porosity logs for the four attribute predictor. The solid black lines indicate the top and base of the Second Sand (analysis window). The vertical axis is two-way travel time in ms.

This thesis is accepted on behalf of the faculty
of the Institute by the following committee:

Advisor

_____

5/6/99

Date

I release this document to the New Mexico Institute of Mining and Technology

4-6-99

Student Signature   Date